# RAREFACTION EFFECTS ON THERMAL TRANSPORT AND FLOW STRUCTURES IN CAVITY FLOWS

A Dissertation

by

VISHNU VENUGOPAL

Submitted to the Office of Graduate and Professional Studies of
Texas A&M University
in partial fulfillment of the requirements for the degree of

DOCTOR OF PHILOSOPHY

| | |
|---|---|
| Chair of Committee, | Sharath S. Girimaji |
| Committee Members, | Diego A. Donzis |
| | Rodney Bowersox |
| | Hamn-Ching Chen |
| Head of Department, | Rodney Bowersox |

December 2016

Major Subject: Aerospace Engineering

ABSTRACT

Accurate simulation and modeling the effects of rarefaction on heat and mass transport is of much interest in high-speed flow applications including hypersonic vehicles and atmospheric re-entry flights. Toward this end, the present work develops numerical schemes appropriate for a wide range of Knudsen numbers and performs analytical investigation of the rarefaction effects. First, the Unified Gas Kinetic Scheme (UGKS) is extended to a wider range of Mach and Knudsen numbers by implementing WENO (Weighted Essentially Non-Oscillatory) interpolation. Direct Simulation Monte Carlo (DSMC) computations are also performed when appropriate for comparison purposes. Though DSMC method is theoretically valid in the entire range of Knudsen numbers (from continuum to free-molecular), real computations with DSMC are limited to rarefied flows as this method demands excessive computational resources to simulate continuum/near-continuum flows.

The effect of rarefaction is examined in the canonical lid-driven flows. In particular, the effect of cavity size (cavity aspect ratio), flow speed (lid Mach number) and degree of rarefaction (global Knudsen number) on flow structures and transport properties in the cavity are examined. The simulations are performed at a wide range of flow regimes (a) subsonic incompressible, subsonic compressible and supersonic (b) Knudsen numbers: continuum, near-continuum, transition and highly rarefied regimes. Flow (vortex) structures and thermal transport are characterized as functions of different flow regimes and cavity size. Mechanism of vortex evolution is investigated at a microscopic perspective.

Parametric studies followed by careful observations and rigorous analyses reveal important insights to the rarefaction effects on the heat and mass transport behavior

of canonical 2D cavity flows. The proposed scheme can extensively be used for fluid flows comprising of large density variations whose length scales extend from a macro-scale to a molecular scale.

TABLE OF CONTENTS

Page

LIST OF FIGURES

FIGURE Page

LIST OF TABLES

TABLE Page

# 1. INTRODUCTION

The nature of heat and mass transfer in rarefied (low density) high-speed flows around hypersonic vehicles and atmospheric re-entry flights is significantly different from the well-known continuum regime behavior. The mean collision time, which is defined as the average time interval between successive inter-molecular collisions, is large in a rarefied flow. A high mean collision time delays the relaxation of molecules toward their local equilibrium. Therefore, non-equilibrium effects are easily triggered in rarefied flows, which invalidates the applicability of thermodynamic relationships and continuum constitutive models. For instance, the conductive heat flux vector in a continuum medium is governed by Fourier law and is directed from hot to cold regions. However, this law may not be applicable in a low-density environment. The implications of such behavior on the second law of thermodynamics is critical, demanding a closer investigation of thermal transport and entropy evolution in rarefied flows.

Understanding the mechanisms behind such intense aero-thermodynamic phenomena in high-speed rarefied flows is of much importance to the aerospace community. However, replicating rarefied flow conditions in ground-based laboratory facilities is both expensive and technically challenging. Hence, there is an important role for computational models in the investigation of rarefied flow physics. Many of the rarefied flows of aerospace interest include a wide range of speeds and Knudsen numbers (degree of rarefaction). Therefore, it is also necessary that the simulation tool be capable of capturing a range of Mach number and Knudsen number physics within a single flow domain. Figure 1.1 shows the limits of validity of different mathematical models as the degree of rarefaction is varied from continuum to

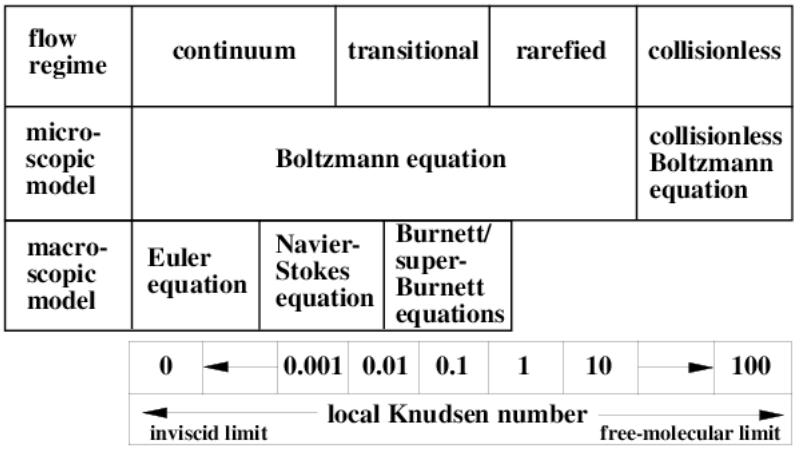


Figure 1.1: Knudsen number limits on different mathematical models

free-molecular regimes. Knudsen number, defined as the ratio of particle mean free path ($\lambda$) to a characteristic length scale of the flow, is the parameter representing the degree of rarefaction. Local Knudsen numbers are often defined to characterize the degree of non-equilibrium in a specific region of the flow. For example, a local Knudsen number with a length scale based on density gradient ($\nabla\rho$) is used to study any non-equilibrium effects due to rarefaction (Equation 1.1).

$$Kn_{local} = \frac{\lambda}{\frac{\rho}{|\nabla\rho|}} \tag{1.1}$$

From Figure 1.1, it can be seen that the Navier-Stokes (NS) governing equations are inapplicable beyond a local Knudsen number of about 0.001. The reason underlying the failure is primarily due to the lack of validity of simple constitutive relations, such as Newton's law of viscosity or Fourier's law of heat conduction. In other words, the transport models in the NS equations fail when the gradients of the macroscopic variables become so steep that their associated length scales approaches the order of the particle mean free path. However, extended hydrodynamic equa-

tions such as Burnett or super-Burnett corrections, with higher order terms, have successfully extended the applicability of continuum models to higher Knudsen numbers for non-equilibrium flows. In this study, numerical simulations of rarefied flows are performed using gas-kinetics based numerical methods that are derived from the broadly-applicable Boltzmann equation. These equations do not assume any closed form of constitutive relationship. The transport fluxes and other properties are calculated directly from the single particle velocity distribution function (vdf). The fluxes will then be compared against extended thermodynamic formulations.

Lid-driven cavity flow is an excellent problem in which the non-equilibrium effects due to rarefaction can be examined. Numerical simulations of lid-driven cavity flows are of great interest to the fluid dynamics community as they are associated with complex flow structures that evolve within a simple geometry. Slits, suction chambers, impact damages or any other pockets on the surface of a flight vehicle can be conveniently modeled as cavities of different sizes and shapes. Such a study is also of direct practical interest as the presence of a cavity on the thermal protection system can potentially be hazardous. For instance, in high-speed re-entry flows, the freestream may be rarefied but the flow within the cavity could be close to continuum due to the accumulation of molecules. This early transition can heat up the cavity leading to high surface stresses and temperatures for extended time and most likely damage the surface. According to Bertin and Cummings [5], one of the main reasons for the damage of NASA space shuttle Columbia was the breaching of hot gas through a cavity in the thermal protection system of the vehicle during its re-entry. Hence, it is important to characterize the flow behavior in a cavity of given size and shape as functions of flow speed and degree of rarefaction.

The main objective of this work is to analyze and understand the non-equilibrium heat and mass transport behavior in a cavity flow as a function of cavity aspect ra-

tio, flow speed and rarefaction parameter. Continuum and near-continuum lid-driven cavity flows have been examined extensively in literature. Recently, an interesting work by Naris and Valougeorgis [31] investigates the transformation between different stable vortex structures in low-speed cavity flows, for a wide range of cavity sizes and Knudsen numbers. Analytically, rarefied flows have been examined with different extended higher-order hydrodynamic models, such as the Burnett, BGK (Bhatnagar-Gross-Krook)-Burnett, augmented Burnett, regularized Burnett and super-Burnett equations [52, 21, 2, 1]. These models are shown to accurately capture the macroscopic properties and other significant features pertaining to rarefied effects such as the non-linear pressure drop in microchannel flows [34, 26]. However, the evolution of model transport properties and their reliability over the entire range of Knudsen numbers and flow speeds are yet to be investigated.

The objectives for this dissertation can be divided into the following parts:

1. Development of a numerical tool that can accurately capture the flow physics with continuum as well as a rarefied media.

2. Characterize the flow structures in a cavity as a function of cavity aspect ratio, lid velocity and Knudsen number.

3. Investigate the validity and applicability of the Fourier, augmented Burnett and BGK-Burnett extended thermodynamic models.

4. Examine the implications of the second law on transport mechanisms for the proposed gas kinetic scheme.

5. Investigate the vortex evolution mechanism in cavity flows through a microscopic perspective.

6. Study the effects of Prandtl number on the rarefaction and thermal transport in cavity flows.

Chapter 2 discusses the finite volume Unified Gas Kinetic Scheme (UGKS) enhanced with WENO (Weighted Essentially Non-Oscillatory) reconstruction. The Direction Simulation Monte Carlo (DSMC) method is also outlined. Extensive validation of UGKS against DSMC for cavity flow simulations are presented in Chapter 3. The flow structures are then characterized as functions of degree of freestream rarefaction, flow speed and cavity size. Chapter 4 deals with a comprehensive thermal transport analyses of highly non-equilibrium flows and reveals important implications of second law of thermodynamics on UGKS simulations. Vortex evolution mechanism and its effects on rarefaction and flow speed for different cavity sizes are investigated in Chapter 5. The effect of Prandtl number on rarefaction and thermal transport in cavity flows is studied in Chapter 6. The dissertation concludes by highlighting relevant physical insights gained from non-equilibrium cavity flow simulations and directs to important future works (Chapter 7). A comprehensive description of algorithm and step-by-step implementation of UGKS are explained in Appendix A.

# 2. NUMERICAL SIMULATION SCHEMES: UNIFIED GAS KINETIC SCHEME AND DIRECT SIMULATION MONTE CARLO

This chapter provides a description of the proposed numerical schemes to simulate non-equilibrium flows. As mentioned earlier, the flows of interest are exposed to high degrees of non-equilibrium that are more or less triggered by rarefaction effects. We go beyond the conventional set of Navier-Stokes-Fourier (NSF) equations and utilize the more fundamental Boltzmann equation for the following reasons:

1. NSF equations are derived based on continuum hypothesis which breaks down in regions of high local Knudsen number.

2. Microscopic properties are not smooth due to high non-equilibrium effects. Therefore, the macroscopic properties cannot be approximated through a statistical average of the respective microscopic properties.

3. Most importantly, the modeled transport properties fail at a much earlier stage in the transition regime, i.e. even before the system reaches a significant rarefaction level.

## 2.1 Boltzmann and Bhatnagar-Gross-Krook (BGK) Equations

Boltzmann equation, derived from a microscopic or molecular viewpoint, describes the temporal evolution equation of particle velocity distribution function $f$, in phase space (Equation 2.1). In Equation 2.1, $\mathbf{x}$ is the position vector, $\mathbf{u}$ is the particle velocity and $\mathbf{F}$ is any external force per unit mass such as the acceleration due to gravity. $Q_{collision}$ is the non-linear collision integral term which computes the change in the distribution function due to inter-molecular collisions. Collision

integral depends on the kind of collisions and the molecular species involved. A combination of partial differential terms and integral terms in the Boltzmann equation and its independent variables being seven $(x_1, x_2, x_3, u_1, u_2, u_3, t)$ for an unsteady three dimensional flow, pose formidable issues to solve the equation using a direct numerical method.

$$\frac{\partial (f)}{\partial t} + u_j \frac{\partial (f)}{\partial x_j} + \frac{\partial (F_j f)}{\partial u_j} = Q_{collision} \tag{2.1}$$

The challenges encountered in directly solving the Boltzmann equation can be primarily attributed to the non-linear nature of the collision integral. Bhatnagar et al. [6] proposes that this complex term can be replaced by an approximation, often known as the BGK collision model, that simplifies those difficulties but simultaneously retaining most of the physics accounted by the complete Boltzmann equation. If the collision integral in the Boltzmann equation is replaced by the BGK model, the resulting governing equation is known as the BGK equation (Equation 2.2).

$$\frac{\partial (f)}{\partial t} + u_j \frac{\partial (f)}{\partial x_j} + \frac{\partial (F_j f)}{\partial u_j} = \frac{f^{(0)} - f}{\tau} \tag{2.2}$$

Here, $f^{(0)}$ is the Maxwellian distribution function that is unique for a given mean velocity $\overline{\mathbf{u}}$ and temperature $T$, and $\tau$ is the mean collision time that is inversely proportional to density $\rho$, and can have dependence on temperature. The BGK equation is a closure model that describes the relaxation of an initially non-equilibrium distribution $f$ towards the equilibrium distribution $f^{(0)}$ with a local relaxation time of $\tau$. Note that the quantities $\overline{\mathbf{u}}$ and $T$ that appear in $f^{(0)}$ are defined as the moments of $f$. Thus the BGK equation remains as a non-linear integro-differential equation. However, this form of the equation permits solution through the method of characteristics

which enables a numerical approach to simulate a variety of flows of interest. In this study, we use recently developed approach for directly solving the BGK equation known as the Unified Gas Kinetic Scheme [46].

## 2.2 Numerical Schemes

The simulation tools employed to compute the lid-driven cavity flow namely Unified Gas Kinetic Scheme (UGKS) and Direct Simulation Monte Carlo (DSMC) are described in this section.

### *2.2.1 Unified Gas Kinetic Scheme (UGKS)*

Successful efforts have been made in literature to couple continuum and discrete solvers to derive a hybrid scheme [11, 32] or even to extend the Boltzmann equation based solvers to continuum regime [28, 15]. However, the restrictions on time-step (of the order of mean collision time) and grid size (of the order of mean free path) cannot be overcome because of the operator-splitting methods used for separating the collision and transport phenomena. A reliable gas kinetic scheme that can accommodate a high degree of non-equilibrium was developed by Xu [45] and has even been extended to strong turbulent flows [23, 24]. The original version of the scheme assumes a smooth velocity distribution function throughout the domain and is applicable near equilibrium. More recently, attempts have been made to discretize the velocity space as well, along with the physical space, so as to incorporate the evolution of discontinuous velocity distribution functions arising from high non-equilibrium effects. The Unified Gas Kinetic Scheme (UGKS) of Xu and Huang [46], where the whole phase space is discretized, has provided promising preliminary results in both rarefied and continuum regimes [19, 20]. As a result, the time-step and the cell size for a UGKS simulation are restricted by the Courant-Friedrichs-Lewy (CFL) condition rather than the corresponding mean collision time or mean free path.

The Unified Gas Kinetic Scheme is a finite volume approach wherein the fluxes through the control surfaces are derived from the BGK-Shakhov model [37] with a discretized velocity space [50]. For simplicity, we start from the one-dimensional BGK-Shakhov model which can be written as:

$$\partial_t f + u_1 \partial_{x_1} f = \frac{f^{+(0)} - f}{\tau}, \tag{2.3}$$

where $f$ is the particle velocity distribution function (vdf), $u_1$ is the particle velocity in the direction of $x_1$, $\tau$ is the mean collision time and $f^{+(0)}$ is the modified (due to Prandtl number fix of Shakhov [37]) equilibrium velocity distribution function (vdf). Note that the subscripts in $u_1$ and $x_1$ are dropped (and further denoted as $u$ and $x$) in this section for convenience. Then, the Maxwellian distribution for 1-D case is:

$$f^{(0)} = \rho \left(\frac{\lambda}{\pi}\right)^{\frac{K+1}{2}} e^{-\lambda\left((u-U)^2-\zeta^2\right)}, \tag{2.4}$$

where $\rho$ is the density, $\lambda = m/(2k_B T)$, $m$ is the molecular mass, $k_B$ is the Boltzmann constant, $U$ is the macroscopic velocity, $K$ is the number of internal degrees of freedom and $\zeta^2 = \sum_{i=1}^{K} \zeta_i^2$ is the energy associated with the internal degrees of freedom; and the modified equilibrium distribution is expressed as:

$$f^{+(0)} = f^{(0)} \left[1 + (1 - Pr)\, \mathbf{c}.\mathbf{q} \left(\frac{c^2}{RT} - 5\right) / \left(5pRT\right)\right], \tag{2.5}$$

where $Pr$ is the Prandtl number, $\mathbf{c}$ is the random (or thermal or peculiar) velocity, $\mathbf{q}$ is the heat flux, $R$ is the gas constant and $T$ is the temperature.

An integral solution of the BGK-Shakhov equation constructed via the method

of characteristics [35] is:

$$f\left(x,t,u,\zeta\right)=\frac{1}{\tau}\int_{t^n}^{t^{n+1}} f^{(0)}\big(x-u\big(t-t^{'}\big),t^{'},u,\zeta\big)e^{\frac{t^{'}-t}{\tau}}dt^{'} \\ +e^{\frac{t^n-t}{\tau}}f_0^n\big(x-u\big(t-t^n\big),t^n,u,\zeta\big), \tag{2.6}$$

where $f_0^n$ is the initial distribution function at $t^n$. The implementation of the finite volume method starts with the discretization of the physical, temporal and the particle velocity space which is collectively known as the phase space.

1. The physical space is divided into uniform structured cells where the $i^{th}$ cell has its center at $x_i$ and its left and right interfaces are denoted by $x_{i-1/2}$ and $x_{i+1/2}$ respectively. Hence the cell size $\Delta x_i = x_{i+1/2} - x_{i-1/2}$.

2. The discretized temporal space is represented by $t^n$ for the $n^{th}$ time-step.

3. The velocity space is divided into $2M+1$ cells with the cell size $\Delta u$. The center of $k^{th}$ velocity interval is $u_k = k\Delta u_k$. Hence, the cell averaged particle velocity at the $k^{th}$ cell,

$$u_k \in \left[\left(k-\frac{1}{2}\right)\Delta u_k, \left(k+\frac{1}{2}\right)\Delta u_k\right]; \quad k \in \mathbb{Z}\left[-M,M\right] \tag{2.7}$$

Using finite volume discretization in phase space and invoking the trapezoidal rule to approximate the collision term, the BGK-Shakhov difference equation takes the form:

$$f_{i,k}^{n+1} = f_{i,k}^n + \frac{1}{\Delta x}\int_{t^n}^{t^{n+1}}\left(f_{i-1/2,k}u_k - f_{i+1/2,k}u_k\right)dt \\ +\frac{\Delta t}{2}\left(\frac{f_{i,k}^{+(0)(n+1)} - f_{i,k}^{n+1}}{\tau^{n+1}} + \frac{f_{i,k}^{+(0)(n)} - f_{i,k}^{n}}{\tau^{n}}\right), \tag{2.8}$$

where $f_{i,k}^n$ and $f_{i,k}^{n+1}$ are the cell averaged distribution functions in the $i^{th}$ cell and $k^{th}$ discrete particle velocity ($u_k$), at $t^n$ and $t^{n+1}$ respectively. Here, $\Delta x$ is the cell size and $\Delta t$ is the time-step determined by CFL condition; $f_{i-1/2,k}$ and $f_{i+1/2,k}$ are the distribution functions across the cell interface which are computed using the integral solution of BGK-Shakhov equation (Equation 2.6). In the original UGKS, Van-Leer interpolation is used to determine the distribution ($f_0^n$ in Equation 2.6) at a particular cell interface. The Maxwellian distribution ($f^{(0)}$ in Equation 2.6) across the cell interface is approximated by Taylor's expansion in space and time. First order expansion of an equilibrium state is necessary to ensure the validity of UGKS over the entire Knudsen number regime. $f_{i,k}^{+(0)}$ and $\tau$ are modified equilibrium distributions and particle collision time respectively. Both quantities have a one-to-one correspondence with the instantaneous macroscopic properties. An evolution equation for the macroscopic properties can be obtained by taking the moments of the above BGK-Shakhov difference equation about the collision invariants ($\boldsymbol{\psi}$):

$$\boldsymbol{\psi} = \left(1, u, 0.5\left(u^2 + \zeta^2\right)\right)^T \tag{2.9}$$

Note that the moments of collision terms about the collision invariants must vanish in order to satisfy conservation laws.

$$\mathbf{Q}_i^{n+1} = \mathbf{Q}_i^n + \frac{1}{\Delta x}\left(\mathbf{F}_{i-1/2} - \mathbf{F}_{i+1/2}\right), \tag{2.10}$$

where $\mathbf{F} = \int_{t^n}^{t^{n+1}} \int \boldsymbol{\psi} f u d\Xi dt$, $\mathbf{Q} = \begin{pmatrix} \rho \\ \rho U \\ \rho E \end{pmatrix}$ and $d\Xi = du d\zeta_1 d\zeta_2 ... d\zeta_k$.

#### *2.2.1.1 WENO Implementation:*

One of the crucial operations in the UGKS is the interpolation of the distribution function to the cell interface. In high Mach number flows, interpolation can be challenging due to the presence of steep shocks. It is shown that Van-Leer interpolation produces spurious oscillations in the computed results at high Knudsen number. In this work, the implementation of $5^{th}$ order WENO (Weighted Essentially Non-Oscillatory) reconstruction schemes namely WENO-S of Shu [39] and WENO-C of Yamaleev and Carpenter [49] is presented. WENO uses a convex combination of all the candidate stencils neighboring a cell, each being assigned a non-linear weight which depends on the local smoothness of the numerical solution based on the corresponding stencil. This ensures non-oscillatory behavior near discontinuities without compromising the higher accuracy.

Figure 2.1 shows a typical computational stencil used for each reconstruction scheme. A second order Van-Leer limiter [41] uses the values stored at the immediate nodes neighbouring a cell interface to construct the value at the cell interface. For instance, the flux of the initial distribution function at $k^{th}$ velocity space at the right interface of $i^{th}$ cell is given by

$$q_{i+1/2,k} = q_{i,k} + (x_{i+1/2} - x_i)s_{i,k}, \tag{2.11}$$

where the slope $s_{i,k}$ is calculated from the Van-Leer scheme

$$s_{i,k} = (sign(s_1) + sign(s_2))\frac{|s_1||s_2|}{|s_1| + |s_2|}, \tag{2.12}$$

where

$$s_1 = \frac{q_{i,k} - q_{i-1,k}}{x_i - x_{i-1}} \text{ and } s_2 = \frac{q_{i+1,k} - q_{i,k}}{x_{i+1} - x_i}. \tag{2.13}$$

WENO-S scheme initially reconstructs the three values at the cell interface using the illustrated stencils $S_1$, $S_2$ and $S_3$. The final value at interface is then a convex combination of these values which are computed using weights that are specific for the scheme. WENO-C scheme is similar to WENO-S but avoids the bias of choosing three cells to the left of the interface and two from the right. Reconstruction based on this scheme can be computationally expensive as it involves calculations based on four stencils compared to that of WENO-S which uses only three stencils. However, WENO-C is known to lead to faster convergence [49].

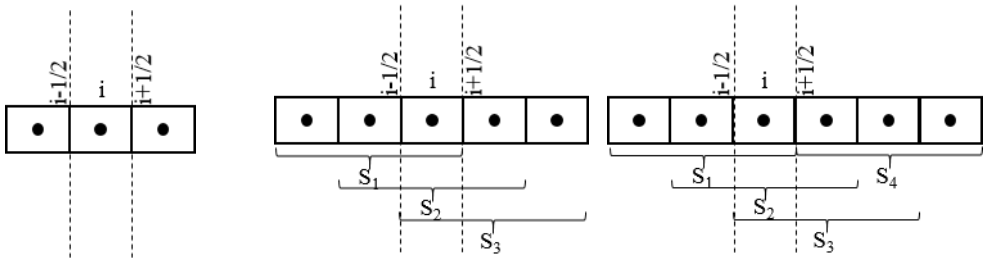


(a) Van-Leer (b) WENO-S (c) WENO-C

Figure 2.1: Computational stencils for different reconstruction schemes

#### *2.2.1.2 WENO-S and WENO-C:*

The WENO-C scheme is presented first and WENO-S can be derived from WENO-C with minor simplifications. WENO-C calculates the numerical flux (flux of initial distribution function in our case) at the interface ($x_{i+\frac{1}{2}}$) as a convex combination of four third order fluxes that are calculated based on the following three point stencils: $S^{(1)} = \{x_{i-2}, x_{i-1}, x_i\}$, $S^{(2)} = \{x_{i-1}, x_i, x_{i+1}\}$, $S^{(3)} = \{x_i, x_{i+1}, x_{i+2}\}$ and $S^{(4)} = \{x_{i+1}, x_{i+2}, x_{i+3}\}$. Note that the collection of all four stencils is symmetric

with respect to $x_{i+\frac{1}{2}}$. The WENO-C flux of any quantity $q$ is then given by

$$q_{i+\frac{1}{2}} = w^{(1)} q^{(1)}_{i+\frac{1}{2}} + w^{(2)} q^{(2)}_{i+\frac{1}{2}} + w^{(3)} q^{(3)}_{i+\frac{1}{2}} + w^{(4)} q^{(4)}_{i+\frac{1}{2}} \tag{2.14}$$

where $q^{(r)}_{i+\frac{1}{2}}$ is the $3^{rd}$ order flux defined by the stencil $S^{(r)}$ $(r = 1, 2, 3, 4)$

$$\begin{pmatrix} q^{(1)}_{i+\frac{1}{2}} \\ q^{(2)}_{i+\frac{1}{2}} \\ q^{(3)}_{i+\frac{1}{2}} \\ q^{(4)}_{i+\frac{1}{2}} \end{pmatrix} = \frac{1}{6} \begin{pmatrix} 2 & -7 & 11 & 0 & 0 & 0 \\ 0 & -1 & 5 & 2 & 0 & 0 \\ 0 & 0 & 2 & 5 & -1 & 0 \\ 0 & 0 & 0 & 11 & -7 & 2 \end{pmatrix} \begin{pmatrix} q_{i-2} \\ q_{i-1} \\ q_i \\ q_{i+1} \\ q_{i+2} \\ q_{i+3} \end{pmatrix} \tag{2.15}$$

and the weight function is given by

$$w^{(r)} = \frac{b^{(r)}}{\sum_{m=1}^{4} b^{(r)}}, \tag{2.16}$$

$$b^{(r)} = d^{(r)} \left( 1 + \frac{p}{\epsilon + \beta^{(r)}} \right), \quad \epsilon = 10^{-6}, \tag{2.17}$$

$$d^{(1)} = \frac{1}{10} - \Delta, \quad d^{(2)} = \frac{6}{10} - 3\Delta, \quad d^{(3)} = \frac{3}{10} + 3\Delta, \quad d^{(4)} = \Delta. \tag{2.18}$$

The functions $\beta^{(r)}$ are the smoothness indicators and are given by

$$\beta^{(1)} = \frac{13}{12} \left( q_{i-2} - 2q_{i-1} + q_i \right)^2 \quad + \quad \frac{1}{4} \left( q_{i-2} - 4q_{i-1} + 3q_i \right)^2 \tag{2.19a}$$

$$\beta^{(2)} = \frac{13}{12} \left( q_{i-1} - 2q_i + q_{i+1} \right)^2 \quad + \quad \frac{1}{4} \left( q_{i-1} - q_{i+1} \right)^2 \tag{2.19b}$$

$$\beta^{(3)} = \frac{13}{12} \left( q_i - 2q_{i+1} + q_{i+2} \right)^2 \quad + \quad \frac{1}{4} \left( 3q_i - 4q_{i+1} + 3q_{i+2} \right)^2 \tag{2.19c}$$

$$\beta^{(4)} = \frac{13}{12} \left( q_{i+1} - 2q_{i+2} + q_{i+3} \right)^2 + \quad \frac{1}{4} \left( -5q_{i+1} + 8q_{i+2} - 3q_{i+3} \right)^2 \tag{2.19d}$$

and the expression for $p$ is given by

$$p = \begin{cases} \left(-q_{i-2} + 5q_{i-1} - 10q_i + 10q_{i+1} - 5q_{i+2} + q_{i+3}\right)^2 & for \quad \Delta \neq 0 \\ \left(q_{i-2} - 4q_{i-1} + 6q_i - 4q_{i+1} + q_{i+2}\right)^2 & for \quad \Delta = 0 \end{cases} \tag{2.20}$$

The value of $\Delta$ affects the convergence rate and for the specific value of $\Delta_c = \frac{1}{20}$, the convergence rate is 6 [49]. Hence, all WENO-C simulations will be performed with $\Delta = \frac{1}{20}$. It can be proved that the classical fifth-order upwind-biased WENO-S scheme of Shu [39] is obtained by setting $\Delta = 0$. It should be noted that the WENO reconstruction to the left interface to obtain $q_{i-\frac{1}{2}}$ is mirror symmetric with respect to $x_i$ of the above procedure [39].

The flux of the initial distribution function at the cell interface at $x_{i+1/2}$ is selected based on the direction of the mean particle velocity in the corresponding velocity space $u_k$:

$$q_{i+1/2,k} = \begin{cases} q_{i+1/2,k}^{(left)} & if \quad u_k \geq 0 \\ \\ q_{i+1/2,k}^{(right)} & if \quad u_k < 0 \end{cases} \tag{2.21}$$

The actual implementation and a step-by-step algorithm of UGKS is explained in detail in Appendix A.

### *2.2.2 Direct Simulation Monte Carlo (DSMC)*

The DSMC method represents real gas flow using a large number of simulated particles. This method is one way to realize physical processes modeled by the Boltzmann equation. The DSMC method, similar to other Monte Carlo schemes, is a statistical approach whose solutions are shown to converge towards the analytical solutions of Boltzmann equation with sufficiently large number of samples. The number of simulated molecules is much smaller than the number of real molecules present

in the flow. Appropriate choice of collision partners and effecting sufficient number of collisions during one time step in a cell guarantee a reasonable facsimile of the real flow. The intermolecular collisions are treated on a probabilistic rather than a deterministic basis and are subject to the 'molecular chaos' ansatz. The essential DSMC approximation is the uncoupling, over a small time interval or step, of molecular streaming and intermolecular collisions. The position coordinates, velocity components and internal state of each molecule evolve in time subject to representative collisions within the domain and due to boundary interactions.

A typical DSMC implementation can be briefly described as follows. A physical flow domain with appropriate boundaries is described. The computational domain is divided into cells used for selecting collision partners and over which the particle properties are averaged to obtain macroscopic properties. The physical domain is initialized by specifying the number of simulated particles and assigning initial position and velocity values according to an equilibrium probability density function calculated from the given flow conditions. The simulation then proceeds, stepping through time as follows:

1. The particles are advected according to the velocity and time step size.

2. Boundary conditions, such as collisions with walls, inflow and outflow, are applied.

3. Particle collisions (elastic and inelastic) are computed based on collision probabilities and molecular models.

4. Macroscopic flow field variables are evaluated by averaging over the properties of the individual particles.

This procedure involves certain assumptions and limitations. First, the time

step must be smaller than the mean collision time such that the particle movements and the collision operations can be separated. This entails the time step to be approximately one-third of the mean collision time. Second, the collision partners are chosen among the particles in each cell. Consequently, each cell should be less than one mean free path in size. Collision partners can then be randomly chosen from the particles in each cell while maintaining physical accuracy. Third, each cell should contain sufficient particles such that the macroscopic averages are statistically meaningful. Generally 20 to 25 particles per cell are required. Further, when the mean flow speed is much lesser than the corresponding molecular speed, the DSMC method is subject to significant statistical fluctuations. By its very nature, DSMC is well suited for high-speed rarefied flows. However, those very features render DSMC computationally expensive for continuum, near-continuum or low-speed flows. More details on DSMC can be found in Bird [7].

# 3. FLOW STRUCTURES IN RAREFIED CAVITY FLOWS*

WENO enhanced UGKS is employed to simulate the canonical problem of lid-driven cavity flow exposed to a wide range of Mach and Knudsen numbers. Direct Simulation Monte Carlo (DSMC) computations are also performed when appropriate for comparison. The effect of aspect ratio, Knudsen number and Mach number on cavity flow physics is examined leading to important insights.

## 3.1 Introduction

The main objectives of the chapter are to: (i) extend the applicability of UGKS by implementing, testing and verifying a WENO (weighted essentially non-oscillatory) interpolation scheme; and (ii) examine the effect of Mach number, Knudsen number and aspect ratio on the flow characteristics in a lid-driven cavity flow. In the first part, various WENO variants [39, 49] are compared against the original Van Leer scheme [41] to establish the applicability of the different interpolation schemes. Then the UGKS is compared against the well-established DSMC solver OpenFOAM (dsmcFOAM) at high Knudsen numbers. Once the verification is complete, the UGKS solver is used to investigate the flow features within a cavity at different conditions. This work addresses mostly two-dimensional flows for ease of numerical scheme development and verification/validation. Clearly further three-dimensional studies are needed for complete investigation of flow physics.

*Reprinted with permission from Cambridge University Press. Full citation: Venugopal, Vishnu, and Sharath S. Girimaji. 'Unified Gas Kinetic Scheme and Direct Simulation Monte Carlo Computations of High-Speed Lid-Driven Microcavity Flows.' Communications in Computational Physics 17.05 (2015): 1127-1150.

## 3.2 Numerical Setup and Simulation Parameters

We simulate the flow of Argon gas within a cavity driven by a lid moving at a constant velocity of $U_{lid}$. The degree of rarefaction is set using the global (freestream) Knudsen number, which is the ratio between the mean free path of the molecules in the freestream ($\lambda_\infty$) to the global length scale ($L$).

$$Kn_{global} = \frac{\lambda_\infty}{L} \tag{3.1}$$

Global length scale for this problem is defined as the characteristic width of the cavity, which is of the order of one micron. Hence, a 2D square cavity, would have the dimensions of $10^{-6}m \times 10^{-6}m$ (Figure 3.1). All cavity walls including the lid are set to be isothermal maintaining a temperature of $T_{wall}$. The dimensions of cavities with various aspect ratios ($AR$, defined as the ratio of height to width of the cavity) simulated in the present study are given in Table 3.1. The list of various simulation conditions is given in Tables 3.2 and 3.3.

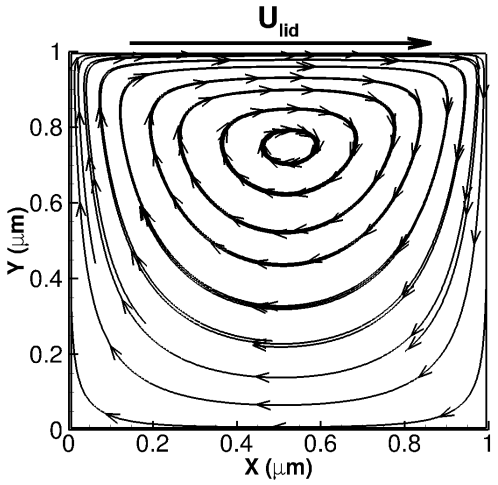


Figure 3.1: Cavity geometry

| $\boldsymbol{AR}$ | **Height** | **Width** |
|---|---|---|
| 1.0 | 1.0 | 1.0 |
| 0.4 | 1.0 | 2.5 |
| 2.5 | 2.5 | 1.0 |

Table 3.1: Dimensions in microns for wide and narrow cavities

| $\boldsymbol{AR}$ | $\boldsymbol{Kn}_{global}$ | $\boldsymbol{Mach}_{lid}$ | $\boldsymbol{T}_{wall}$ $(K)$ |
|---|---|---|---|
| 1.0 | 0.05 | 0.3 | 300 |
| 1.0 | 0.5 | 0.3 | 300 |
| 1.0 | 1.0 | 0.3 | 300 |
| 1.0 | 10.0 | 0.3 | 300 |

Table 3.2: Simulation parameters for validation cases

| $\boldsymbol{AR}$ | $\boldsymbol{Kn}_{global}$ | $\boldsymbol{Mach}_{lid}$ | $\boldsymbol{T}_{wall}$ $(K)$ |
|---|---|---|---|
| 0.4 | 0.005 | 0.3 | 273 |
| 0.4 | 0.05 | 0.3 | 273 |
| 0.4 | 1.0 | 0.3 | 273 |
| 0.4 | 10.0 | 0.3 | 273 |
| 0.4 | 0.005 | 3.0 | 273 |
| 0.4 | 0.05 | 3.0 | 273 |
| 0.4 | 1.0 | 3.0 | 273 |
| 0.4 | 10.0 | 3.0 | 273 |
| 2.5 | 0.005 | 0.3 | 273 |
| 2.5 | 0.05 | 0.3 | 273 |
| 2.5 | 1.0 | 0.3 | 273 |
| 2.5 | 10.0 | 0.3 | 273 |
| 2.5 | 0.005 | 3.0 | 273 |
| 2.5 | 0.05 | 3.0 | 273 |
| 2.5 | 1.0 | 3.0 | 273 |
| 2.5 | 10.0 | 3.0 | 273 |

Table 3.3: Simulation parameters for studies on cavity flow physics

### *3.2.1 DSMC Implementation*

The grid spacing in any direction is one-hundredth of a micron for DSMC simulations so that the cell size is never more than the freestream mean free path

($\lambda_\infty$).The time step for DSMC calculations is on the order of mean collision time of the freestream molecules, $\tau_\infty$ and intrinsic gas properties such as freestream number density ($n_\infty$), $\lambda_\infty$ and mean collision time ($\tau_\infty$). are calculated assuming a Variable Hard Sphere (VHS) binary collision model (Table 3.4, Eqn. 3.2, Eqn. 3.3).

$$\lambda_\infty = \frac{1}{\sqrt{2}\pi d_{ref}^2 n_\infty} \tag{3.2}$$

$$\tau_\infty = \frac{1}{\pi d_{ref}^2 n_\infty \bar{c}_{r\infty}}, \tag{3.3}$$

where $\bar{c}_{r\infty} = \left(\frac{16kT_{ref}}{\pi m}\right)^{1/2}$ is the mean magnitude of the relative velocity of colliding molecules in freestream condition [7]. DSMC models the gas-boundary interaction using diffuse reflection model with complete thermal accommodation. The fraction determining number of real molecules represented by a simulated molecule is defined such that the average number of simulated molecules per cell is at least 25. This is to maintain a good acceptance rate of the collision partners being selected from a particular cell, and also to make a meaningful statistical averaging among the molecules in a cell. Simulations in 2D physical space must be performed carefully. Apart from grid sensitivity studies, it is equally important to confirm that one is not missing to capture any three dimensional flow features. Possibility of 3D effects are high in our case since we deal with highly non-equilibrium flows with multiple vortex structures. However, in the following part, it is seen that our flow structures are free from any 3D effects ensuring accurate results with corresponding 2D simulations. Collisions are calculated based on Variable Hard Sphere (VHS) binary collision model.

| | |
|---|---|
| Molecular mass, $m$ | $66.3 \times 10^{-27} kg$ |
| Reference diameter, $d_{ref}$ | $4.17 \times 10^{-10} m$ |
| Reference temperature, $T_{ref}$ | $273K$ |
| Viscosity index, $\omega_{VHS}$ | 0.81 |
| Diffusion index, $\alpha_{VHS}$ | 1.0 |

Table 3.4: Molecular properties for Argon gas

### *3.2.2 UGKS Implementation*

Based on grid sensitivity studies, the grid size for the UGKS computations was chosen to be 0.09 microns. The time-step is calculated from the CFL condition with a CFL number of 0.9. The Prandtl number is set to 2/3. A set of 28 weights based on Gauss-Hermite quadrature is used for numerical integration over the discrete velocity space in each direction [38]. The mean collision time ($\tau$) for each cell is defined as the ratio of corresponding dynamic viscosity coefficient ($\mu_{VHS}$) to the macroscopic pressure ($p$).

$$\tau = \frac{\mu_{VHS}}{p}, \tag{3.4}$$

$$p = \frac{1}{3} \int \left( (u - U)^2 + \zeta^2 \right) f d\Xi, \tag{3.5}$$

and $\mu_{VHS}$ is given by Sutherland's law

$$\mu_{VHS} = \mu_{ref} \left( \frac{T}{T_{ref}} \right)^{\omega_{VHS}}, \tag{3.6}$$

where $\mu_{ref}$ for Variable Hard Sphere (VHS) collision model is given by [7],

$$\mu_{ref} = \frac{5(\alpha_{VHS}+1)(\alpha_{VHS}+2)\sqrt{\pi}}{4\alpha_{VHS}(5-2\omega_{VHS})(7-2\omega_{VHS})} Kn_{global}. \tag{3.7}$$

The diffuse-wall boundary condition in UGKS is realized from the logic of impermeability condition. A particular computational cell attached to the left wall is considered for illustration purpose. The no-penetration condition then demands that

$$\sum_{k:\ u_k>0} u_k f_{w,k}^{(0)} \ + \sum_{k:\ u_k<0} u_k f_{w,k}^{in} = 0, \tag{3.8}$$

$f_{w,k}^{(0)}$ is the Maxwellian-type distribution function at the wall in the $k^{th}$ velocity space

$$f^{(0)_{w,k}} = \rho_w \left(\frac{\lambda_w}{\pi}\right)^{\left(\frac{K+1}{2}\right)} e^{-\lambda_w\left((u_k-U_w)^2+\zeta^2\right)}, \tag{3.9}$$

where the subscript $w$ denotes that the properties are at the wall. $f_{w,k}^{in}$ is the incoming distribution function from the right side of the wall-interface which is obtained based on a one-sided interpolation from the interior region. Density at the wall $\rho_w$ is then computed from Equation 3.8 to satisfy the impermeability condition. The corresponding Maxwellian distribution at the wall can then be calculated from Equation 3.9. The distribution function at this boundary is then expressed as

$$f_{w,k} = \begin{cases} f^{(0)_{w,k}} & if \quad u_k \geq 0 \\ \\ f_{w,k}^{in} & if \quad u_k < 0 \end{cases} \tag{3.10}$$

Finally, the fluxes $\boldsymbol{F_w}$ across the walls can be obtained from usual procedure

$$\boldsymbol{F_w} = \int_{t^n}^{t^{n+1}} \int \boldsymbol{\psi} f u d\Xi dt. \tag{3.11}$$

## 3.3 Results and Discussion

The main objective of this study is to provide numerical verification of the UGKS-WENO implementation. Such verification can be most conveniently established in 2D simulations. Due to relatively low computational burden, wide range of verifications can be performed with 2D simulations. As a first step, we compare 2D simulations with 3D computations to establish that the former can capture important aspect of flow physics seen in the latter. Thus, we perform a comparison between 2D and 3D simulation results before proceeding to a more exhaustive verification/validation study with only 2D simulations. Finally, we present one set of results for $100 \times 100$ discrete velocity Newton-Cotes quadrature scheme.

### *3.3.1 Comparison between 2D and 3D Simulations*

A microcavity simulation of the case with lid velocity of $Mach$ 0.3 and $Kn$ 10 is performed in 3D domain with periodic boundary conditions in the spanwise dimension ($Z$). The simulation is performed using OpenFOAM. The domain is divided into $100 \times 100 \times 100$ sampling cells. Figure 3.2(a) shows the mean-velocity profiles along mid-horizontal and mid-vertical lines at different Z-planes. These profiles are also compared with corresponding 2D DSMC and 2D UGKS simulations in Figure 3.2(a). Absence of any 3D effects is clearly seen since the mean-profiles are the same with each and every case. Figures 3.2(b), 3.2(c) and 3.2(d) show the x, y and z vorticity contours respectively. Note that the x and y vorticity fields are purely random and distributed symmetrically over the entire domain. Also, their average magnitude is very small compared to z-vorticity field. This clearly indicates that 2D simulations can indeed capture aspects of 3D flow physics. Through the remainder of this section, we will restrict ourselves to 2D simulations for the verification and flow physics studies.

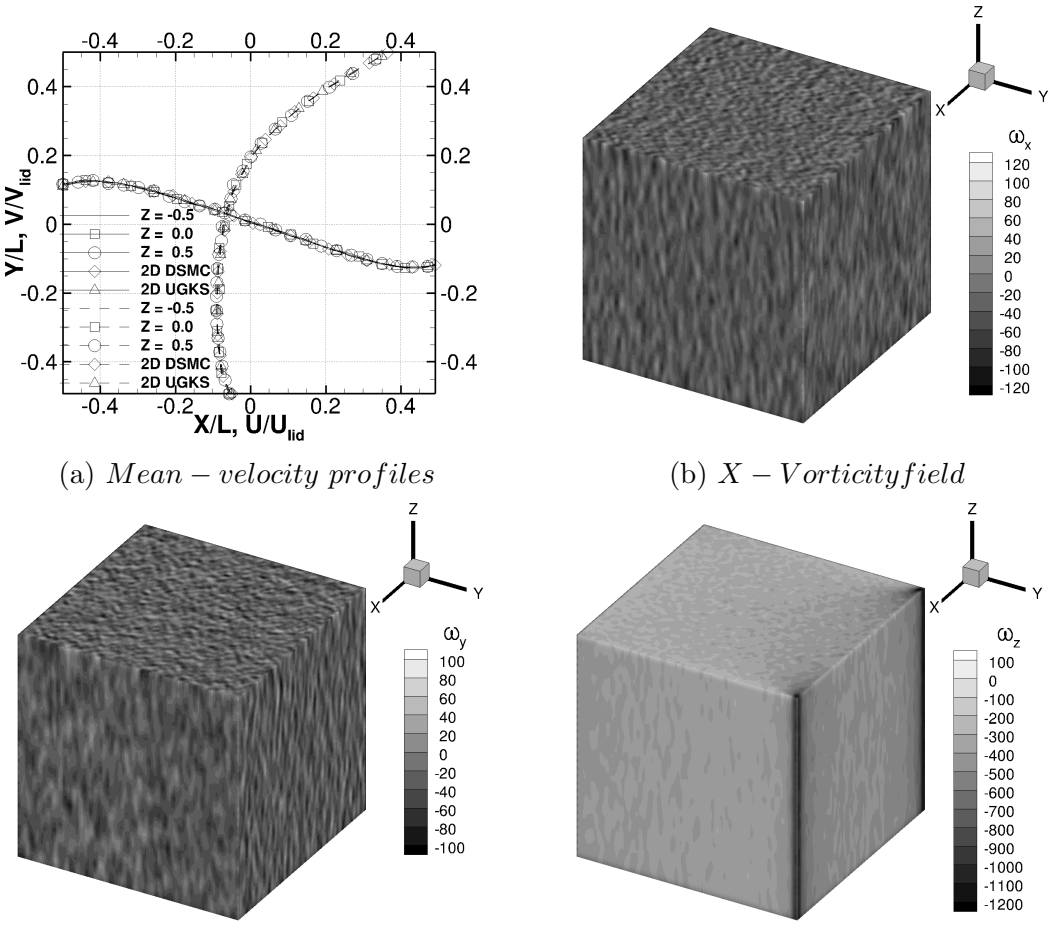


(a) $Mean - velocity\ profiles$

(b) $X - Vorticity field$

(c) $Y - Vorticity field$

(d) $Z - Vorticity field$

Figure 3.2: Observing 3D effects

### *3.3.2 Verification Results*

Basic verifications of UGKS has been performed in Xu and Huang [46]. It is shown that the scheme performs well in continuum and rarefied regimes. Here, we extend the validation to a larger range of Knudsen numbers. To enable this wider range, different WENO interpolation schemes are investigated.

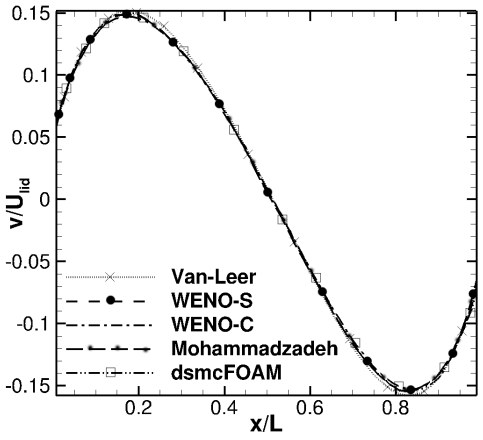


(a) $Kn = 0.05$

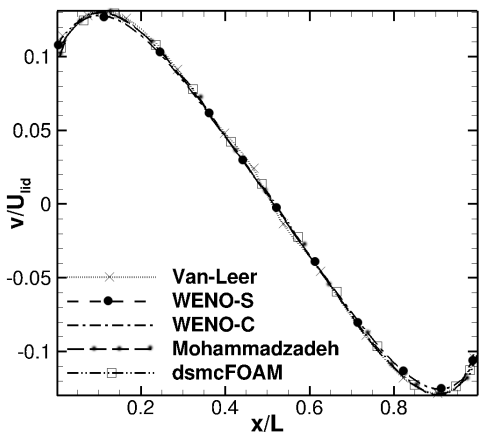


(b) $Kn = 0.5$

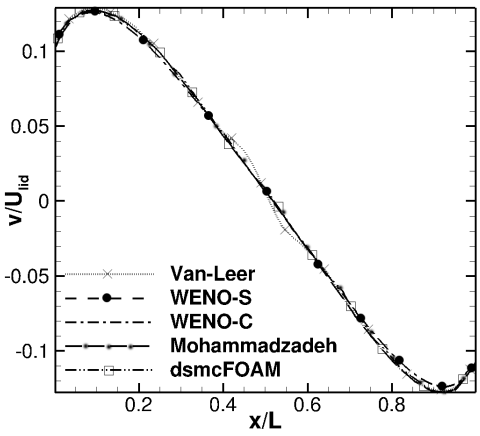


(c) $Kn = 1.0$

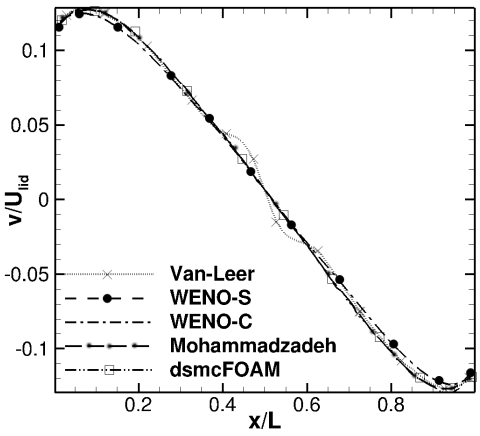


(d) $Kn = 10.0$

Figure 3.3: V-velocity profile along mid-horizontal line

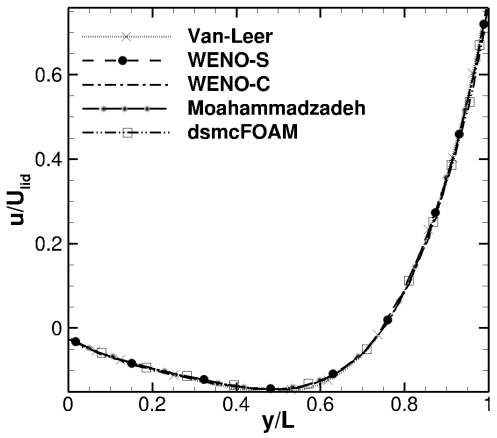


(a) $Kn = 0.05$

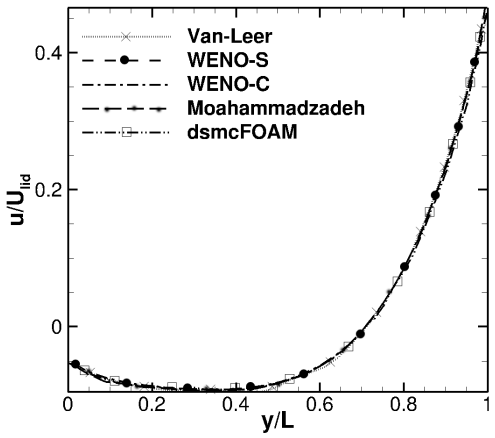


(b) $Kn = 0.5$

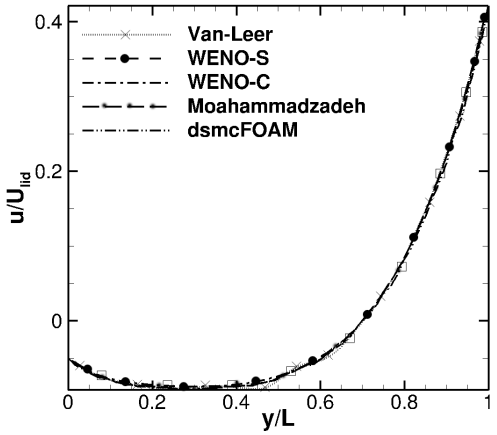


(c) $Kn = 1.0$

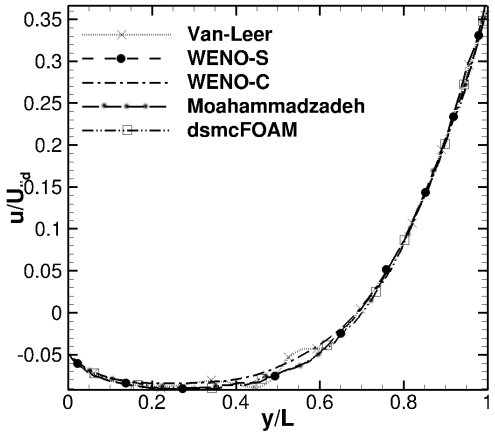


(d) $Kn = 10.0$

Figure 3.4: U-velocity profile along mid-vertical line

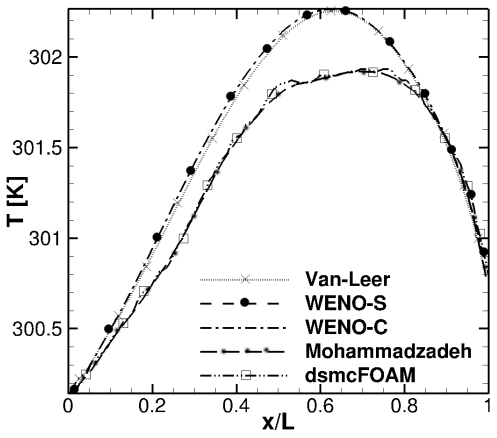


(a) $Kn = 0.05$

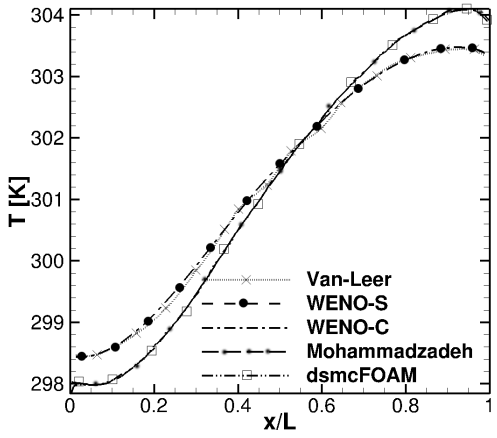


(b) $Kn = 0.5$

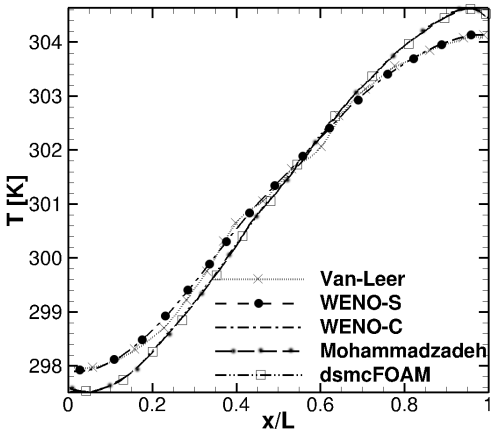


(c) $Kn = 1.0$

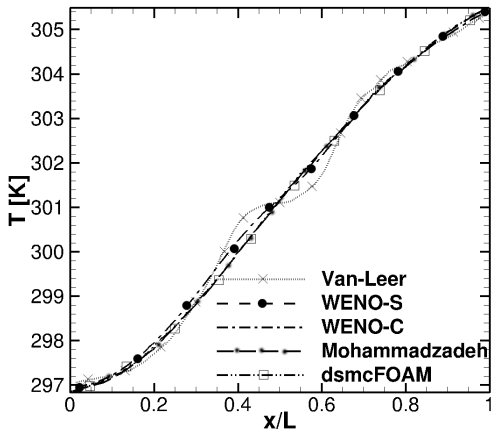


(d) $Kn = 10.0$

Figure 3.5: Temperature profile along mid-horizontal line

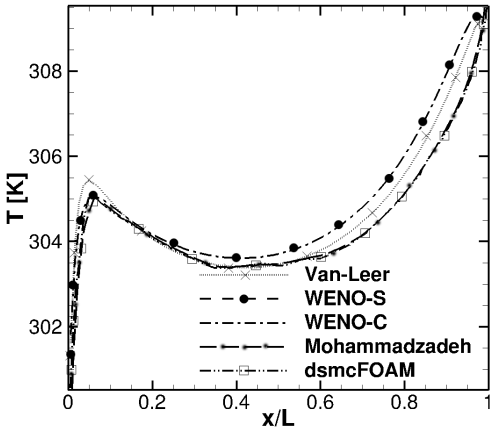


(a) $Kn = 0.05$

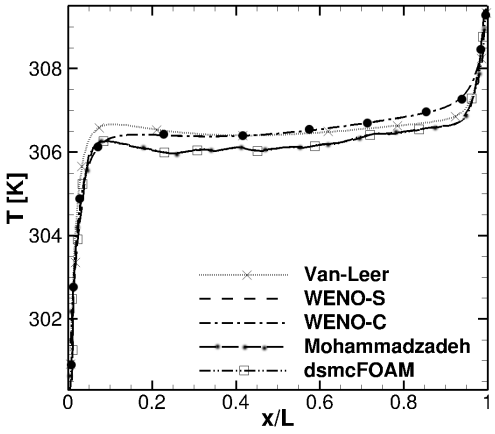


(b) $Kn = 0.5$

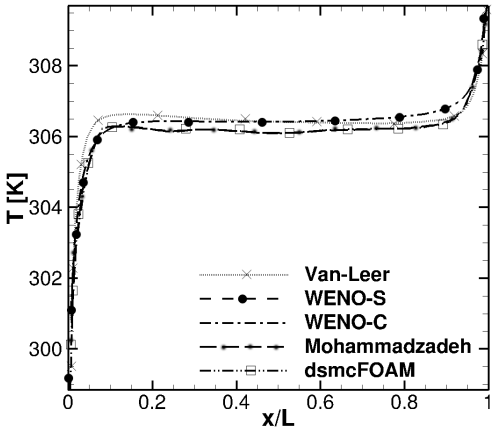


(c) $Kn = 1.0$

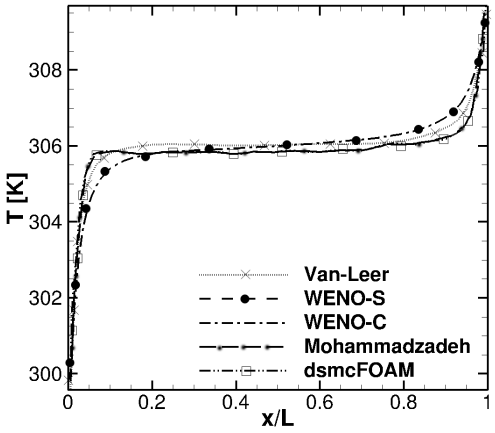


(d) $Kn = 10.0$

Figure 3.6: Temperature profile along the lid

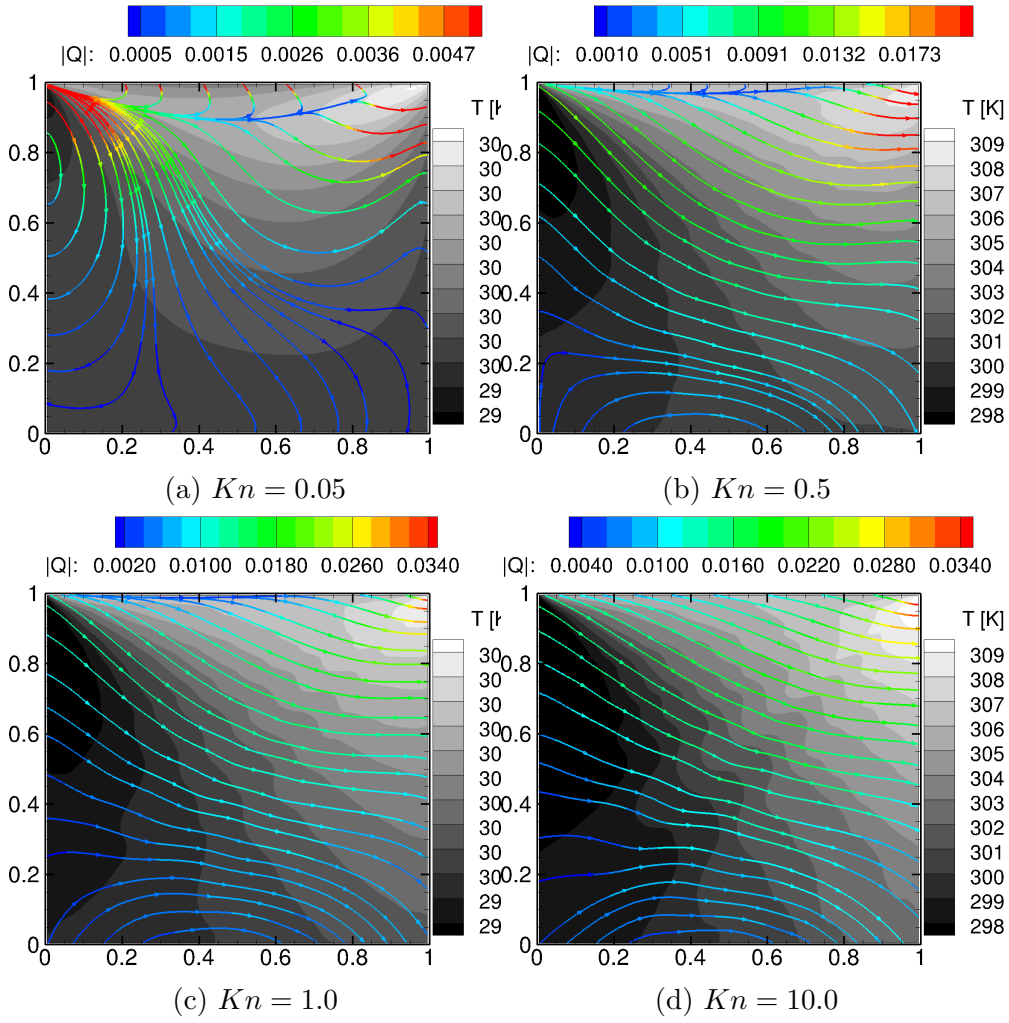


(a) $Kn = 0.05$ (b) $Kn = 0.5$

(c) $Kn = 1.0$ (d) $Kn = 10.0$

Figure 3.7: Temperature contours overlaid with heat-flux lines (Van-Leer)

The results from Van-Leer and WENO computations are compared against those from DSMC computations of (a) OpenFOAM (dsmcFOAM) and (b) the results of Mohammadzadeh et al. [29]. Figures 3.3, 3.4, 3.5 and 3.6 show that the velocity and temperature profiles (along the mid-vertical line, mid-horizontal line and lid surface) generated by UGKS agrees well with those of the corresponding DSMC simulations. Slight deviations in temperature profiles of DSMC from that of UGKS at low global Knudsen numbers (Figures 3.5 and 3.6) can be attributed to the inadequacies (of

cell-size, time-step and the number of particles per cell) of DSMC at near-continuum regime. Such slight deviations have also been reported by Bartel et al. [4] where DSMC simulations conducted in continuum regime to compute an expanding jet flow. The main advantage of UGKS over DSMC at low Knudsen numbers is also evident from the computational time required for the simulations. For low global Kn numbers, DSMC simulations with openFOAM were at least ten times computationally more expensive than a corresponding UGKS based simulation.

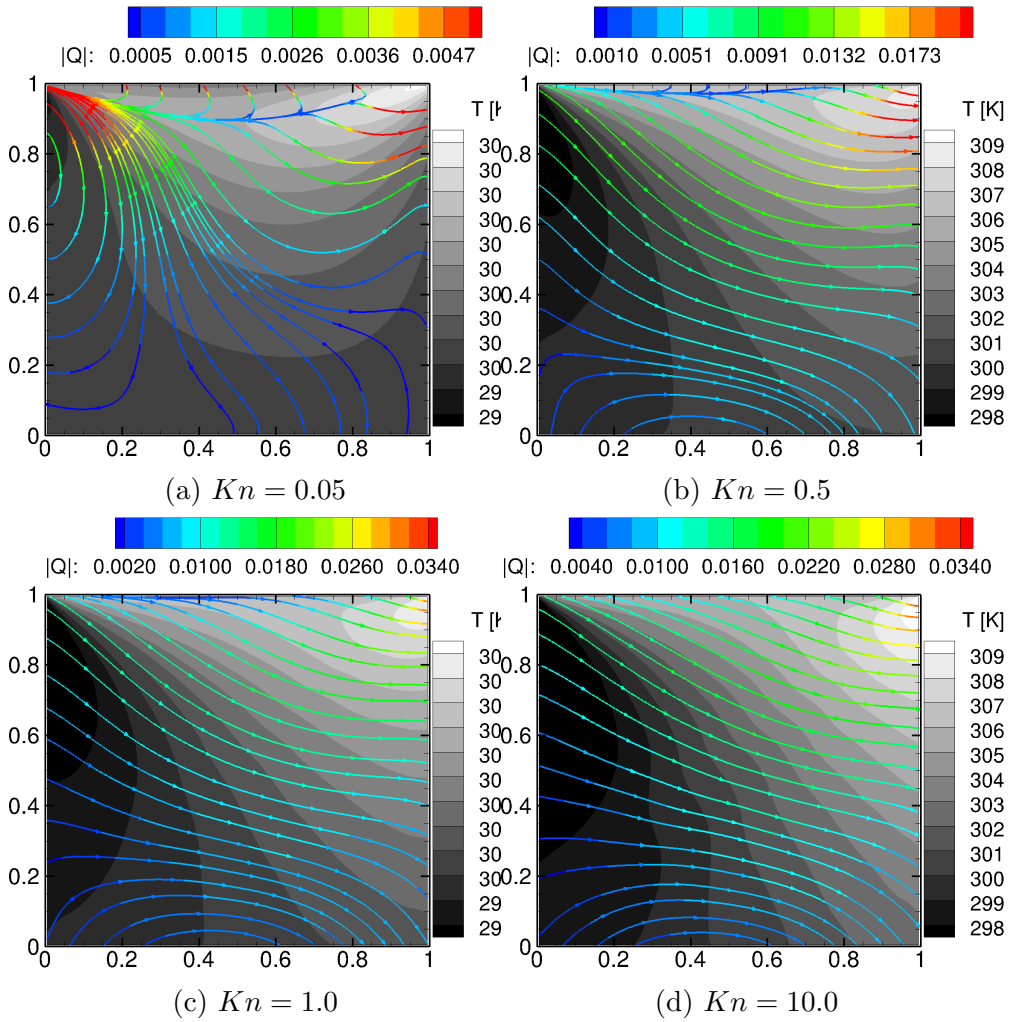


(a) $Kn = 0.05$ (b) $Kn = 0.5$

(c) $Kn = 1.0$ (d) $Kn = 10.0$

Figure 3.8: Temperature contours overlaid with heat-flux lines (WENO-S)

As can be seen from Figures 3.3, 3.4 and 3.5, UGKS with Van-Leer scheme shows undesirable oscillations, that become prominent at high Knudsen numbers. These spurious oscillations are eliminated when higher order WENO reconstruction scheme is employed. Moreover, at higher Knudsen numbers, UGKS with Van-Leer scheme has a much slower rate of convergence compared to WENO-S or WENO-C schemes. A better illustration of the smoothing effect of WENO schemes can be seen by comparing Figure 3.7 and Figure 3.8, which shows the temperature contours overlaid with the heat-flux lines (colored with heat-flux magnitude). Detailed discussion on the origination and possible means of removal of these non-physical oscillations are presented in section 3.3.4. The inference is that UGKS with a WENO-based reconstruction scheme is necessary at high Knudsen number regimes. WENO-S and WENO-C produce nearly identical profiles for velocity and temperature. Also, it is noted that these two schemes give similar steady-state values for all macroscopic properties throughout the domain. The main distinction between the two WENO methods is in the rate of convergence. WENO-C leads to a more rapid convergence. However, WENO-C is computationally expensive since it uses an extra stencil to interpolate the flux data to the cell interface. Throughout the reminder of this article, we present results from WENO-S which was found to be adequate for current simulations.

### *3.3.3 Cavity Flow Physics*

Micro-cavities of practical interest come in many shapes and sizes. The nature of flow inside these cavities depend critically on the shape. To understand the influence of shape, we simplify the cavity geometry to rectangles of different aspect ratios shown in Table 3.1. Flows within these cavities are simulated at different Mach and Knudsen numbers, and the results are examined.

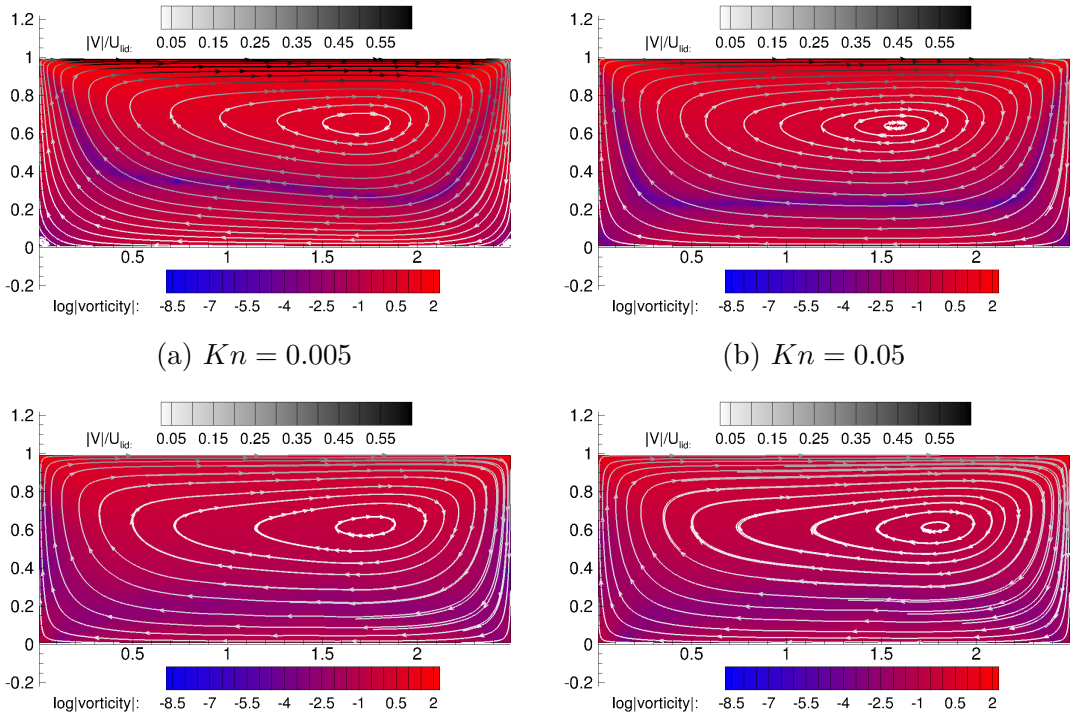


(a) $Kn = 0.005$ (b) $Kn = 0.05$

(c) $Kn = 1$ (d) $Kn = 10$

Figure 3.9: Vortex structures for $AR = 0.4,\ Mach_{lid} = 0.3$

Figures 3.9, 3.10, 3.11 and 3.12 show the streamlines colored with the normalized velocity magnitude for wide and deep cavities at different Knudsen and Mach numbers. The background contour illustrates the varying strength of $z$-vorticity normalized by $U_{lid}/L$. Note that the contour levels for $z$-vorticity are set in logarithmic scale indicating a large range of $z$-vorticity strength (of about 10 orders of magnitude) within the cavity. Comparison between these sets of figures reveal important Mach and Knudsen number effects.

It can be clearly seen that a wide cavity, on an average, has a higher streamwise velocity as well as $z$-vortex strength when compared to a similar case (of same Knudsen and Mach numbers) with a deep cavity. However, this behavior is expected

since the rate at which momentum gets transferred from the moving lid to molecules within the cavity is high for wide cavities owing to its large lid stroke for given area. Thus, the lid transfers more momentum to the cavity fluid. The flow in wide cavities approach steady state more readily and exhibit a stable configuration involving a single large primary vortex. This was not the case with deep cavities where most of the simulations triggered the formation of a second vortex.

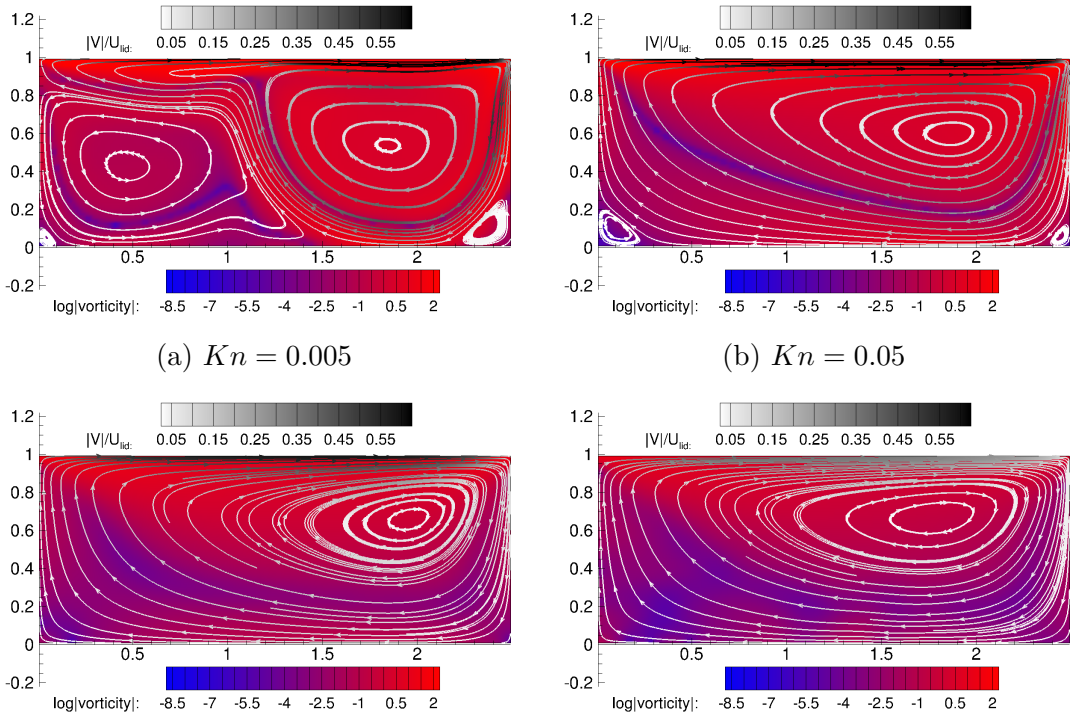


(a) $Kn = 0.005$ (b) $Kn = 0.05$

(c) $Kn = 1$ (d) $Kn = 10$

Figure 3.10: Vortex structures for $AR = 0.4$, $Mach_{lid} = 3.0$

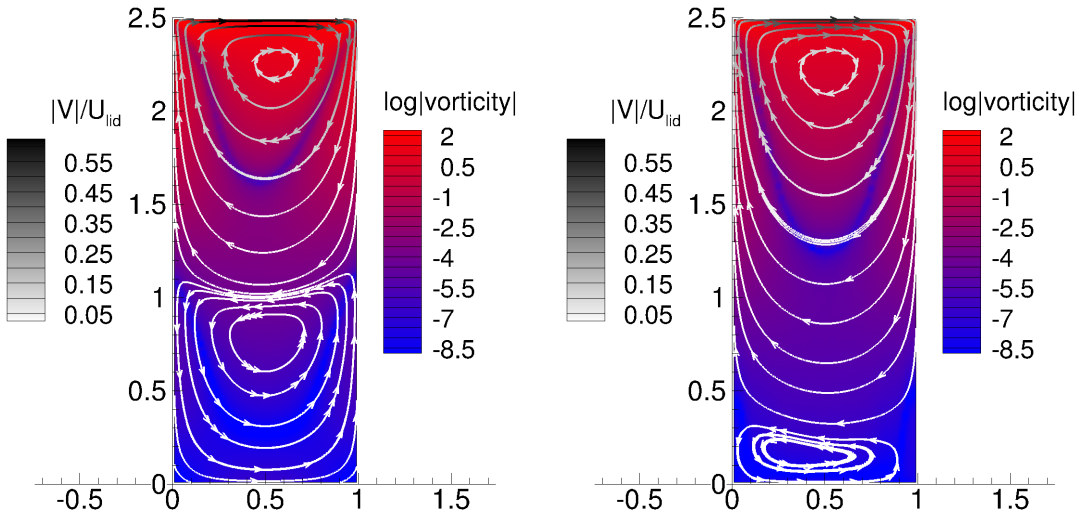


(a) $Kn = 0.005$ (b) $Kn = 0.05$

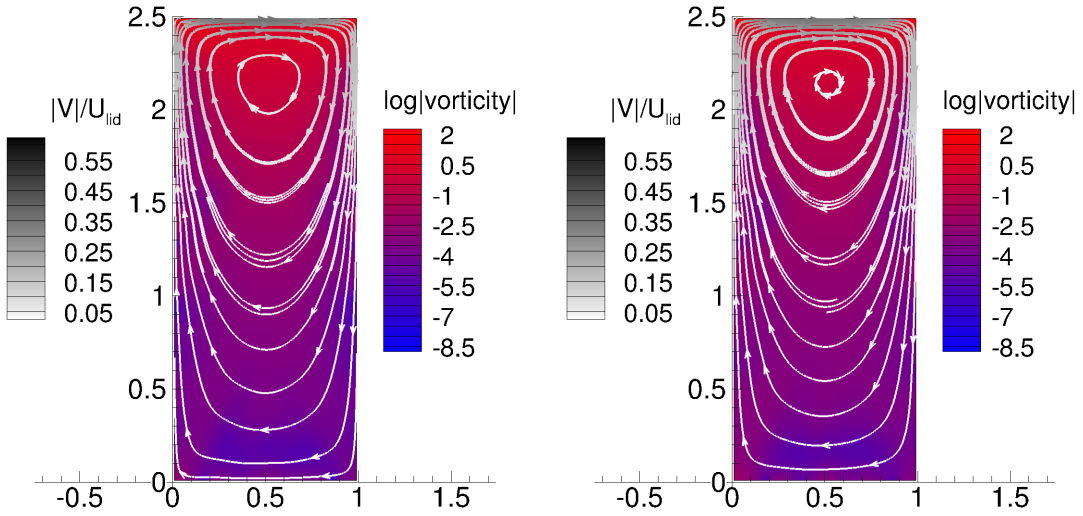


(c) $Kn = 1$ (d) $Kn = 10$

Figure 3.11: Vortex structures for $AR = 2.5,\ Mach_{lid} = 0.3$

At a constant lid velocity, the number of active vortices decrease with an increase of global Knudsen number. The mechanism that creates additional vortices for flows near continuum regimes is clearly demonstrated in Figures 3.10 (b) and 3.12 (b). It

is seen that for $AR = 0.4$ (Figure 3.10 (b)), secondary eddies have been created at the two bottom corners under the main vortex. As the aspect ratio is increased to 2.5, these secondary eddies grow and merge into a second vortex under the main one.

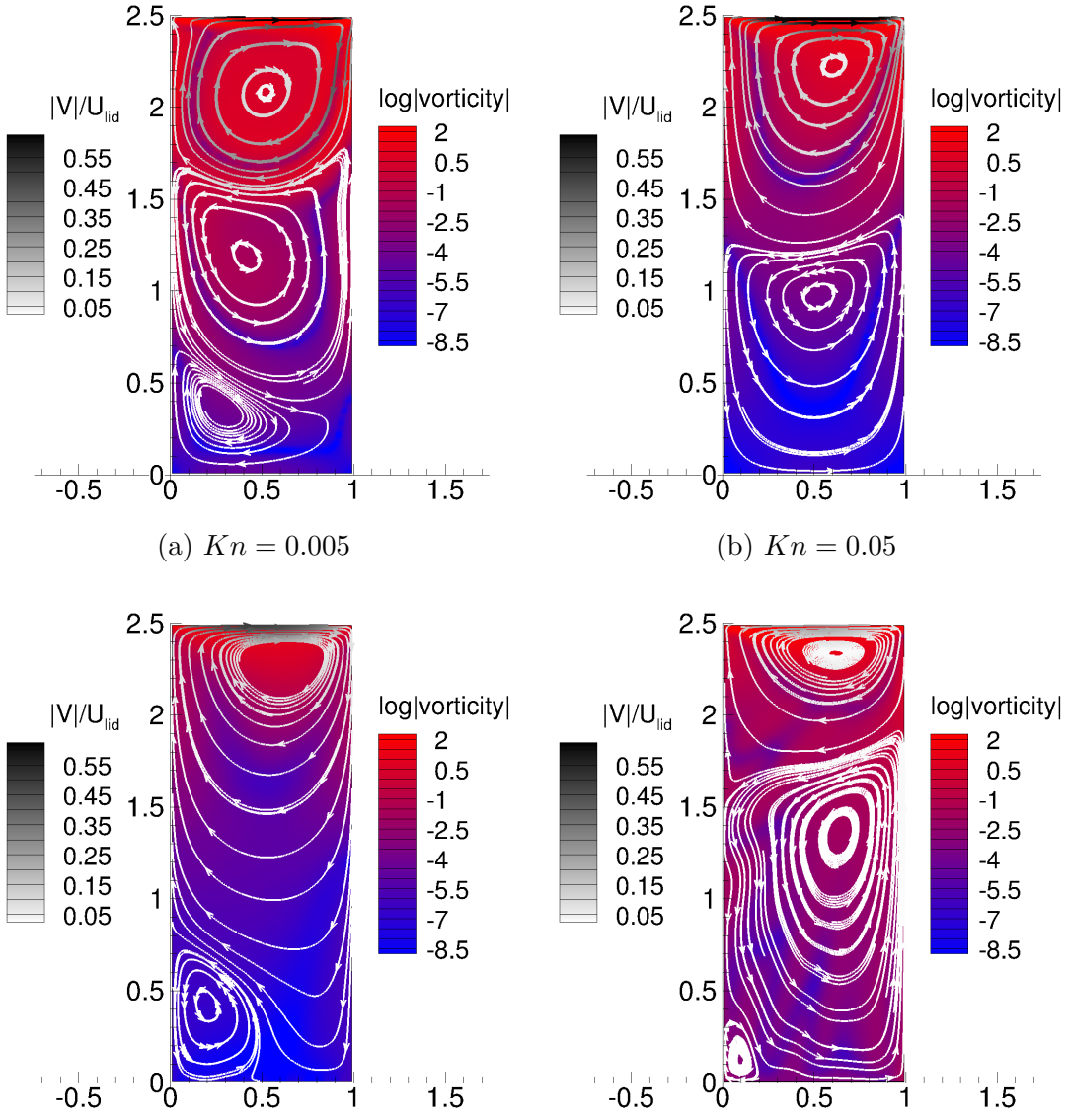


(a) $Kn = 0.005$ (b) $Kn = 0.05$

(c) $Kn = 1$ (d) $Kn = 10$

Figure 3.12: Vortex structures for $AR = 2.5$, $Mach_{lid} = 3.0$

When the Knudsen number is maintained constant, the number of vortices increase with an increase in the lid velocity. This is more prominent with flows in near-continuum regime and with a high cavity aspect ratio. An interesting observation is that of the large difference in vortex strengths between the vortices which appeared in a particular flow. It is noted that the multi-vortex configuration is stable when secondary or higher level vortices progressively showed a large relative difference in their vortex strengths. However, at high lid velocities, higher order vortices with vortex strengths comparable to the primary vortex start appearing with an increase in the degree rarefaction (Figure 3.12). This phenomena triggers numerical instability (see section 3.3.4) with non-physical oscillations in the flow affecting the rate of convergence. For example, a snapshot of the highly non-equilibrium case can be seen in Figure 3.12 (d). However, when the aspect ratio is reduced for the same case (Figure 3.10 (d)), the geometry combined with the high degree of rarefaction disallows the formation of any secondary eddies henceforth causing the flow to be steady and stable with a single vortex configuration.

Another important factor to be noted from Figure 3.8 is that the temperature peaks on the upper right corner of the cavity, which increases with an increase in the degree of rarefaction. This phenomena can be attributed to the relatively lesser number of inter-molecular collisions (which allows for an exchange in energy transfer to neighbouring molecules) than the number of molecular-surface interactions that occur in a rarefied cavity flow. Further, the direction of heat flux disobeys Fourier's law particularly with an increase in the degree or rarefaction. Wang et al. [44] has derived an empirical model for non-Fourier heat transfer by examining DSMC data of rarefied hypersonic flows. However, a universal model is yet to be formulated. A detailed study with an extended set of simulations is currently under progress.

### 3.3.4 Simulations with Newton-Cotes Quadrature

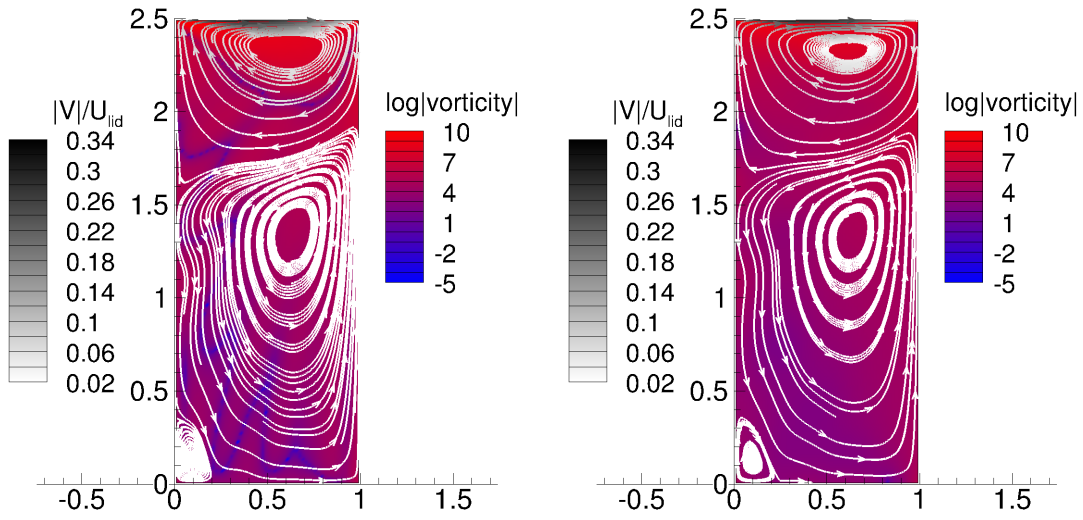


(a) Van-Leer with $100 \times 100$ velocity points (b) WENO-S with $100 \times 100$ velocity points

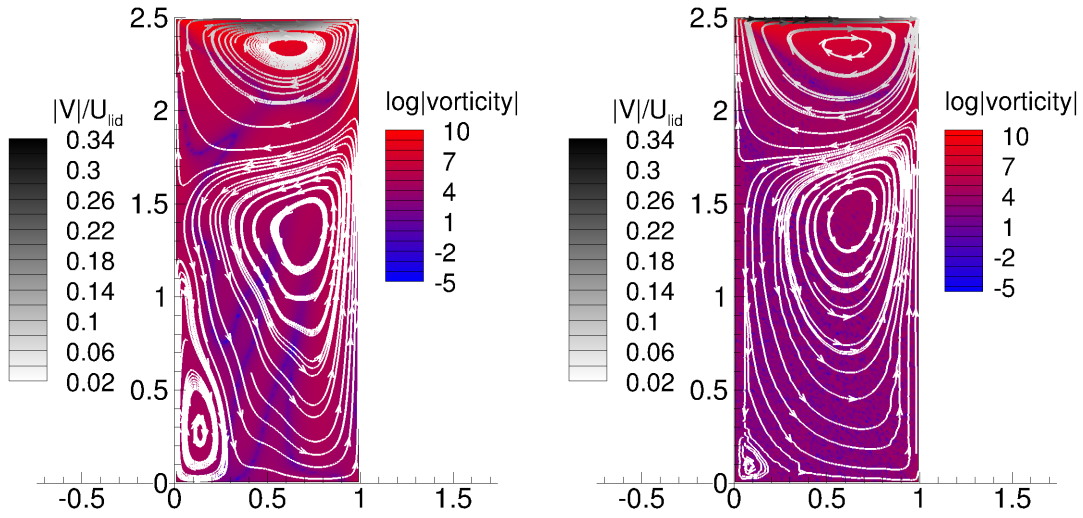


(c) Van-Leer with $100 \times 100$ velocity points (d) DSMC

Figure 3.13: Vortex structures for $AR = 2.5,\ Mach_{lid} = 3.0,\ Kn = 10$

Due to the discretization in the velocity space, UGKS suffers from boundary induced discontinuities at high Knudsen numbers. A typical feature of the cavity flow is that the distribution function can become highly irregular from discontinuities induced around its corners. Significant oscillations are induced by the top two corners of the cavity due to the strong discontinuities in the velocity between stationary and moving walls. The discontinuities from the boundaries propagate inside the computational domain and produce non-physical oscillatory behavior in the macroscopic quantities. The issue is popularly known as 'ray effects' in the transport theory community and appears in neutron transport and radiative transfer [27]. Methodologies have been proposed and successfully implemented to eliminate this problem for low-speed rarefied flows [31, 42]. The 'ray effects', in general, can be partially eliminated by increasing the number of discrete velocities. With such an approach, the amplitude of these oscillations decreases but their frequency increases. Further, the Gauss-Hermite type distribution points are widely spaced in the velocity space. The weights of extreme velocities can be rather small, minimizing their contribution in the process of numerical integration. So, the use of Newton-Cotes quadrature is more promising in rarefied supersonic flows which are in high non-equilibrium state [18].

In this final study, simulations are performed with an increased number of discrete velocity points. Simulations are performed with a $100 \times 100$ Newton-Cotes quadrature for the highly non-equilibrium case of deep cavity with a lid velocity of $Mach$ 3 and $Kn$ 10. UGKS simulations with both Van-Leer and WENO-S interpolations are performed and are compared with a corresponding DSMC simulation. Figure 3.13 shows the vortex structures generated by these computations. Simulation with WENO-S converges much faster than a corresponding Van-Leer case. Figures 3.13(a, b and d) show the converged steady solutions. Figures 3.13(b) and 3.13(b) are con-

verged solutions to the same convergence criteria, but the latter took almost double the number of iterations more to reach a steady-state solution (Figure 3.13(a)). The DSMC solution (Figure 3.13(d)) is oscillation-free and is believed to be the most accurate in this rarefied supersonic regime. It can be seen that both Figures 3.13(a) and 3.13(b) yield similar vortex structures to those by DSMC. However, the non-physical oscillations in streamlines as well as the vorticity contours (Figures 3.12(d) and 3.13(a)) are smoothed out by the WENO-S based UGKS simulation (Figure 3.13(b)).

## 3.4 Conclusion

The results from UGKS codes are validated against corresponding DSMC solutions for a wide range of Knudsen numbers spanning from near-continuum/slip regime to rarefied regime. Use of WENO schemes for initial reconstruction of the distribution fluxes gave oscillation-free solutions with higher spacial accuracy as well as faster convergence compared to Van-Leer limiting scheme at high Knudsen numbers.

Further simulations with varying aspect-ratio reveal that the formation of secondary vortices depend on the degree of rarefaction as well as the lid velocity. It is observed that multi-vortex configurations are favourable in high aspect ratio cavities. As the degree of rarefaction is increased, secondary vortices tend to disappear. At the same time, the number of active vortices increase with an increase in the lid velocity. However, with higher lid velocities at highly rarefied regimes, non-physical oscillations appear in the flow domain. Newton-Cotes quadrature with 100 velocity points in each direction along with a $5^{th}$ WENO scheme for flux interpolation is then necessary to obtain a physically meaningful steady-state with UGKS. Full 3D simulations are needed to further confirm the physical features presented here.

# 4. THERMAL TRANSPORT ANALYSIS IN RAREFIED CAVITY FLOWS

Thermal transport in high-speed rarefied flows far removed from thermodynamic equilibrium is investigated using numerical simulations and extended thermodynamic models. Gas Kinetic numerical simulations of lid-driven cavity flows are performed over a wide range of Knudsen numbers, Mach numbers and cavity shapes. Two numerical schemes − Unified Gas Kinetic Scheme (UGKS) and Direct Simulation Monte Carlo (DSMC) − are employed to simulate transport behavior at different degrees of rarefaction. Thermal transport is then characterized as a function of lid Mach number, cavity aspect-ratio and Knudsen number distribution. Vast deviation from Fourier law thermal flux, including counter−counter−gradient (CCG) transport, is exhibited. Entropy implications are examined in detail. It is demonstrated that extended thermodynamic models can reasonably account for observed behavior. Challenges facing thermal-transport modeling in non-equilibrium flows are identified.

## 4.1 Introduction

Fourier law of heat conduction is one of the foundations of transport theory in the realm of continuum mechanics. The law states that the heat flux is proportional to the magnitude and opposite in direction of the temperature gradient. While Fourier law is widely known to be accurate when the medium can be treated as a continuum, it is also evident that significant departures occur outside the continuum limits. Flow in microscale devices often fall in the rarefied regime as the device size is not substantially larger than the mean free path of the gas. In many high-altitude flight applications, the flow is not only rarefied, but also compressible and in a state to thermodynamic non-equilibrium. (Throughout this work the term *thermodynamic non-equilibrium* indicates a gas whose constituent molecular velocity

distribution function is far from a Maxwellian). Thus, there is much recent interest in understanding thermal transport behavior in rarefied flows and gases that are far from thermodynamic equilibrium.

In this study, we analyze the thermal transport behavior within canonical lid-driven cavity flows exposed to high non-equilibrium conditions. Gas kinetic numerical simulations of cavity flows are performed for a wide range of flow regimes − subsonic incompressible to supersonic speeds, and continuum to rarefied domains. Unified Gas Kinetic Scheme (UGKS) is used to enable the simulations to be done over a wide range of Knudsen numbers (degrees of rarefaction) and flow speeds. Results are verified with Direct Simulation Monte Carlo (DSMC) computations in the case of near-continuum, transition and rarefied flows. Heat transport within the cavity are characterized as a function of lid-speed, cavity aspect-ratio and degree of rarefaction. Heat flux components from extended thermodynamic models such as augmented Burnett and BGK-Burnett models are then examined and compared with corresponding UGKS and DSMC fluxes. The flow fields generated with UGKS are then tested for their compatibility with the second law of thermodynamics through appropriate entropy considerations.

The Navier-Stokes-Fourier (NSF) governing equations fail after a local Knudsen number of about 0.001. Although this can be mathematically proved, the most important cause for this failure is the deviation of transport properties from continuum. The gradients of the macroscopic variables become so steep that their associated length scales tend to the order of the particle mean free path. Extended hydrodynamic equations with higher order terms to compute the transport terms, such as Burnett or super-Burnett corrections, extendeds the applicability of continuum models to higher Knudsen numbers. In this study, where the simulations are frequently exposed to high non-equilibrium conditions, the transport properties are computed

directly from the moments of particle velocity distribution function (vdf). The mathematical model that governs the evolution of vdf in its phase space then becomes the Boltzmann equation which is valid in the entire Knudsen number regime. Numerical schemes based on the Boltzmann model is used for the simulations presented in this work and are explained in detail in Chapter 2 and Appendix A.

The objective of this work is to analyze and understand the non-equilibrium thermal transport behavior in a cavity flow as a function of cavity aspect ratio, lid speed and rarefaction parameter. A lot of fundamental physics in fluid dynamics has been explored, both experimentally as well as numerically, for lid-driven cavity flows. The effect of rarefaction on thermal transport was also observed in the field of solid mechanics when the device characteristic length is comparable to the heat-carrier mean free path, or when the characteristic time is in the order of heat-carrier relaxation time. It was later discovered that a ballistic transport mechanism is present near the system boundaries that can cause significant deviations in corresponding local thermal behavior [14]. The problem is then approached by assuming the coexistence of two kinds of heat carriers (phonons): diffusive phonons that undergo multiple collisions within the core of the system and ballistic phonons originating at the system boundaries and experiencing collisions mainly with the walls. Hence, the total thermal flux is decomposed into ballistic and the diffusive components which are then governed by separate model equations which is known as the ballistic-diffusion model [14, 25]. However, their approach is restricted to the linear domain as all nonlinear contributions are omitted. In addition, coupling between diffusive and ballistic heat fluxes has been neglected. Near-continuum and quasi-equilibrium rarefied flows have been numerically simulated with different extended higher-order hydrodynamic models, such as the Burnett, BGK (Bhatnagar-Gross-Krook)-Burnett, augmented Burnett, regularized Burnett and super-Burnett equations [52, 21, 2, 1]. These mod-

els are able to accurately capture the macroscopic properties and significant features pertaining to rarefied effects such as the non-linear pressure drop in microchannel flows [34, 26]. However, the evolution of model transport properties and their reliability over the entire range of Knudsen numbers and flow speeds are yet to be investigated. The investigation presented in this article is divided into two parts. The first study focuses on establishing the validity and applicability of the most common models that are used to predict the thermal transport behaviour: Fourier, augmented Burnett and BGK-Burnett. In the second part, the evolution of flow fields are subject to a compatibility test against the second law of thermodynamics to ensure the physical existence of our numerical results.

Toward these above mentioned objectives, we perform two-dimensional (2D) as well as three-dimensional (3D) gas kinetic numerical simulations (GKNS) of lid-driven cavity flows over a range of parameters being the lid Mach number, global Knudsen number and cavity aspect ratio. The thermal flux components obtained from GKNS simulations are first verified for their correctness. Conductive heat fluxes of GKNS are then compared with the heat fluxes computed from Fourier, augmented Burnett and BGK-Burnett models to establish the range of applicability of these models. A final compatibility test of the Unified Gas Kinetic Scheme against the second law of thermodynamics is then conducted. We seek an appropriate entropy criterion that incorporates the possible effects in a non-equilibrium flow and then examine the consistency of our numerical results with the chosen entropy evolution model, establishing further validity of the numerical scheme.

## 4.2 Heat Flux Analysis

The constitutive relation between the heat flux components and the state properties can be derived from approximate solutions to the Boltzmann equation using

the Chapman-Enskog expansion. The heat flux vector then follows as:

$$q_i = q_i^{(0)} + q_i^{(1)} + q_i^{(2)} + q_i^{(3)} + ... + O(\lambda^{(n)}) \tag{4.1}$$

The mean free path $\lambda$ for variable hard sphere molecules is given by

$$\lambda = \frac{16\mu}{5\rho\sqrt{2\pi RT}} \tag{4.2}$$

where $\mu$,$R$ and $T$ represent the dynamic viscosity, gas constant and temperature respectively. Viscosity dependence on temperature is facilitated by invoking Sutherland's law

$$\frac{T}{T_{ref}} = \left(\frac{\mu}{\mu_{ref}}\right)^{\omega} \tag{4.3}$$

Here, $\omega$ is the viscosity index and $\mu_{ref}$ is the viscosity at a reference temperature $T_{ref}$

In the continuum near-equilibrium state, the second and higher order terms in Equation 4.1 are present, but their effects on the final heat flux are negated due to infinitesimal mean free path ($\lambda$) of the molecules constituting a continuum media. Also, it is well-known that a zeroth order approximation (when $n = 0$) corresponds to the Euler equations and hence $q_i^{(0)} = 0$. The first order approximation eventually represents the Navier-Stokes equations and the first two terms in Equation 4.1 become important in the accurate computation of continum heat flux. The first order heat flux components in a 2D flow can be expressed as:

$$q_x^{(1)} = -\kappa T_x, \quad q_y^{(2)} = -\kappa T_y \tag{4.4}$$

where $()_x = \frac{\partial()}{\partial x}$, $()_y = \frac{\partial()}{\partial y}$ and $\kappa$ is the coefficient of thermal conductivity.

As we move on to transitional regimes (in terms of rarefaction), additional higher order terms in Equation 4.1 are required to compute the heat flux components with reasonable accuracy. Numerous forms for these higher order terms have been derived in the literature. Non-continuum fluid flows have frequently been approached with different extended higher-order hydrodynamic models, such as the Burnett, BGK(Bhatnagar-Gross-Krook)-Burnett, augmented Burnett, regularized Burnett and super-Burnett equations [52, 21, 2, 1]. These models are able to accurately capture the macroscopic properties and other significant features pertaining to rarefied effects. General expressions for the second order Burnett equations were first derived by Burnett [10], and later corrected by Chang and Uhlenbeck [12] and then completely formulated by Chapman and Cowling [13]. The stability analysis of the Burnett equations, which was first carried out by Bobylev [8], shows that these equations were unstable to disturbances of very small wavelengths. Zhong [52] chose, by trial and error, to add all the linear third derivative terms from the super Burnett equations to the stress and heat flux relations of the conventional Burnett equations. It was also shown by the method of linearized stability analysis that the resulting 'augmented Burnett equations' are stable to these disturbances. However, attempts at computing the flow fields for blunt body wakes and flat plate boundary layers even with the augmented Burnett equations have not been entirely successful. It has been conjectured by Comeaux et al. [17] that this instability may be due to the fact that the augmented Burnett equations violate the second law of thermodynamics at higher Knudsen numbers. A new set of equations, designated as the 'BGK-Burnett' equations was then derived by Balakrishnan and Agarwal [3]. It was shown by the authors that the BGK-Burnett equations are stable to small wavelength disturbances and that they yield results consistent with the second law of thermodynamics. Jin and Slemrod [21] introduced a regularization method for the Burnett equations,

which is based on Grad's 13-moment method and the requirement of a positive entropy generation. However, unknown coefficients appear in their set of equations which were obtained by fitting to experimental data. Torrilhon and Struchtrup [40] clearly illustrates that these regularized Burnett equations do not account for major terms contributing to non-equilibrium effects, which is one of the reasons why the addition of super-Burnett terms pose formidable issues.

In this work, we compute the higher order heat flux components based on the augmented Burnett as well as the BGK-Burnett equations [2, 1, 51]. For convenience, augmented Burnett and BGK-Burnett heat fluxes are designated as $q_i^{(AB)}$ and $q_i^{(BGKB)}$ respectively. The augmented Burnett heat flux components for a 2D flow are given as:

$$\begin{aligned} q_x^{(AB)} &= q_x^{(0)} + q_x^{(1)} + \frac{\mu^2}{\rho}\Bigg(\gamma_1\frac{1}{T}T_x u_x + \gamma_2\frac{1}{T}T_x v_y + \gamma_3 u_{xx} + \gamma_4 u_{yy} + \gamma_5 v_{xy} + \gamma_6\frac{1}{T}T_y v_x \\ &+ \gamma_7\frac{1}{T}T_y u_y + \gamma_8\frac{1}{\rho}\rho_x u_x + \gamma_9\frac{1}{\rho}\rho_x v_y + \gamma_{10}\frac{1}{\rho}\rho_y u_y + \gamma_{11}\frac{1}{\rho}\rho_y v_x\Bigg) \\ &+ \frac{\mu^3 R}{p\rho}\left(\gamma_{12}T_{xxx} + \gamma_{12}T_{xyy} + \gamma_{13}\frac{T}{\rho}\rho_{xxx} + \gamma_{13}\frac{T}{\rho}\rho_{xyy}\right) \end{aligned} \tag{4.5}$$

$$\begin{aligned} q_y^{(AB)} &= q_y^{(0)} + q_y^{(1)} + \frac{\mu^2}{\rho}\Bigg(\gamma_1\frac{1}{T}T_y u_y + \gamma_2\frac{1}{T}T_y v_x + \gamma_3 v_{yy} + \gamma_4 v_{xx} + \gamma_5 u_{xy} + \gamma_6\frac{1}{T}T_x u_y \\ &+ \gamma_7\frac{1}{T}T_x v_x + \gamma_8\frac{1}{\rho}\rho_y v_y + \gamma_9\frac{1}{\rho}\rho_y u_x + \gamma_{10}\frac{1}{\rho}\rho_x v_x + \gamma_{11}\frac{1}{\rho}\rho_x u_y\Bigg) \\ &+ \frac{\mu^3 R}{p\rho}\left(\gamma_{12}T_{yyy} + \gamma_{12}T_{xxy} + \gamma_{13}\frac{T}{\rho}\rho_{yyy} + \gamma_{13}\frac{T}{\rho}\rho_{xxy}\right) \end{aligned} \tag{4.6}$$

On the other hand, the BGK-Burnett heat flux components are computed as:

$$
\begin{aligned}
q_x^{(BGKB)} &= q_x^{(0)} + q_x^{(1)} + \frac{\mu^2}{\rho}\Bigg(\gamma_1\frac{1}{T}T_x u_x + \gamma_2\frac{1}{T}T_x v_y + \gamma_3 u_{xx} + \gamma_4 u_{yy} + \gamma_5 v_{xy} + \gamma_6\frac{1}{T}T_y v_x \\
&+ \gamma_7\frac{1}{T}T_y u_y + \gamma_8\frac{1}{\rho}\rho_x u_x + \gamma_9\frac{1}{\rho}\rho_x v_y + \gamma_{10}\frac{1}{\rho}\rho_y u_y + \gamma_{11}\frac{1}{\rho}\rho_y v_x\Bigg) \\
&+ \frac{\mu^3}{p\rho}\Bigg(R\theta_1(T_{xxx} + T_{xyy} - \frac{1}{\rho}\rho_x T_{xx} - \frac{1}{\rho}\rho_x T_{yy}) + \theta_2 u_x u_{xx} + \theta_3 u_x v_{xy} + \theta_4 u_x u_{yy} \\
&+ \theta_5 v_y u_{xx} + \theta_6 v_y v_{xy} + \theta_7 v_y u_{yy} + \theta_8 u_y v_{xx} + \theta_9 u_y u_{xy} + \theta_4 u_y v_{yy} + \theta_8 v_x v_{xx} \\
&+ \theta_9 v_x u_{xy} + \theta_4 v_x v_{yy} - \left(\frac{\rho_x}{\rho} + \frac{T_x}{T}\right)(\theta_{10}u_x^2 + 2\theta_{11}u_x v_y + 2\theta_{12}u_y v_x + \theta_{12}u_y^2 \\
&+ \theta_{12}v_x^2 + \theta_{10}v_y^2) + \frac{R\theta_1}{T}(T_x T_{xx} + T_x T_{yy})\Bigg) \qquad (4.7)
\end{aligned}
$$

$$
\begin{aligned}
q_y^{(BGKB)} &= q_y^{(0)} + q_y^{(1)} + \frac{\mu^2}{\rho}\Bigg(\gamma_1\frac{1}{T}T_y u_y + \gamma_2\frac{1}{T}T_y v_x + \gamma_3 v_{yy} + \gamma_4 v_{xx} + \gamma_5 u_{xy} + \gamma_6\frac{1}{T}T_x u_y \\
&+ \gamma_7\frac{1}{T}T_x v_x + \gamma_8\frac{1}{\rho}\rho_y v_y + \gamma_9\frac{1}{\rho}\rho_y u_x + \gamma_{10}\frac{1}{\rho}\rho_x v_x + \gamma_{11}\frac{1}{\rho}\rho_x u_y\Bigg) \\
&+ \frac{\mu^3}{p\rho}\Bigg(R\theta_1(T_{yyy} + T_{xxy} - \frac{1}{\rho}\rho_y T_{yy} - \frac{1}{\rho}\rho_y T_{xx}) + \theta_2 v_y v_{yy} + \theta_3 v_y u_{xy} + \theta_4 v_y v_{xx} \\
&+ \theta_5 u_x v_{yy} + \theta_6 u_x u_{xy} + \theta_7 u_x v_{xx} + \theta_8 v_x u_{yy} + \theta_9 v_x v_{xy} + \theta_4 v_x u_{xx} + \theta_8 u_y u_{yy} \\
&+ \theta_9 u_y v_{xy} + \theta_4 u_y u_{xx} - \left(\frac{\rho_y}{\rho} + \frac{T_y}{T}\right)(\theta_{10}u_x^2 + 2\theta_{11}u_x v_y + 2\theta_{12}u_y v_x + \theta_{12}u_y^2 \\
&+ \theta_{12}v_x^2 + \theta_{10}v_y^2) + \frac{R\theta_1}{T}(T_y T_{xx} + T_y T_{yy})\Bigg) \qquad (4.8)
\end{aligned}
$$

The coefficients for Argon gas [1] from $\gamma_1$ through $\gamma_{14}$ are $-11.101$, $-1.0$, $-1.384$, $-2.0$, $-3.333$, $-6.5$, $-5.667$, $-1.051$, $1.0$, $-3.0$, $-3.0$, $0.6875$ and $-0.625$ respectively; and from $\theta_1$ through $\theta_{12}$ are $4.167$, $6.222$, $-1.778$, $1.333$, $-3.111$, $4.222$, $-0.667$, $4.333$, $3.667$, $2.222$, $-1.111$ and $1.667$ respectively.

## 4.3 Second Law of Thermodynamics from a Microscopic Perspective

Second law of thermodynamics can give useful information about the direction of thermodynamic processes within a system. It is well-known that any thermodynamic process are directed towards increasing entropy. In continuum, the entropy field in the cavity is calculated using the famous Sackur-Tetrode equation (Equation 4.9) for the absolute translational entropy.

$$S_{tr} = nk\left[\frac{5}{2}R\log T - R\log P + R\left\{\log\left[\left(\frac{2\pi m}{h^2}\right)^{\frac{3}{2}} k^{\frac{5}{2}}\right] + \frac{5}{2}\right\}\right] \tag{4.9}$$

Here, $n$ is the number density (number of molecules per unit volume), $k$ is the Boltzmann's constant, $h$ is the Planck's constant and $m$ is the molecular mass. This entropy function was derived purely from quantum considerations for monatomic ideal gases and assumes that the region of interest is in local thermodynamic equilibrium. It is also required to quantify entropy in the non-continuum regimes in our case. By definition, entropy is a measure of the degree of randomness or disorder. In a molecular point of view, this quantity can be directly related to the changes in the velocity distribution function, which is the essence of the famous Boltzmann's $H$ theorem. Over a small time interval, $f$ changes to $f + \Delta f$ and the fractional change is $\Delta f/f$ or $\Delta(lnf)$. In an ensemble of simple dilute monatomic gas that is free of any external force, Boltzmann's $H$ function is the mean value of $ln(nf)$.

$$H = \overline{ln(nf)} = \int_{-\infty}^{\infty} f ln(nf) d\mathbf{c} \tag{4.10}$$

Boltzmann's $H$ theorem states that for any initial distribution of molecules in the velocity space, the distribution will alter with time in such a way that $H$ decreases

monotonically,

$$\frac{\partial H}{\partial t} < 0 \tag{4.11}$$

and at subsequent times,

$$\frac{\partial H}{\partial t} = 0. \tag{4.12}$$

It can be shown that $H$ converges to a value proportional to $S_{tr}$ at thermodynamic equilibrium

$$H(f_M) = \int_{-\infty}^{\infty} f_M ln(n f_M) d\mathbf{c} = -\frac{S_{tr}}{R} + c \tag{4.13}$$

where $f_M$ is the Maxwellian equilibrium distribution. Second law compatibility tests with the above mentioned entropy criteria will be discussed in §4.7.

## 4.4 Simulation Parameters

Temperature fields and heat flux streamlines for lid-driven cavity flows are generated using UGKS based simulations. A DSMC method will not allow the simulation for continuum or near-continuum cases due to the requirement of enormous computational resources. However, it is easily possible to conduct simulations of rarefied flows using DSMC even for a 3D case. On the other hand, a 3D UGKS simulation is almost impossible due to memory constraints as the whole phase space will have to be meshed. Hence, 2D lid-driven cavity flows are simulated using UGKS. Through proper verification with DSMC simulations, it will be shown in §4.5.1 and §4.5.2 that 2D UGKS simulations could capture relevant flow physics that are subject to current analyses. Four sets of numerical experiments are performed to span the entire range of global Knudsen numbers (Table 4.1). The lid Mach number ($M_{lid}$) is chosen such that the flows can be classified into incompressible subsonic ($M_{lid} = 0.1$), compressible subsonic ($M_{lid} = 0.5$) and supersonic ($M_{lid} = 3.0$) regions. Here, the global Knudsen number ($Kn_g$) is defined as the ratio of freestream particle mean free path

($\lambda_{VHS}$) based on a Variable Hard Sphere (VHS) collision model to the characteristic length scale of the cavity ($L$) which is set to one meter (equation 4.14).

| Case | $Kn_g$ | $M_{lid}$ | $AR$ |
|---|---|---|---|
| Continuum | 0.001 | 0.1, 0.5, 3.0 | 1.0, 2.0, 0.5 |
| Near-continuum | 0.01 | 0.1, 0.5, 3.0 | 1.0, 2.0, 0.5 |
| Transition | 0.1 | 0.1, 0.5, 3.0 | 1.0, 2.0, 0.5 |
| Rarefied | 2.0 | 0.1, 0.5, 3.0 | 1.0, 2.0, 0.5 |

Table 4.1: Simulation parameters

$$Kn_g = \frac{\lambda_{VHS}}{L} \tag{4.14}$$

$$\lambda_{VHS} = \frac{16\mu_{ref}}{5\rho ref\sqrt{2\pi RT_{ref}}} = \frac{1}{\sqrt{2}\pi d_{ref}^2 n_{ref}} \tag{4.15}$$

The subscript $ref$ denotes freestream/reference state. $d$ and $n$ are the molecular diameter and number density (number of molecules per unit volume) respectively. For the verification study, simulations are performed with Argon gas (Table 4.2) as the working fluid.

| | |
|---|---|
| Molecular mass, $m$ | $66.3 \times 10^{-27}\ kg$ |
| Molecular diameter, $d$ | $4.17 \times 10^{-10}\ m$ |
| Viscosity coefficient, $\mu$ | $2.117 \times 10^{-5}\ Nsm^{-2}$ |
| Viscosity index, $\omega$ | 0.81 |
| Prandtl number, $Pr$ | 0.67 |

Table 4.2: Properties of Argon gas at reference state (101325 $Pa$ and $273K$)

For the analysis part, all molecular dimensions are same as that of Argon gas except the Prandtl number being toggled to one. Though a change in Prandtl number did not give significant variations in UGKS results, a unit Prandtl number was necessary as the augmented Burnett and the BGK-Burnett model coefficients did not take non-unit Prandtl number effects under consideration. Simulations are also categorized based on the cavity aspect ratio ($AR$) which is defined as the ratio of cavity width to cavity height. The geometrical dimensions for different cavity sizes are included in Figure 4.1.

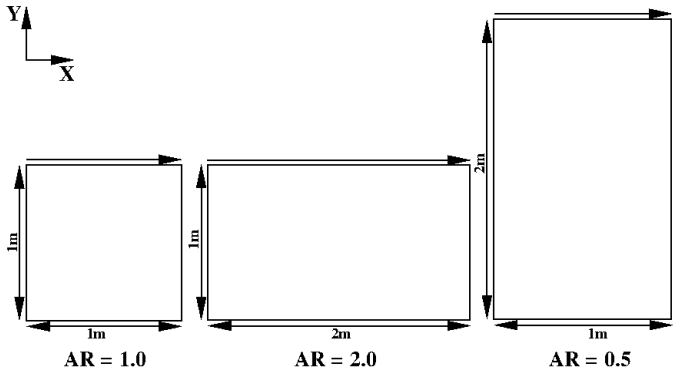


Figure 4.1: Cavity dimensions for different sizes

All the cavity walls including the lid are kept isothermal at a temperature of $273K$ and are modelled with a no penetration boundary condition (see Appendix A). The cavity domain is meshed with a uniform structured grid with a 2D cell size of $0.01m \times 0.01m$ which was determined after a grid independence study with a CFL number of 0.6.

## 4.5 Verification

2D UGKS results of cavity flow simulations are verified against corresponding 2D/3D DSMC simulation results.

### *4.5.1 3D DSMC versus 2D DSMC*

3D DSMC computations are performed using the open source code dsmcFOAM for cubic cavity ($AR = 1$) with a protrusion of $1m$ in the third direction. The end planes in the third direction are assigned periodic boundary condition and all other walls including the lid are kept at a constant temperature of $273K$. A Maxwellian diffuse reflection model was selected for modelling the gas-surface interaction with the solid walls. The 3D sampling cell size is now $0.01m \times 0.01m \times 0.01m$. The number of collision sub cells are automatically generated by dsmcFOAM based on the freestream number density and the factor $F_{num}$ holding the number of molecules represented by a simulated particle. $F_{num}$ is set such that there are 20 simulated particles on an average per sampling cell. DSMC time-step was set to be one-third of the mean collision time in the reference state $\tau_{ref}$ given by Equation 4.16

$$\tau_{ref} = \frac{1}{\pi d_{ref}^2 n_{ref} \bar{c}_{r,ref}} \tag{4.16}$$

where $\bar{c}_{r,ref} = \left(\frac{16kT_{ref}}{\pi m}\right)^{1/2}$ is the mean magnitude of the relative velocity of colliding molecules in the reference state. The simulations are done only for rarefied cases

since 3D DSMC computations are expensive in the continuum limit. The global Knudsen number for 3D simulations are chosen to be 0.5 and 4.0 with lid Mach numbers of 0.5 and 1.0. The temperature profiles and heat flux components are compared with corresponding 2D DSMC simulations and are shown in Figure 4.2. It can be seen that the peak temperature is always at the top right corner in all cases which is predicted well even with a 2D DSMC model. The steady-state temperature contours and heat flux components within the cavity for both 3D and 2D DSMC computations match well with each other. However, the isotherms are not smooth in the case of any 3D simulations which could be attributed to probable deviations due to statistical averaging in a 3D domain. It should be noted that there are only 20 DSMC simulated particles per cell on an average in the D case which also leads to significant statistical fluctuations. The velocity profiles of 2D DSMC cases have already been verified with the corresponding 3D cases in Venugopal and Girimaji [43].

### *4.5.2 2D DSMC versus 2D UGKS*

Corresponding 2D UGKS simulations are also performed to verify their results against DSMC data. The temperature contours overlaid by streamlines of heat-flux are illustrated in Figure 4.3. It can be seen that the heat flux streamlines and the temperature contours produced by a 2D UGKS simulation agree well with its 2D DSMC counterpart. The streamlines are colored with the cosine of angle between the negative temperature gradient ($-\nabla T$) and the heat flux vector ($\mathbf{q}$). A value of 'one' (red color in Figure 4.3) for this measure then means that the heat flux lines are in the direction of decreasing temperature which is in conformance with the Fourier model. Any other value for this measure would mean that the Fourier law is violated in the respective regions. It can be concluded from Figure 4.3 that the heat

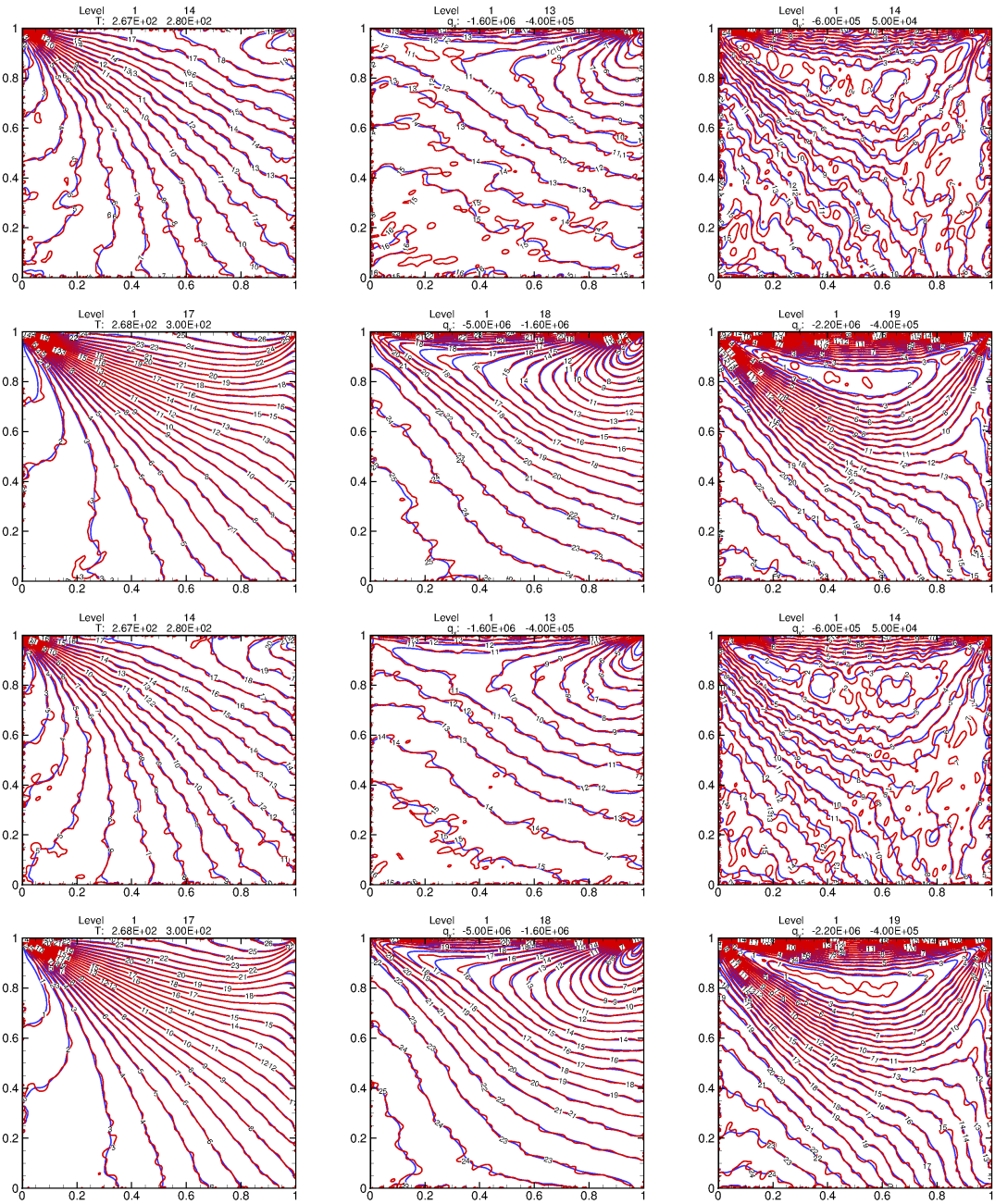


Figure 4.2: 2D DSMC (blue) versus 3D DSMC (red) ([$Kn_g$, $M_{lid}$] for row 1: [0.5, 0.5], row 2: [0.5, 1.0], row 3: [4.0, 0.5], row 4: [4.0, 1.0] and column 1: isotherms, column 2: constant $q_x$ lines, column 3: constant $q_y$ lines)

flux lines violates Fourier model, and is more prominent in the highly rarefied case ($Kn_g = 4.0$), where the flux lines are directed towards hotter regions in the cavity. The purpose here is to simply illustrate that the heat flux direction is well predicted by a 2D UGKS simulation and is verified against a more established DSMC model. A preliminary verification was important to safely proceed with further analysis that are solely dependent on results from 2D UGKS simulations. The non-equilibrium thermal transport behavior is discussed in detail in §4.6.

## 4.6 Analysis on Thermal Transport Mechanisms

Thermal profiles are analysed in the continuum, near-continuum, transition and rarefied cavity flows whose typical global Knudsen numbers are 0.001, 0.01, 0.1 and 2 respectively. In this part, heat flux vectors are calculated from 2D UGKS simulations and are compared against the heat flux vectors computed using Fourier, Burnett and BGK-Burnett models. The measure of deviation of these model fluxes from UGKS fluxes is chosen to be the cosine of the angle between corresponding flux vectors. For example, $cos(Q_{UGKS}, Q_{AB})$ would be the deviation measure of augmented Burnett heat flux ($Q_{AB}$) to UGKS heat flux ($Q_{UGKS}$). The deviations in flux magnitudes were observed to be similar to the chosen deviation measure. These deviations are characterized as a function of global Knudsen number, lid Mach number and cavity aspect ratio in Figures 4.4 through 4.15. All these sets of figures show temperature contours overlaid by the heat-flux streamlines of the corresponding cases. The heat-flux streamlines are colored with the deviation measure. In addition, in any set of figures (from 4.4 to 4.15), the deviation measures are $cos(Q_{UGKS}, Q_{AB})$, $cos(Q_{UGKS}, Q_{AB})$ and $cos(Q_{UGKS}, Q_{AB})$ on columns 1, 2 and 3 respectively. A value of $+1$ (red) for this measure would then mean that the modeled flux is in agreement with the corresponding UGKS flux. On the other hand, a value of $-1$ represent the maximum

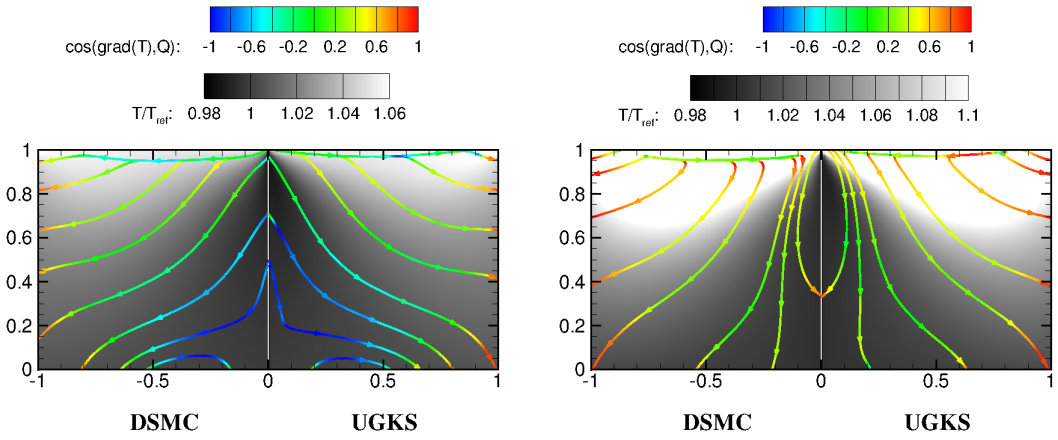


(a) $[Kn_g,\ M_{lid}] = [0.5,\ 0.5]$




(b) $[Kn_g,\ M_{lid}] = [0.5,\ 1.0]$

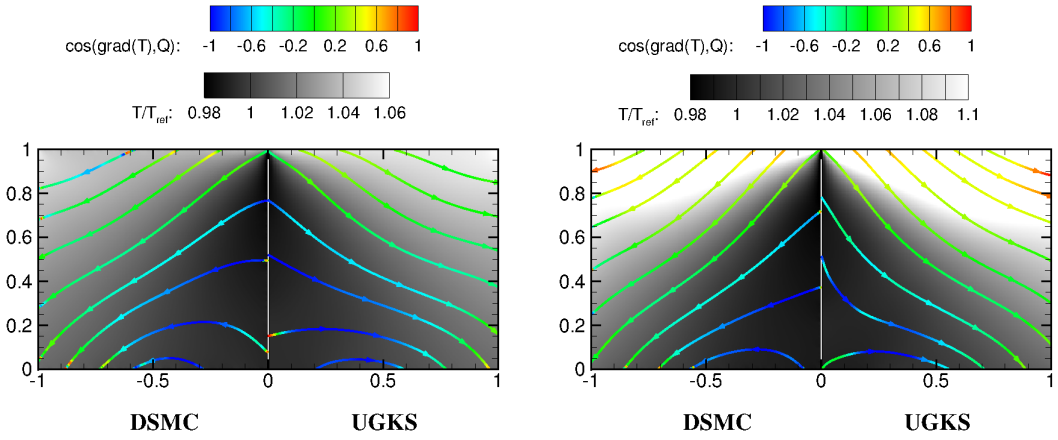


(c) $[Kn_g,\ M_{lid}] = [4.0,\ 0.5]$




(d) $[Kn_g,\ M_{lid}] = [4.0,\ 1.0]$

Figure 4.3: DSMC versus UGKS (mirror symmetric with respect to $x = 0$ plane): Temperature contours overlaid with heat flux streamlines colored with $cos(-\nabla T, Q)$

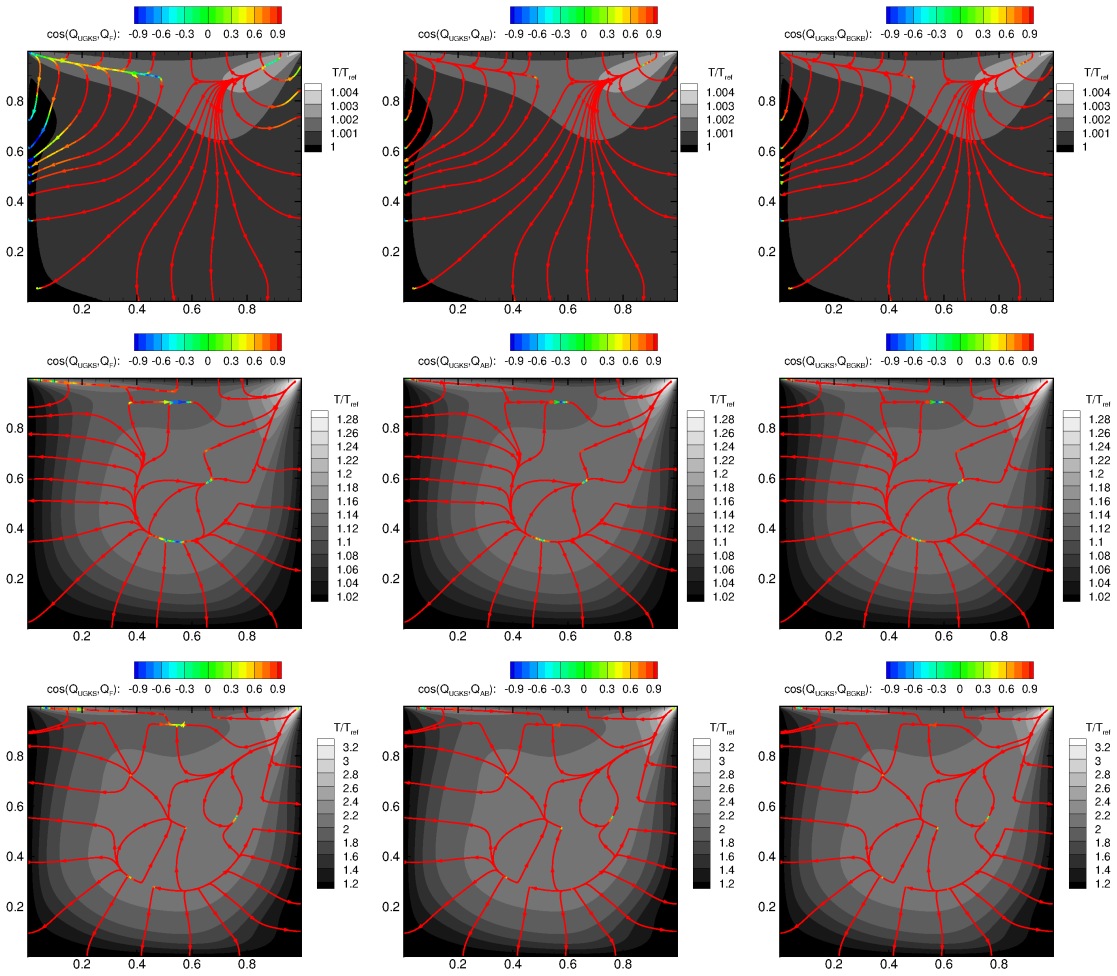


Figure 4.4: Alignment of Fourier, augmented Burnett and BGK-Burnett heat flux with UGKS flux for cavity with $AR = 1.0$ at $Kn_g = 0.001$ and $M_{lid} = 0.1$ (row 1), $M_{lid} = 0.5$ (row 2), $M_{lid} = 3.0$ (row 3); Temperature contours overlaid with heat flux streamlines colored by $cos(Q_{UGKS}, Q_F)$ (column 1), $cos(Q_{UGKS}, Q_{AB})$ (column 2), $cos(Q_{UGKS}, Q_{BGKB})$ (column 3)

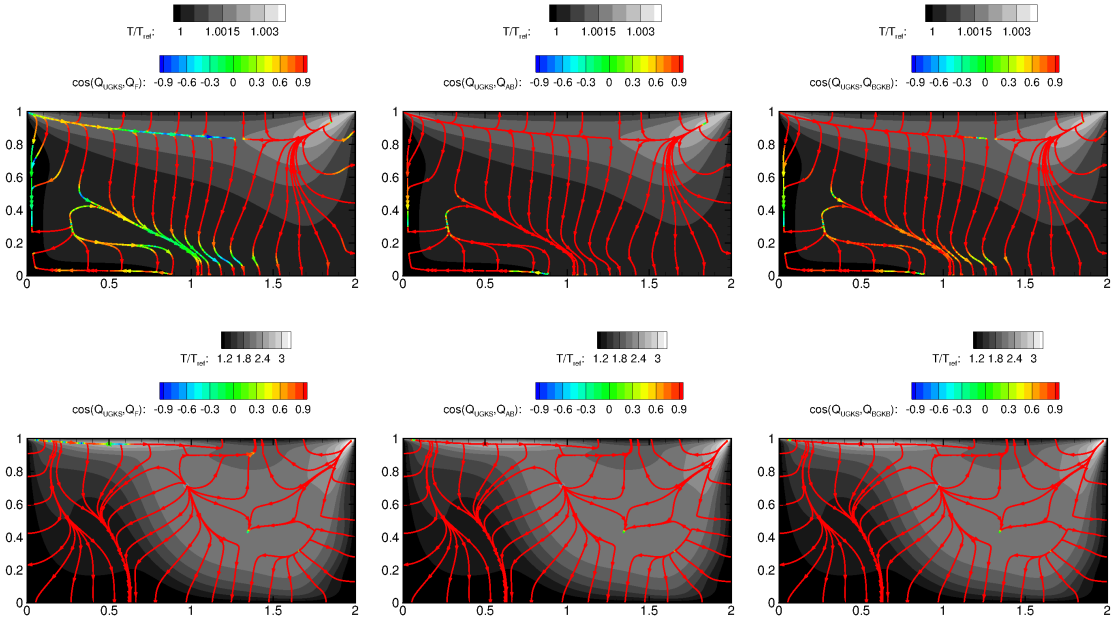


Figure 4.5: Alignment of Fourier, augmented Burnett and BGK-Burnett heat flux with UGKS flux for cavity with $AR = 2.0$ at $Kn_g = 0.001$ and $M_{lid} = 0.1$ (row 1), $M_{lid} = 3.0$ (row 2); Temperature contours overlaid with heat flux streamlines colored by $cos(Q_{UGKS}, Q_F)$ (column 1), $cos(Q_{UGKS}, Q_{AB})$ (column 2), $cos(Q_{UGKS}, Q_{BGKB})$ (column 3)

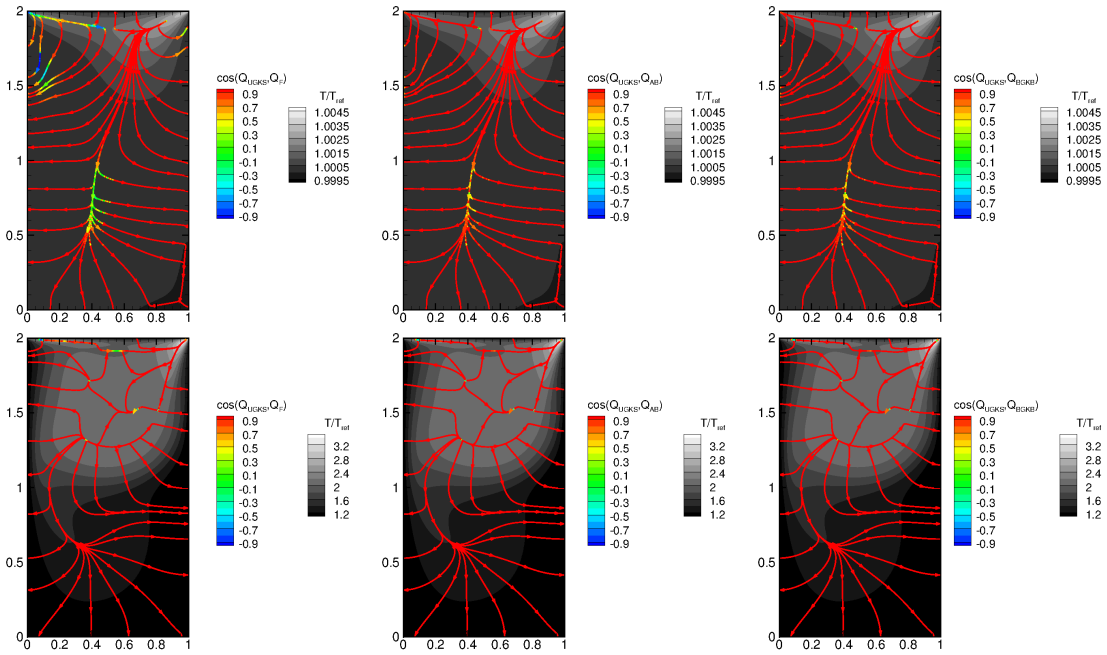


Figure 4.6: Alignment of Fourier, augmented Burnett and BGK-Burnett heat flux with UGKS flux for cavity with $AR = 0.5$ at $Kn_g = 0.001$ and $M_{lid} = 0.1$ (row 1), $M_{lid} = 3.0$ (row 2); Temperature contours overlaid with heat flux streamlines colored by $cos(Q_{UGKS}, Q_F)$ (column 1), $cos(Q_{UGKS}, Q_{AB})$ (column 2), $cos(Q_{UGKS}, Q_{BGKB})$ (column 3)

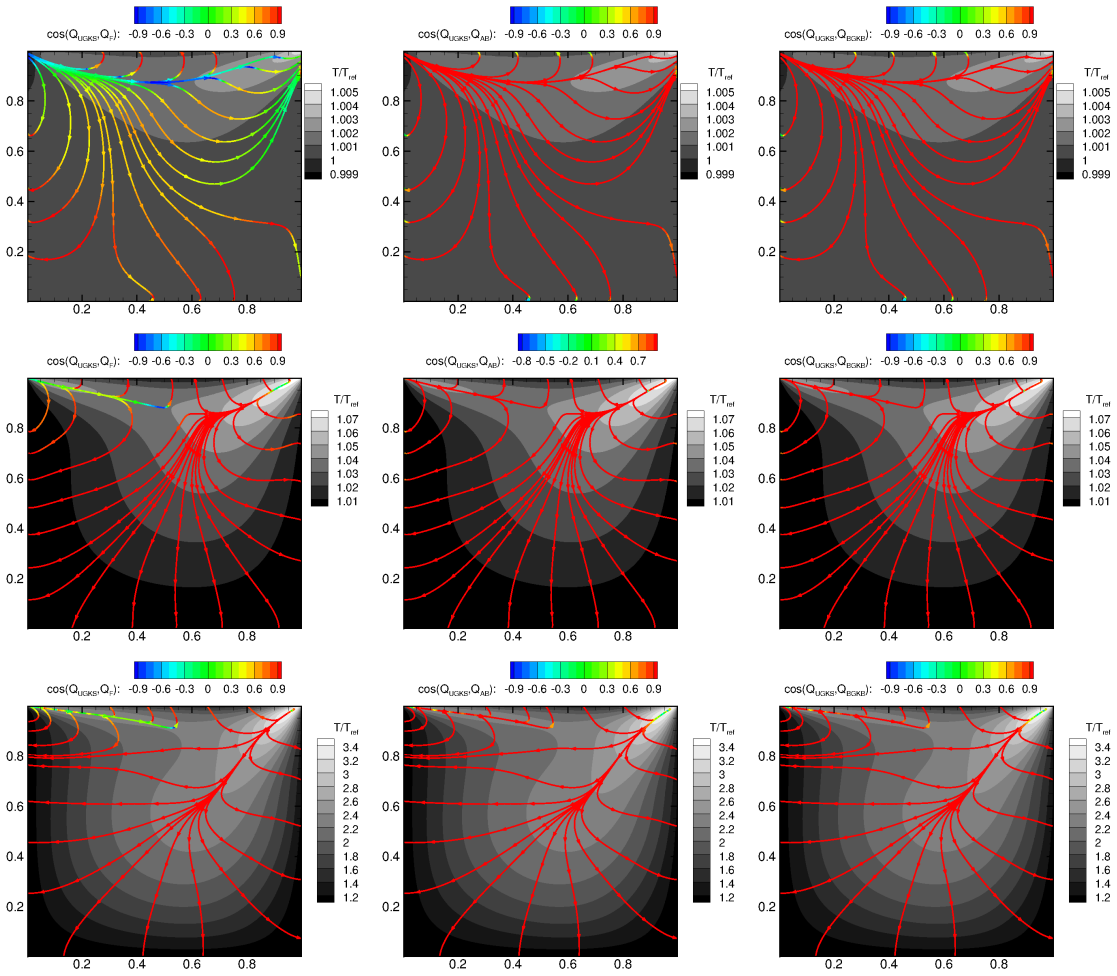


Figure 4.7: Alignment of Fourier, augmented Burnett and BGK-Burnett heat flux with UGKS flux for cavity with $AR = 1.0$ at $Kn_g = 0.01$ and $M_{lid} = 0.1$ (row 1), $M_{lid} = 0.5$ (row 2), $M_{lid} = 3.0$ (row 3); Temperature contours overlaid with heat flux streamlines colored by $cos(Q_{UGKS}, Q_F)$ (column 1), $cos(Q_{UGKS}, Q_{AB})$ (column 2), $cos(Q_{UGKS}, Q_{BGKB})$ (column 3)

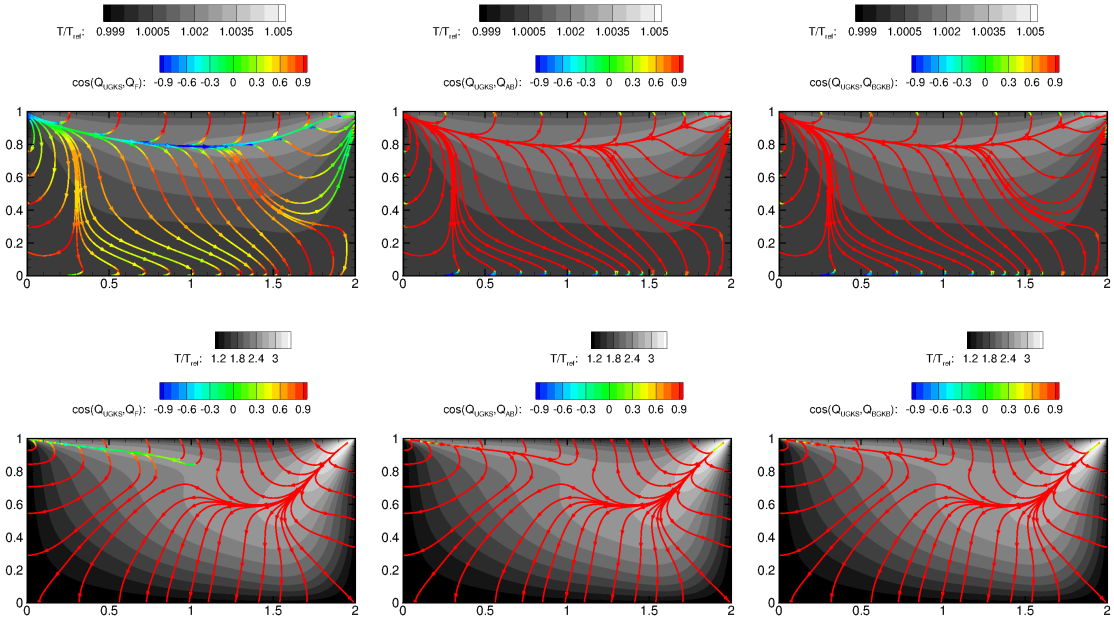


Figure 4.8: Alignment of Fourier, augmented Burnett and BGK-Burnett heat flux with UGKS flux for cavity with $AR = 2.0$ at $Kn_g = 0.01$ and $M_{lid} = 0.1$ (row 1), $M_{lid} = 3.0$ (row 2); Temperature contours overlaid with heat flux streamlines colored by $cos(Q_{UGKS}, Q_F)$ (column 1), $cos(Q_{UGKS}, Q_{AB})$ (column 2), $cos(Q_{UGKS}, Q_{BGKB})$ (column 3)

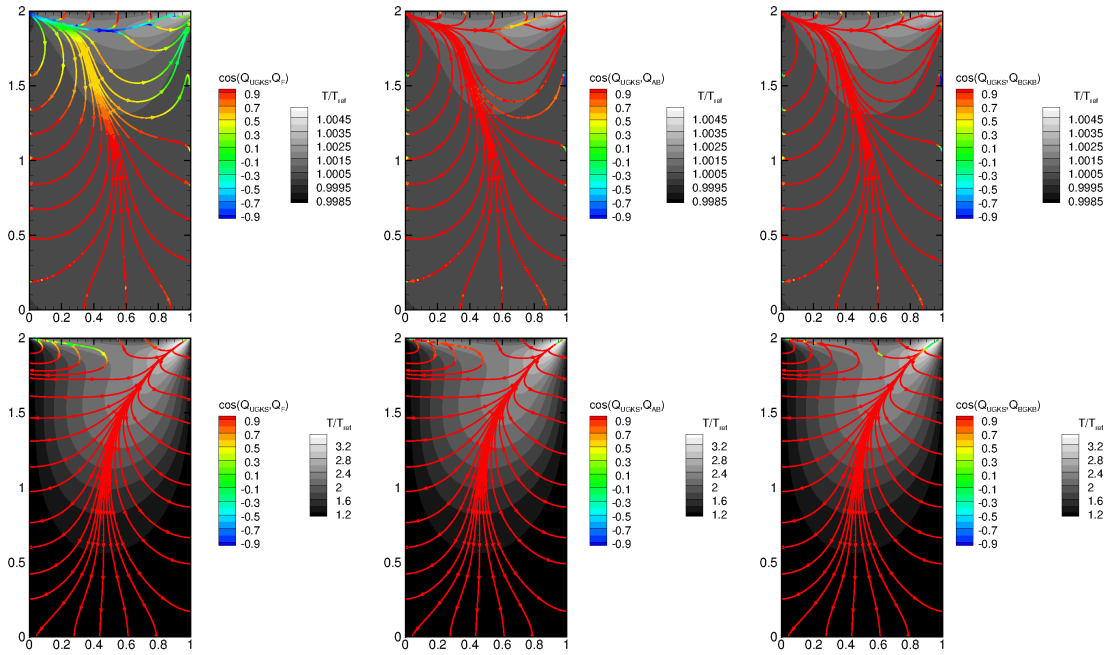


Figure 4.9: Alignment of Fourier, augmented Burnett and BGK-Burnett heat flux with UGKS flux for cavity with $AR = 0.5$ at $Kn_g = 0.01$ and $M_{lid} = 0.1$ (row 1), $M_{lid} = 3.0$ (row 2); Temperature contours overlaid with heat flux streamlines colored by $cos(Q_{UGKS}, Q_F)$ (column 1), $cos(Q_{UGKS}, Q_{AB})$ (column 2), $cos(Q_{UGKS}, Q_{BGKB})$ (column 3)

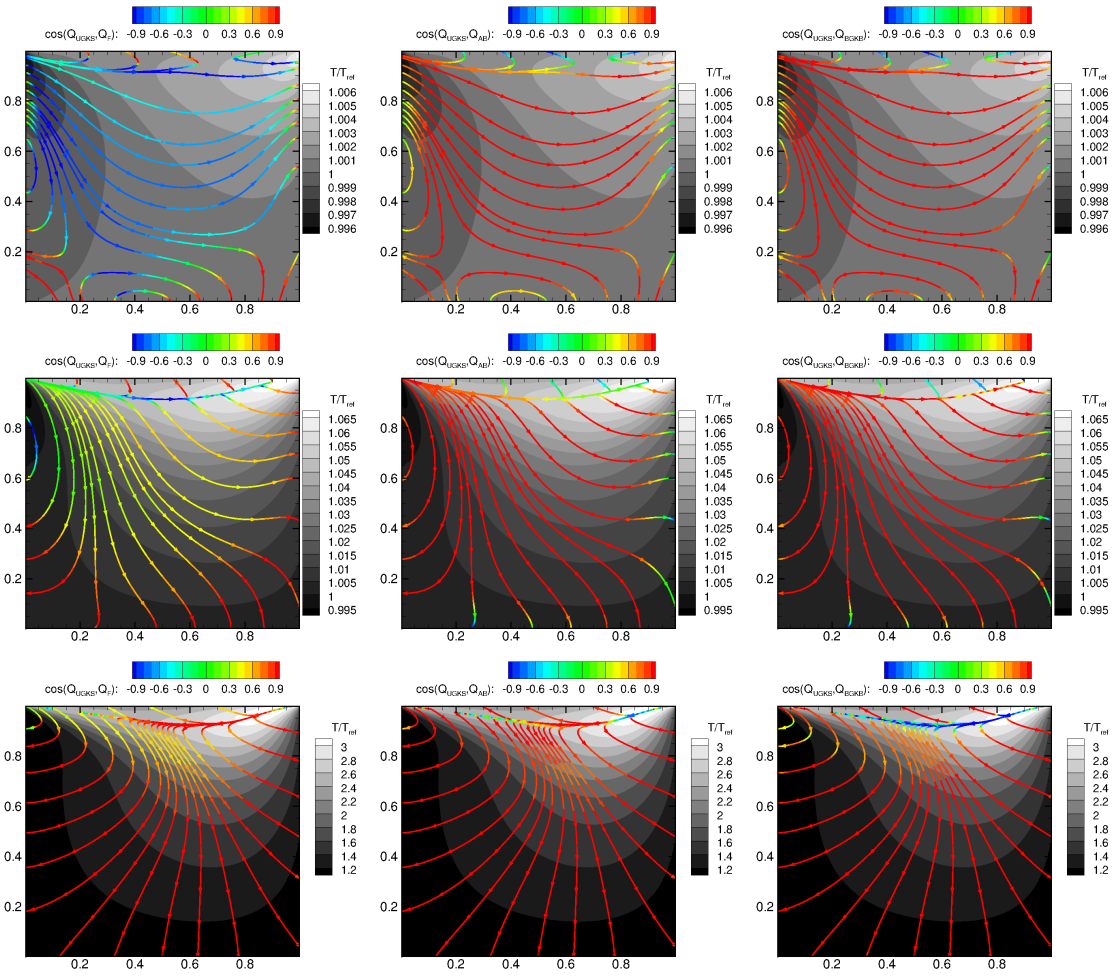


Figure 4.10: Alignment of Fourier, augmented Burnett and BGK-Burnett heat flux with UGKS flux for cavity with $AR = 1.0$ at $Kn_g = 0.1$ and $M_{lid} = 0.1$ (row 1), $M_{lid} = 0.5$ (row 2), $M_{lid} = 3.0$ (row 3); Temperature contours overlaid with heat flux streamlines colored by $cos(Q_{UGKS}, Q_F)$ (column 1), $cos(Q_{UGKS}, Q_{AB})$ (column 2), $cos(Q_{UGKS}, Q_{BGKB})$ (column 3)

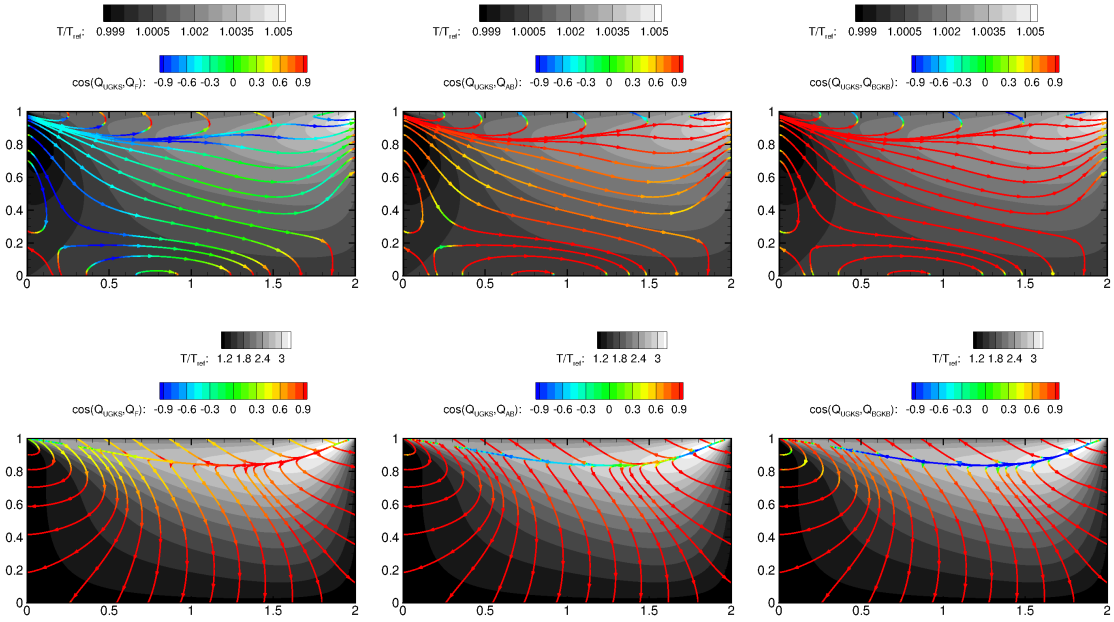


Figure 4.11: Alignment of Fourier, augmented Burnett and BGK-Burnett heat flux with UGKS flux for cavity with $AR = 2.0$ at $Kn_g = 0.1$ and $M_{lid} = 0.1$ (row 1), $M_{lid} = 3.0$ (row 2); Temperature contours overlaid with heat flux streamlines colored by $cos(Q_{UGKS}, Q_F)$ (column 1), $cos(Q_{UGKS}, Q_{AB})$ (column 2), $cos(Q_{UGKS}, Q_{BGKB})$ (column 3)

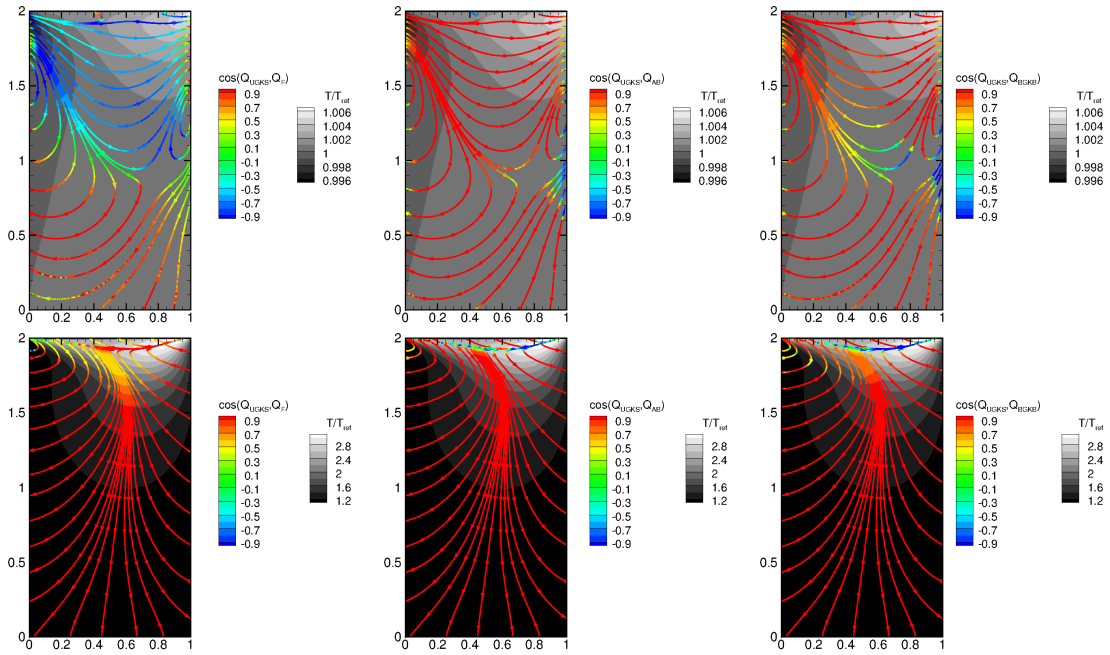


Figure 4.12: Alignment of Fourier, augmented Burnett and BGK-Burnett heat flux with UGKS flux for cavity with $AR = 0.5$ at $Kn_g = 0.1$ and $M_{lid} = 0.1$ (row 1), $M_{lid} = 3.0$ (row 2); Temperature contours overlaid with heat flux streamlines colored by $cos(Q_{UGKS}, Q_F)$ (column 1), $cos(Q_{UGKS}, Q_{AB})$ (column 2), $cos(Q_{UGKS}, Q_{BGKB})$ (column 3)

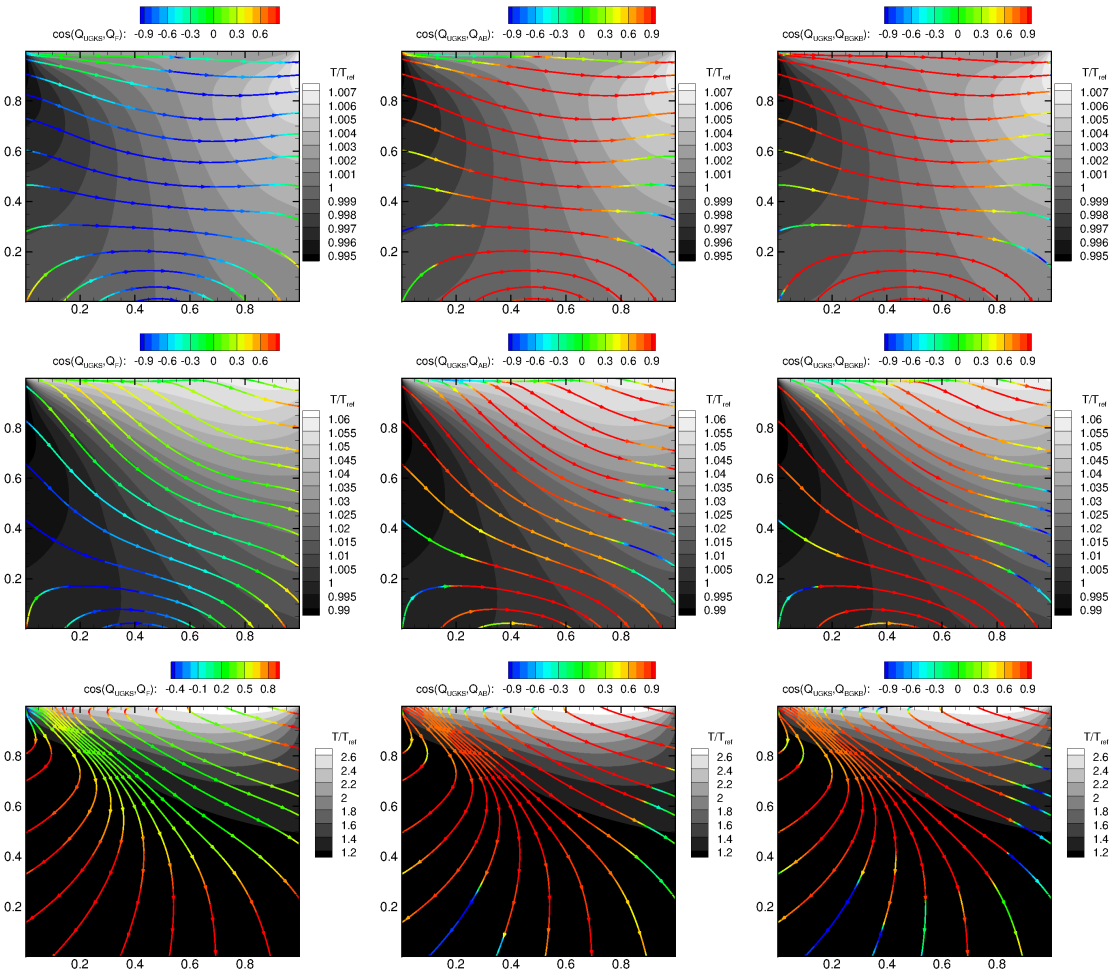

Figure 4.13: Alignment of Fourier, augmented Burnett and BGK-Burnett heat flux with UGKS flux for cavity with $AR = 1.0$ at $Kn_g = 2.0$ and $M_{lid} = 0.1$ (row 1), $M_{lid} = 0.5$ (row 2), $M_{lid} = 3.0$ (row 3); Temperature contours overlaid with heat flux streamlines colored by $cos(Q_{UGKS}, Q_F)$ (column 1), $cos(Q_{UGKS}, Q_{AB})$ (column 2), $cos(Q_{UGKS}, Q_{BGKB})$ (column 3)

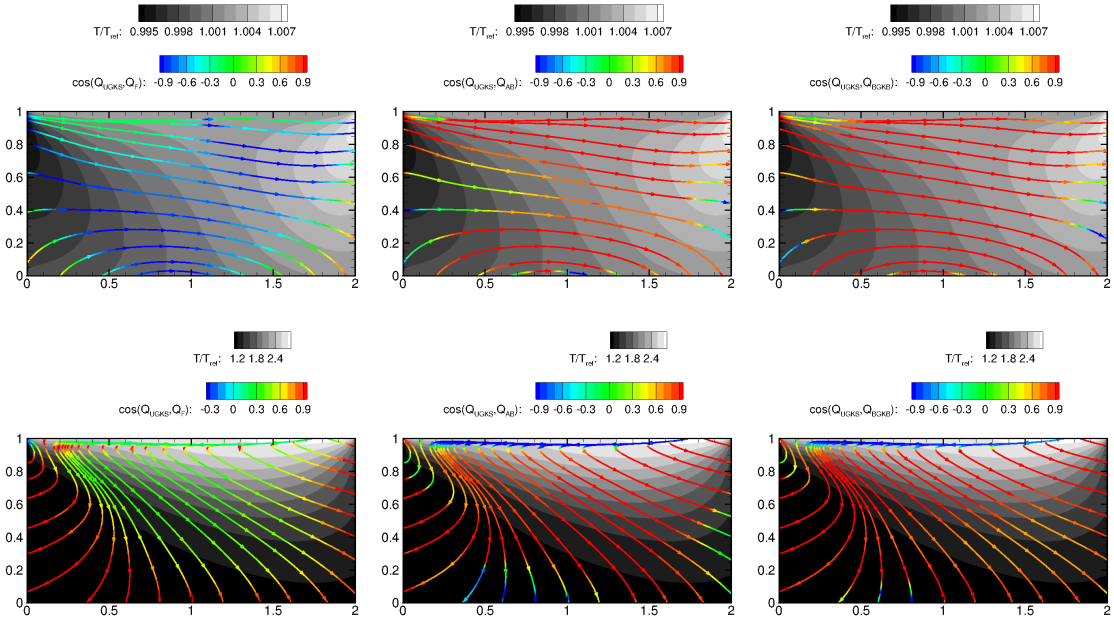


Figure 4.14: Alignment of Fourier, augmented Burnett and BGK-Burnett heat flux with UGKS flux for cavity with $AR = 2.0$ at $Kn_g = 2.0$ and $M_{lid} = 0.1$ (row 1), $M_{lid} = 3.0$ (row 2); Temperature contours overlaid with heat flux streamlines colored by $cos(Q_{UGKS}, Q_F)$ (column 1), $cos(Q_{UGKS}, Q_{AB})$ (column 2), $cos(Q_{UGKS}, Q_{BGKB})$ (column 3)

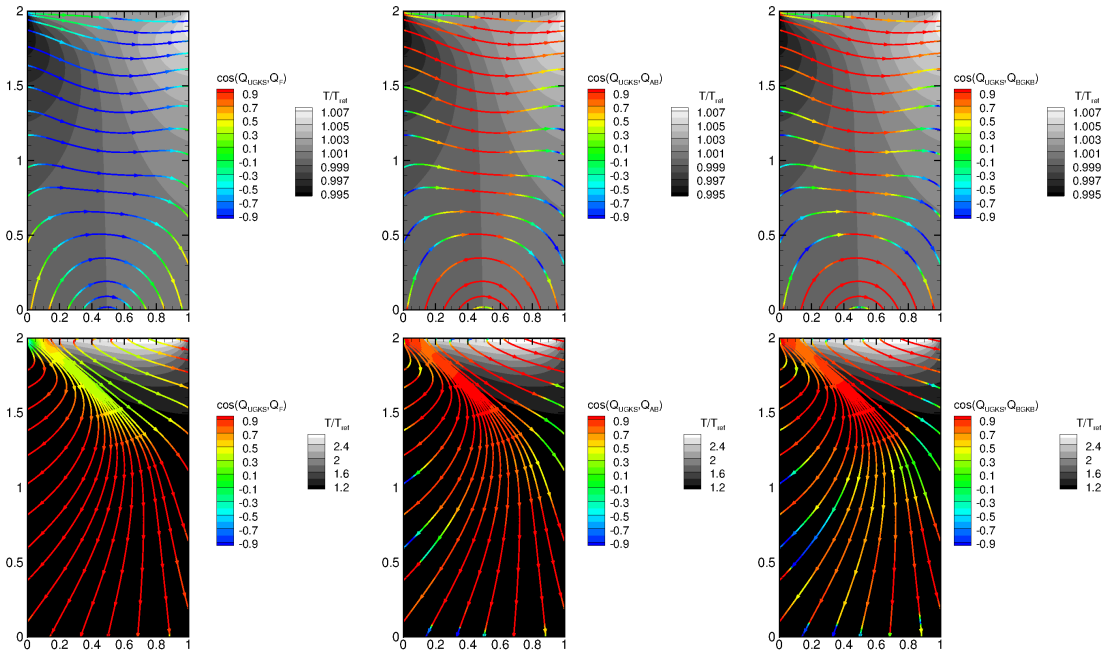


Figure 4.15: Alignment of Fourier, augmented Burnett and BGK-Burnett heat flux with UGKS flux for cavity with $AR = 0.5$ at $Kn_g = 2.0$ and $M_{lid} = 0.1$ (row 1), $M_{lid} = 3.0$ (row 2); Temperature contours overlaid with heat flux streamlines colored by $cos(Q_{UGKS}, Q_F)$ (column 1), $cos(Q_{UGKS}, Q_{AB})$ (column 2), $cos(Q_{UGKS}, Q_{BGKB})$ (column 3)

deviation indicating that the UGKS flux is in opposite direction to the respective model flux. It is also worth mentioning about the sequence of the figures prior to analyses, as they follow a recurring pattern. The sets of figures are divided into four groups based on the global Knudsen number. Figures 4.4-4.6 represent continuum flows, Figures 4.7-4.9 represent near-continuum flows, Figures 4.10-4.12 represent transition flows and Figures 4.13-4.15 represent rarefied flows. In each group, the first set of figures show results for cavities with $AR = 1.0$ (Figures 4.4, 4.7, 4.10, 4.13), the second set for $AR = 2.0$ (Figures 4.4, 4.7, 4.10, 4.13) and the third set for $AR = 0.5$ (Figures 4.4, 4.7, 4.10, 4.13). As mentioned earlier, the flows are also categorized into three regimes based on the lid Mach number. All three regimes are illustrated for square cavities, whereas for $AR = 2.0$ and $AR = 0.5$, only the extreme cases are presented. Hence, for each set of figures the top row represents low-speed cases ($M_{lid} = 0.1$) and the bottom row represents supersonic cases ($M_{lid} = 3.0$). In the cases where $AR = 1.0$, the middle row represents compressible subsonic flow ($M_{lid} = 0.5$).

Cavity flows in the continuum region ($Kn_g = 0.001$) are shown in Figures 4.4, 4.5 and 4.6 for cavity aspect ratios of 1, 2 and 0.5 respectively. In continuum, it can be seen that the heat flux components of augmented Burnett and BGK-Burnett (second and third columns) are in good agreement with that of UGKS with all lid speeds and cavity aspect ratios. Whereas the flux vectors of Fourier model show significant deviation from the UGKS flux vectors in the low-speed flows ($M_{lid} = 0.1$) for all cavity aspect ratios. It can be also seen that these errors from the Fourier model vanish as the lid Mach number is increased. It should be noted that the maximum change in temperature within the cavity domain is much smaller ($\sim 0.5\%$) in the continuum low-speed flows as opposed to corresponding high-speed flows ($\sim 30\%$ for $M_{lid} = 0.5$ and $\sim 300\%$ for $M_{lid} = 3.0$). From these observations, it can be concluded that there

is minimum threshold imposed on the temperature gradients even in the continuum limit, below which the heat flux might not be linearly dependent on the temperature gradients. It can be inferred that a reasonable temperature gradient is not generated in the case of continuum low-speed flows in order to assume a Fick's law based empirical model that assumes a non-physical infinite speed heat conduction. In a microscopic point of view, this behavior clearly indicates that the local gradients in the inter-molecular collision frequency (that are directly proportional to the respective temperature gradients) are too low such that the associated length scales are in the order of mean free path of the molecules. This demands the requirement of an extended thermodynamic model such as augmented-Burnett or BGK-Burnett model to accurately capture the thermal transport behavior.

The implications from the set of continuum experiments are more pronounced when the global Knudsen number is increased to 0.01. These flow regimes fall in the near-continuum limit and are shown in Figures 4.7, 4.8 and 4.9. As expected, it can be clearly seen in these figures that the augmented Burnett and the BGK-Burnett heat flux aligns exactly with the UGKS heat flux throughout the cavity domain for all cases. The Fourier flux vectors show significant deviations that disappear with an increase in the lid Mach number. It should also be noted that UGKS fluxes are in accordance with the Fourier model deeper into the cavity away from moving lid (see Figure 4.9). The molecules accumulate deep in the cavity forming a local continuum media, whereas the regions near to the lid suffers from additional rarefaction. This relative difference in the number density increases with an increase in the lid Mach number. Formation of rarefied region would mean a decrease in the corresponding local number of inter-molecular collisions and hence, an increase in the relaxation time − the average time (or number of inter-molecular collisions) required for the molecules to reach its local equilibrium thermodynamic state. In

near-continuum cavity flows, the local relaxation times at regions in the vicinity of the lid becomes larger than the perturbation time scale of the moving lid. The corresponding molecules are then in a state of local thermodynamic non-equilibrium and it becomes obvious that the Fourier model that is based on equilibrium state properties fail in predicting the heat flux components.

Figures 4.10, 4.11 and 4.12 illustrate the results when the global Knudsen number is set to a typical transition regime of 0.1. One could now clearly classify the locally rarefied and continuum regions that are developed in the cavity at high lid Mach numbers. The Fourier model starts to predict the right direction of heat flow away from the lid as the lid velocity is increased. Moreover, as opposed to the previous cases, the augmented Burnett and BGK-Burnett fluxes are not in agreement with the UGKS fluxes near the cavity walls. Interestingly, the corresponding Fourier fluxes near the cavity walls are reasonably accurate. Therefore, it can be inferred that the higher order terms in the Burnett equations fail at the boundaries. It is worth mentioning here that the temperature slip and the velocity slip are significant at these Knudsen numbers. In other words, the macroscopic properties adjacent to the cavity walls are no longer equal to the properties at the wall boundary as one approaches high degrees of rarefaction. This can trigger the onset to local thermodynamic non-equilibrium near the boundaries. Therefore, Burnett terms and related coefficients near wall boundaries needs further analysis in a different direction and is not discussed here. However, at higher lid Mach numbers, the Burnett flux deviations appear only near the moving lid which can be attributed to the non-equilibrium effects due to slip and induced rarefaction, while the deeper portions in the cavity approaching a continuum state agrees well to the predictions of these higher-order models. As a comparison between the two Burnett models, at low lid Mach numbers, the BGK-Burnett model predicts the flux vectors with reasonable accuracy than the

augmented Burnett model. At high lid Mach numbers, this trend is reversed where the BGK-Burnett model is less accurate compared to augmented Burnett model.

Finally, fully rarefied cavity flows ($Kn_g = 2.0$) are simulated and the results are shown in Figures 4.13, 4.14 and 4.15. The Fourier fluxes completely fail in the low-speed regime. In high-speed flows, the Fourier fluxes agree with UGKS fluxes much deeper in the cavity than in earlier cases. As the initial degree of rarefaction is increased, the non-equilibrium effects are now diffused more into the cavity domain. The failure of higher order Burnett models near the wall boundaries and its effects on to the interior domain is clearly observed while comparing the deviation measures in a narrow cavity (Figure 4.14) with that of a corresponding deep cavity (Figure 4.15). Also, the relative trends between augmented Burnett and BGK-Burnett is illustrated with much clarity in this rarefied case.

Overall, the section can be summarized with the following statements:

1. Lack of significant temperature gradients can lead to inaccurate Fourier fluxes even in the continuum limit, which in the case of cavity flows happens at very low flow speeds.

2. From near-continuum to highly rarefied flows, a cavity flow eventually develops two partitions with an increase in the lid Mach number. The upper part in the vicinity of the moving lid tends to become more rarefied with regions of local thermodynamic non-equilibrium while the deeper portions away from the cavity form a continuum region which are in equilibrium with their corresponding local macroscopic state.

3. Regions of high velocity and temperature slip appear near the cavity walls as the degree of rarefaction is increased. This in turn contributes to non-equilibrium effects that are outspread into the cavity domain with higher rar-

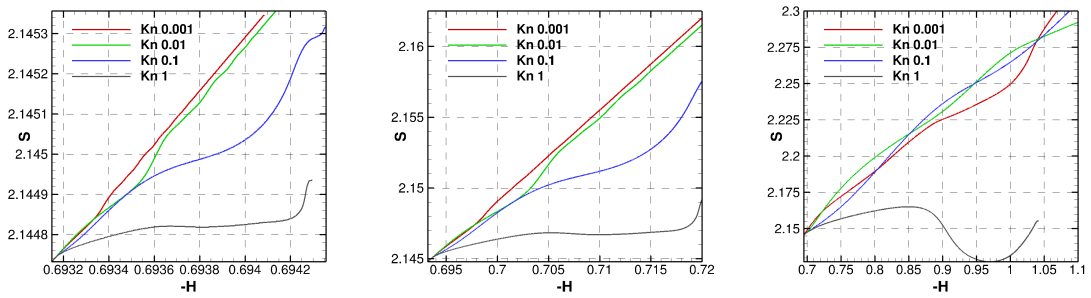


Figure 4.16: Evolution of $S_{tr}$ with $-H$ (a) Mach 0.1 (b) Mach 0.5 (c) Mach 3.0

efaction. Consequently, the higher order terms in the augmented Burnett and BGK-Burnett models fail to predict these non-equilibrium effects near the wall.

4. Thermal fluxes predicted by both the extended thermodynamic models are accurate throughout the continuum and near-continuum regimes. However, in the transition and rarefied regime, BGK-Burnett model is more accurate than augmented-Burnett model for low-speed flows and exhibits a reversed trend in accuracy for high-speed flows.

## 4.7 Second Law Analysis of UGKS

Thermal transport behavior for cavity flows exhibits high sensitivity to freestream rarefaction and flow speed. Cavity flows with extreme degrees of rarefaction involved seemingly impossible counter-counter gradient (CCG) heat transfer. It is therefore critical to perform a second law analysis of the UGKS results to check for its consistency, thereby confirming the physical validity of such transport behavior.

Temporal evolution of $S_{tr}$ and $H$ for the cavity flow is analyzed in this section. In order to keep the system isolated from the universe, the wall boundary conditions are changed to adiabatic type. In a finite time interval, the only constant entropy that is then being added into the system is due to the lid which is moving at a constant

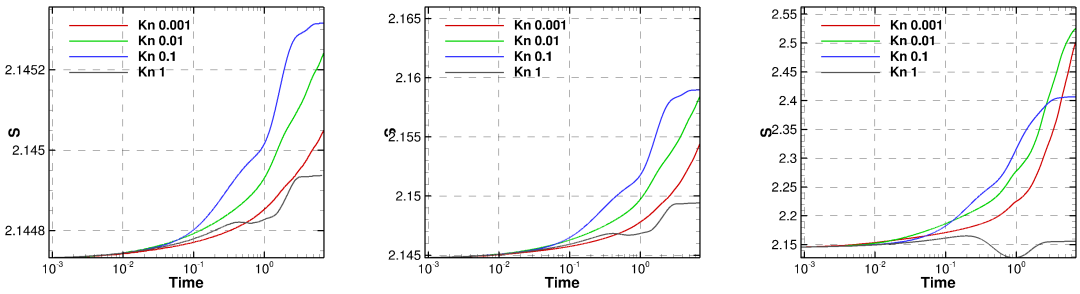


Figure 4.17: Evolution of $S_{tr}$ with time (a) Mach 0.1 (b) Mach 0.5 (c) Mach 3.0

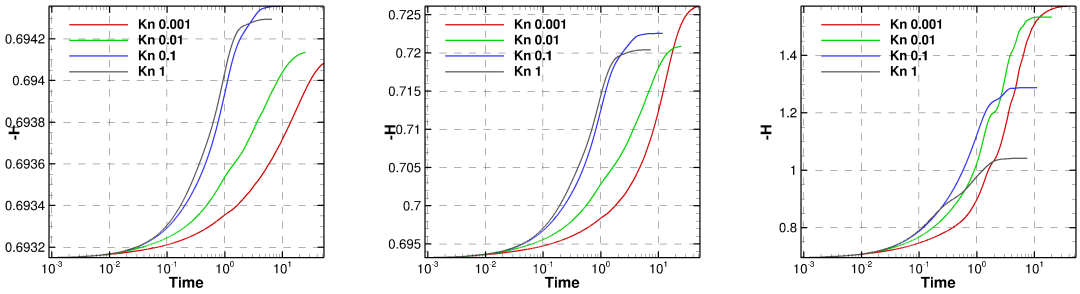


Figure 4.18: Evolution of $-H$ with time (a) Mach 0.1 (b) Mach 0.5 (c) Mach 3.0

speed. However, this should not affect the analysis as we are looking at the rate of change in system entropy with time.

Figure 4.16 compares the evolution of $S_{tr}$ with that of $-H$ for the whole cavity domain at different lid Mach numbers and freestream Knudsen numbers. It can be seen that $S_{tr}$ increases monotonically with $-H$ at low Knudsen number (continuum and near-continuum) flows which can be attributed to the absence of high non-equilibrium regions in the system. It can also be noticed that in these continuum and near-continuum flows, $S_{tr}$ maintains a direct proportionality to $-H$ as the flow evolves. With an increase in the degree of rarefaction, $S_{tr}$ decreases even though $-H$ evolves incrementally. This can be clearly seen in Figures 4.17 and 4.18 where the

temporal evolution of $S_{tr}$ and $-H$ are plotted separately. One could conclude that an entropy criteria with $S_{tr}$ can be applied only to continuum or near-continuum flows where regions of high non-equilibrium are not easily triggered. This is because the Sackur-Tetrode entropy formulation depends on thermodynamic state variables at equilibrium. The contribution to $S_{tr}$ due to the non-equilibrium effects like the extreme rarefaction effects and velocity/temperature slip effects at cavity walls are taken into account. From Figure 4.18, it can be inferred that the temporal evolution of the Boltzmann's $H$ function is consistent with the Boltzmann's $H$ theorem. In other words, the average change in the number of molecules jumping from one velocity class to the other keeps decreasing over time. Hence, from these analyses we could conclude that: (a) The flow field generated by the numerical schemes that we used do not violate Boltzmann's H theorem and the CCG heat transfer proves to be physically possible phenomena. (b) Bolzmann's $H$ theorem is universal and should be invoked to analyze the validity of flow fields accompanied with high non-equilibrium regions.

## 4.8 Conclusion

Thermal transport behavior is analyzed for cavity flows of different aspect ratios and are characterized as a function of global Knudsen number and lid Mach number. An increase in the flow speed constraints the regions of non-equilibrium to the vicinity of the moving lid. Extended hydrodynamic models like Burnett models could accurately capture the thermal transport in the continuum and near-continuum regime irrespective of the cavity aspect ratio and lid Mach number. In transition and rarefied flows, the extended thermodynamic models efficiently represent the heat transport behavior away from the cavity walls. Augmented Burnett model captures the heat flux vectors better than the BGK-Burnett model in supersonic flow regime. The thermal transport phenomena in cavity flow simulations using Unified Gas Kinetic

Scheme do not violate Boltzmann's $H$ theorem and further validates the physical existence of counter-counter-gradient heat transfer. Bolzmann's $H$ theorem is universal and should be invoked to analyze the validity of flow fields accompanied with high non-equilibrium effects.

# 5. VORTEX STRUCTURE IN TRANSITIONAL CAVITY FLOWS

We examine the change in vorticity structure as a function of Mach ($Ma$) and Knudsen ($Kn$) numbers. The physical mechanisms involved in the production of different vortex structures in different parameter regimes are highlighted. In the rarefied regime, we characterize the mechanism in terms of molecular number density and collision frequency as continuum terminology may not be applicable. Finally, we classify different regimes of vortex structures in Ma-Kn space.

## 5.1 Introduction

Figure 5.1 presents a schematic of Knudsen number distribution within the cavity when the freestream flow is rarefied. When the flow is initiated, freestream molecules enter the cavity volume. The molecules penetrate different depths depending upon the initial conditions. The molecules then experience collisions (a) with incoming molecules and (b) with inner cavity surfaces and (c) amongst themselves. With passage of time, there is an accumulation of molecules within the cavity. The accumulation density is inversely proportional to depth. This follows from the idea that the molecules penetrating deeper into the cavity have relatively lower chance of escaping from the cavity, as their speed decrease due to frequent inter-molecular and surface collisions. This gives rise to the Knudsen number distribution illustrated in Figure 5.1. Clearly, the details of the distribution would depend upon the freestream Mach number and Knudsen number. It is equally evident that the flow structures within the cavity will be influenced by the Knudsen number distribution. For aerospace engineering applications, it is crucial to characterize these flow structures as they can significantly influence surface heat transfer and shear stress along cavity walls.

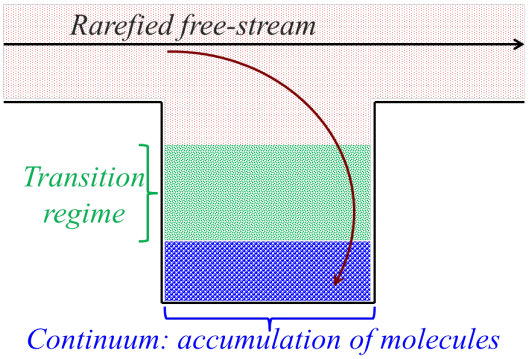


Figure 5.1: Density variations in a cavity flow

In this work, we perform a parametric study of the cavity flow simulations in order to (a) understand the physical mechanism behind the evolution of vortex structures and (b) clearly classify the vortex configurations in the parametric space under consideration. The significant parameters affecting the flow would be the speed of the flow (lid Mach number), degree of rarefaction (Knudsen number) and the cavity size (cavity aspect ratio).

### *5.1.1 Continuum Vortex Dynamics*

Typical vortex structures observed in 2D continuum cavity flows are illustrated in Figure 5.2. These continuum vortex structures that are well established in literature help to validate our current results and to bridge the various vortex evolution mechanisms between continuum and non-continuum regimes.

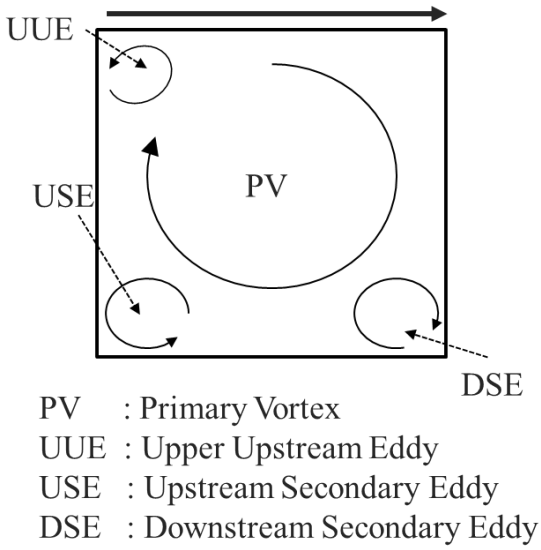


Figure 5.2: Typical vortex structures in a continuum 2D cavity

For the sake of classification, the large steady recirculation regions are defined as vortices, while the smaller unsteady recirculation regions that frequently appear near the cavity corners are called eddies. It will later be seen that these eddies play a critical role in the formation of bigger vortical structures under special circumstances. A typical form for the continuum vorticity equation derived from the Navier Stokes equation and the associated terminologies are illustrated in Figure 5.3.

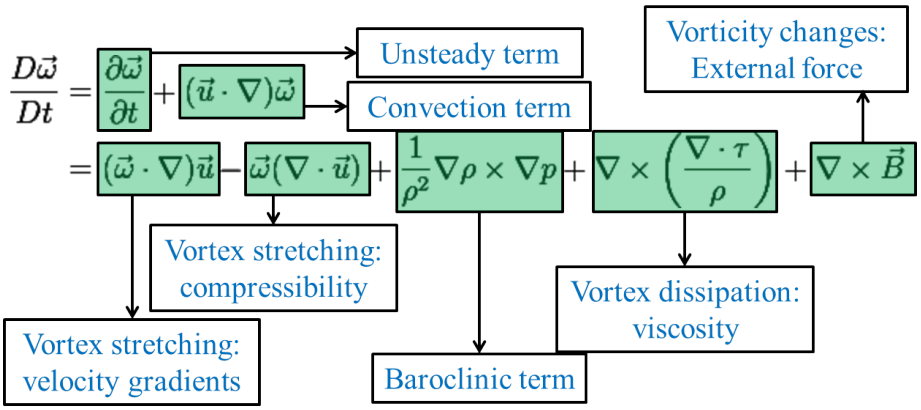


Figure 5.3: Continuum vorticity equation and terminologies

### *5.1.2 Investigating Non-Continuum Vortex Dynamics*

Definition of 'vortex' is still valid in non-continuum regimes. However, the difference lies in the fact that continuum terminologies break down in rarefied regions. The continuum transport terms and hence the vorticity dissipation term in Figure 5.3 will be the first one to deviate as one approaches non-continuum limit. Hence, in the near-continuum to rarefied limit, we seek an explanation based on the more fundamental gas kinetic theory. In particular, it is observed that the vortex evolution and their interaction are highly correlated with the number density, collision frequency and near-stagnant regions in the flow field.

The objective of this work is to explain the relevant physical mechanisms underlying the evolution of vortex structures in a cavity flow with non-continuum effects and hence bridge the gap from rarefied to continuum vortex dynamics. Toward this objective, we perform numerical simulations of two-dimensional lid-driven cavity flows for a wide range of parameters. The flow structures are examined as functions of flow speed, degree of rarefaction and cavity aspect ratio. An effort is made to cover the maximum relevant parameter space; from low-speed incompressible to super-

sonic compressible, from highly rarefied to continuum and from wide to square to deep cavities. We perform the numerical simulations with a Unified Gas Kinetic Scheme (UGKS) which can handle extreme density variations and resolve associated non-equilibrium effects in the flow field.

## 5.2 Simulation Parameters

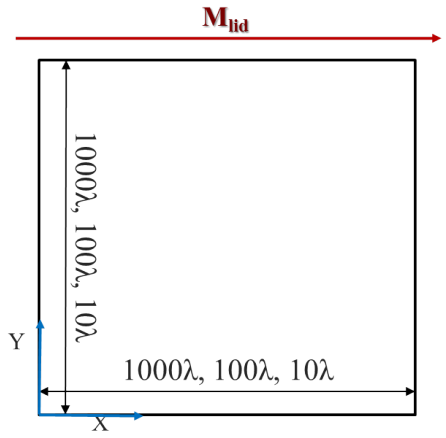


Figure 5.4: Geometry

2D UGKS simulations are performed for the flow of Argon gas within a cavity driven by a lid moving at a constant velocity of $U_{lid}$. The degree of rarefaction is set using the global (freestream) Knudsen number, which is the ratio between the mean free path of the molecules in the freestream ($\lambda_\infty$) to the global length scale ($L$). The characteristic length ($L$) is varied from $1000\lambda_\infty$ to $\lambda_\infty$ to account for analysis from a continuum to an extremely rarefied flow. Cavities of different sizes are considered by varying the aspect ratio ($AR$) which is defined as the ratio of the height of the cavity to the length of the lid. The aspect ratios considered in this study, for a square, deep

and wide cavity are shown in Table 5.1.

| $AR$ | Height | Width |
|---|---|---|
| 1.0 | $1.0L$ | $1.0L$ |
| 2.5 | $2.5L$ | $1.0L$ |
| 0.4 | $1.0L$ | $2.5L$ |

Table 5.1: Height and width for various cavity sizes

All cavity walls including the lid are set to be isothermal, maintaining a temperature of $T_{wall}$ which is set to the reference temperature $T_{ref} = 273K$. The CFL number is 0.9 and the grid points in each direction are uniformly spaced. The grid sensitivity results suggested this spacing to be $L/90$ i.e, $N_x \times N_y = 90 \times 90$ when $AR = 1$, $90 \times 225$ when $AR = 2.5$ and $225 \times 90$ when $AR = 0.4$; where $N_x$ and $N_y$ are the number of divisions along $x$ and $y$ respectively. For extreme non-equilibrium cases (high Mach and Knudsen numbers), integration over velocity space is performed based on Newton-Cotes quadrature with 100 points in each direction. For all other cases, a Gauss-Hermite quadrature is used with 28 weights in each direction.

The lid Mach number is varied from 0.1 to 3.0 in steps of 0.1. Hence, the cavity flow in incompressible, compressible subsonic and supersonic regimes are simulated. The Knudsen number is varied from 0.001 to 1.0, thereby covering continuum to rarefied cases.

## 5.3 Results and Discussion

The UGKS code has been extensively validated from low-speed and continuum flows to highly non-equilibrium high-speed and rarefied flows [46, 19, 20, 43]. The current section is divided into two parts. Different flow structures are presented in the first part to examine their correlation with the flow parameters under consideration. The second part deals with an extensive analysis of the vortex evolution mechanism. Finally, a vortex-structure map is developed. This map delineates the Mach-Knudsen number space into different regions of distinct vorticity structures.

### *5.3.1 Flow Structures: Observations*

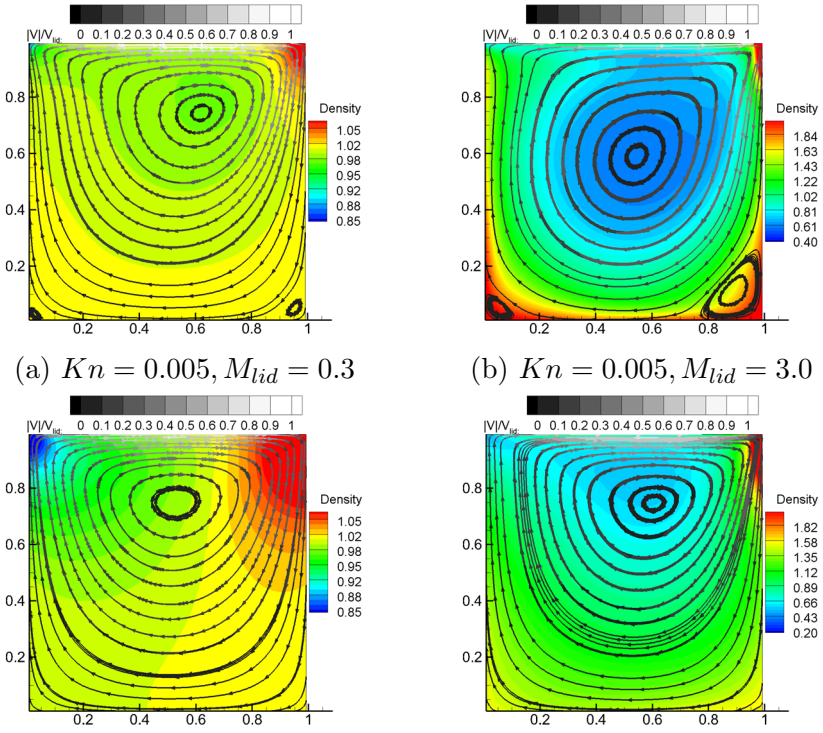


(a) $Kn = 0.005, M_{lid} = 0.3$ (b) $Kn = 0.005, M_{lid} = 3.0$

(c) $Kn = 0.05, M_{lid} = 0.3$ (d) $Kn = 0.05, M_{lid} = 3.0$

Figure 5.5: Streamlines colored with velocity magnitude and density contours (background) for $AR = 1.0$

Figures 5.5 and 5.6 show the streamlines inside a square cavity at various Knudsen and lid Mach numbers that are chosen to illustrate the transformation in the flow structures. The gray-scale coloring of these streamlines represents the velocity magnitudes that are non-dimensionalized with the lid velocity. It should be observed that the velocity magnitude significantly decreases as one goes deeper into the cavity. The upstream secondary eddy (USE) and downstream secondary eddy (DSE) start appearing with a decrease in the degree of rarefaction (see figures 5.5 (a) and (b)). The size of USE and DSE sizes increase with increasing lid velocity (see figures 5.5 (a) and (b), Figure 5.6). A low-speed rarefied cavity flow features only a primary vortex, with its outermost streamlines nearly adhering to the cavity walls (see Figure 5.5 (c)). Therefore, in general, approaching to continuum or increasing the flow speed in a square cavity favors the formation of USE and DSE, and eventually they grow in size.

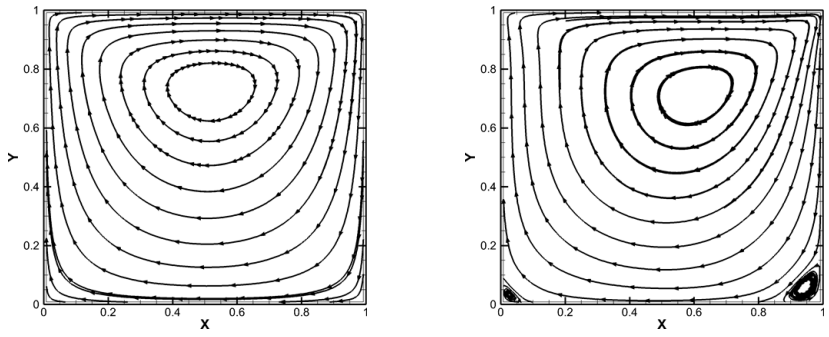


(a) $M_{lid} = 0.3$ (b) $M_{lid} = 3.0$

Figure 5.6: Streamlines for $AR = 1.0, Kn = 0.01$

The background in Figure 5.5 shows the density contours. For cavities exposed to high flow speed and low rarefaction, it can be observed that density is higher in

the lower part of the cavity (especially near the bottom corners) when compared to the core of the primary vortex (see figures 5.5 (a), (b) and (d)).

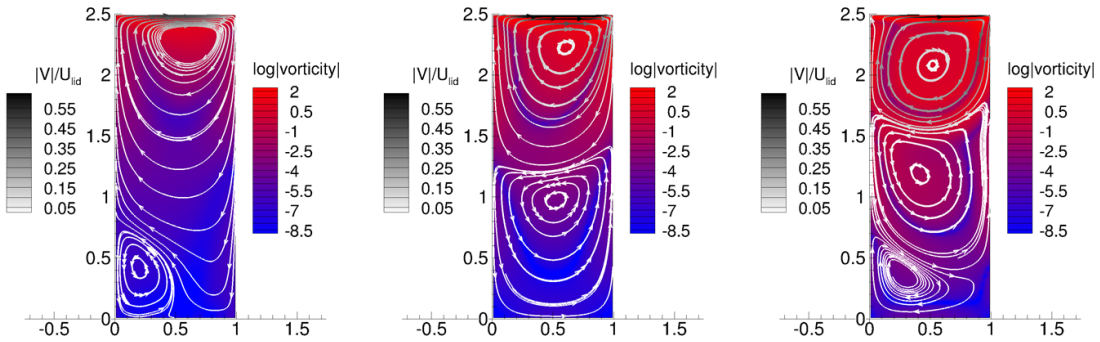


Figure 5.7: Streamlines colored with velocity magnitude and vorticity magnitude contours (background) for $AR = 2.5$, $M_{lid} = 3$ and $Kn_g = 1, Kn_g = 0.05, Kn_g = 0.005$ (left to right)

Figure 5.7 shows the streamlines inside a deep cavity with $M_{lid} = 3.0$. It can be observed that the velocity magnitude is very small, deep inside the cavity. The different configurations in the flow structures reveal that the number of vortices increase with a decrease in the global Knudsen number (or degree of rarefaction). Therefore, it is expected that with a further increase in the Knudsen number, the flow structure would simply comprise of a single primary vortex with no secondary eddies or vortices [43]. For deep cavities, it is also observed that the effect of decreasing lid Mach number is equivalent to the effect of increasing Knudsen number [31]. The background in the Figure 5.7 is the vorticity magnitude contour plotted in *log* scale. The primary vortex (vortex closest to the lid) has the maximum vortex strength and it significantly decreases for secondary and subsequent higher order vortices. Figure 5.8 illustrates the density contours for a deep cavity at different Mach and

Knudsen numbers. A lid moving at high-speed compresses fluid deeper into the cavity resulting in a higher density in the lower half of the cavity compared to the upper half (compare figures 5.8 (a) and (b) to figures 5.8 (c) and (d)). In a microscopic perspective, this effect can be attributed to the increasing entrapment of the molecules near the bottom half of the cavity, which will be elucidated in the next section.

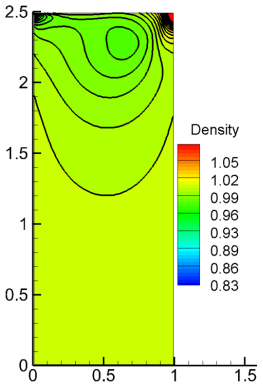


(a) $Kn = 0.005, M_{lid} = 0.3$

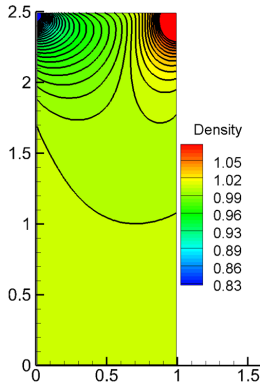


(b) $Kn = 0.05, M_{lid} = 0.3$

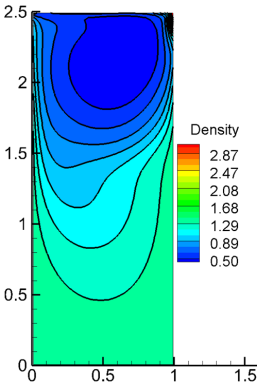


(c) $Kn = 0.005, M_{lid} = 3.0$

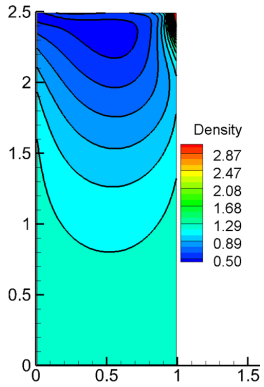


(d) $Kn = 0.05, M_{lid} = 3.0$

Figure 5.8: Density contours for $AR = 2.5$

Flow structures in a high-speed flow in a wide cavity are illustrated in Figure 5.9. The streamline coloring represents the velocity magnitude and the background

shows the vorticity magnitude contour in *log* scale. It can be observed that only the primary vortex prevails at higher Knudsen numbers. USE and DSE start appearing with a decrease in Knudsen numbers. In all the cases, the core of the primary vortex is on the right (downstream) side of the cavity. A secondary vortex appears with further decrease in the degree of rarefaction. The primary vortex still remains but its shape gets distorted due to continuum no-slip boundary conditions. It should also be noted that the vortex strength and the velocity magnitude are smaller for a secondary vortex and much smaller for USE and DSE. Figure 5.10 shows the density contours at different Mach and Knudsen numbers for wide cavities. At high Mach numbers, density is higher at the bottom corners compared to the cavity center (figure 5.10 (d)). High-speed continuum flows in wide cavities give rise to a denser left half (upstream side) compared to the downstream side (figure 5.10 (c)). In low-speed flows, it is observed that the density gradients are smaller compared to high-speed flows (compare figures 5.10 (a) and (b) to figures 5.10 (c) and (d) respectively). In general, the effect of decreasing flow speed is similar to the effect of increasing Knudsen number [43].

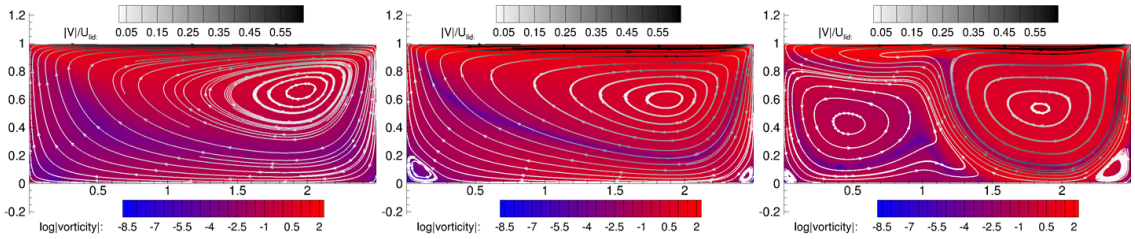


Figure 5.9: Streamlines colored with velocity magnitude and vorticity magnitude contours (background) for $AR = 0.4$, $M_{lid} = 3$ and $Kn_g = 1, Kn_g = 0.05, Kn_g = 0.005$ (left to right)

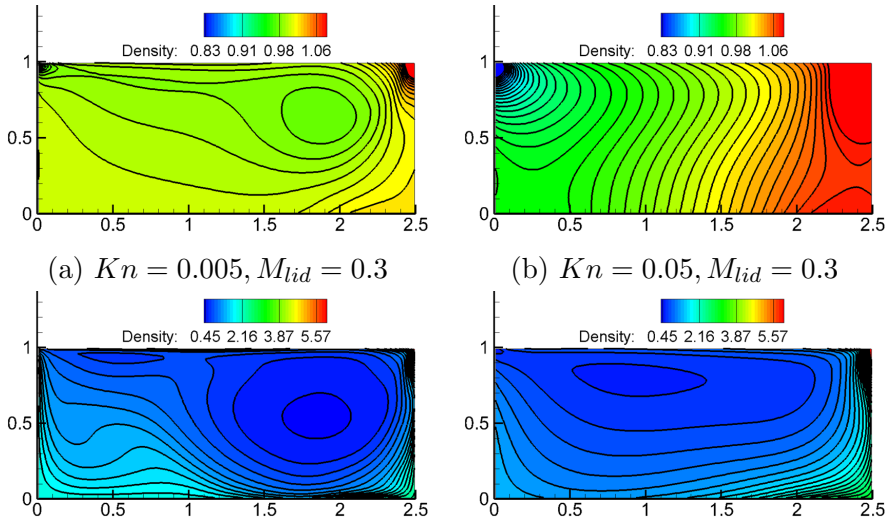


(a) $Kn = 0.005, M_{lid} = 0.3$ (b) $Kn = 0.05, M_{lid} = 0.3$

(c) $Kn = 0.005, M_{lid} = 3.0$ (d) $Kn = 0.05, M_{lid} = 3.0$

Figure 5.10: Density contours for $AR = 0.4$

### *5.3.2 Mechanism of Vortex Evolution*

Within the parameter space under consideration, local regions of high degree of non-equilibrium often appear due to rarefaction effects. Therefore, an investigation based on macroscopic quantities would not reveal the relevant mechanisms of vortex evolution. Hence, we seek an explanation based on fundamental microscopic quantities like the number density and the collision frequency.

Number density, which is defined as the number of molecules per unit volume, is equal to the density normalized with the molecular mass. Density contours for different cases are examined in the previous section. Figure 5.11 plots the variation of average density computed at three regions of a square cavity, namely the primary vortex (PV) region, upstream secondary eddy (USE) region and the downstream secondary eddy (DSE) region. The corresponding vortex/eddy structures are examined in this vicinity. The average density of these local regions is plotted against

lid Mach number at different global Knudsen numbers. At low Knudsen numbers, it should be noted that the average density of the PV region decreases with increasing Mach number, while this trend is reversed in the case of USE and DSE regions, which makes them denser. A closer observation would also reveal that this variation in density profile is much significant only at regions of high lid Mach numbers and low global Knudsen numbers. Figure 5.12 shows the collision frequency (CF) contours for a square cavity at different Mach and Knudsen numbers. For better illustration purposes, the collision frequency contour plots are normalized with the quantity $a_{ref}Kn_g/L$, where $a_{ref}$ is the speed of sound at the reference state, $Kn_g$ is the global Knudsen number, and $L$ is the characteristic length. In Figure 5.12, one can immediately observe similar patterns for figures 5.12 (a), (d), (e) and figures 5.12 (b), (c), (f). When the flow approaches continuum limit at high speeds, the collision frequency becomes dominant in the USE and DSE regions (see figures 5.12 (a), (d) and (e)). The fact that high collision frequency, high density and low velocity magnitude occur simulataneously at USE and DSE regions provides an important insight. The USE and DSE regions are made up of a near-stagnant cluster of entrapped molecules that collide with other molecules in this cluster as well as the cavity walls. This cluster of entrapped molecules form a barrier to any external particle which prevents their penetration into the USE/DSE region, subsequently diverting them from these near-stagnant regions. These DSE/USE regions, then act as independent fluid particles and gain momentum from the nearby primary vortex, eventually forming secondary eddies. It should be highlighted that a low Mach number or a high Knudsen number does not yield favorable conditions for the secondary eddies to develop at the DSE/USE region. Hence, only a primary vortex prevails at such conditions, where the flow is driven by the moving lid with only the cavity walls guiding the streamlines.

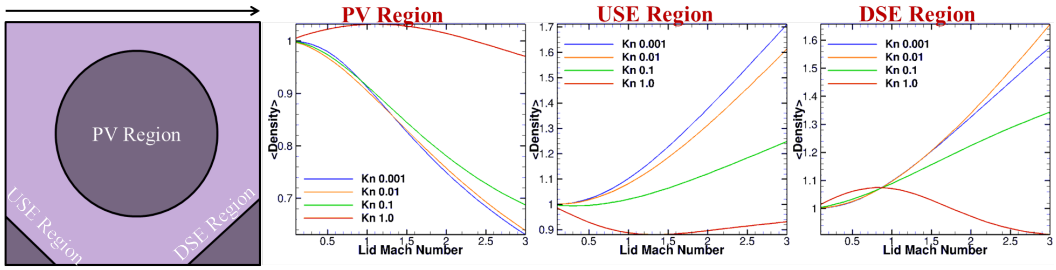


Figure 5.11: Variation of average density with Mach number

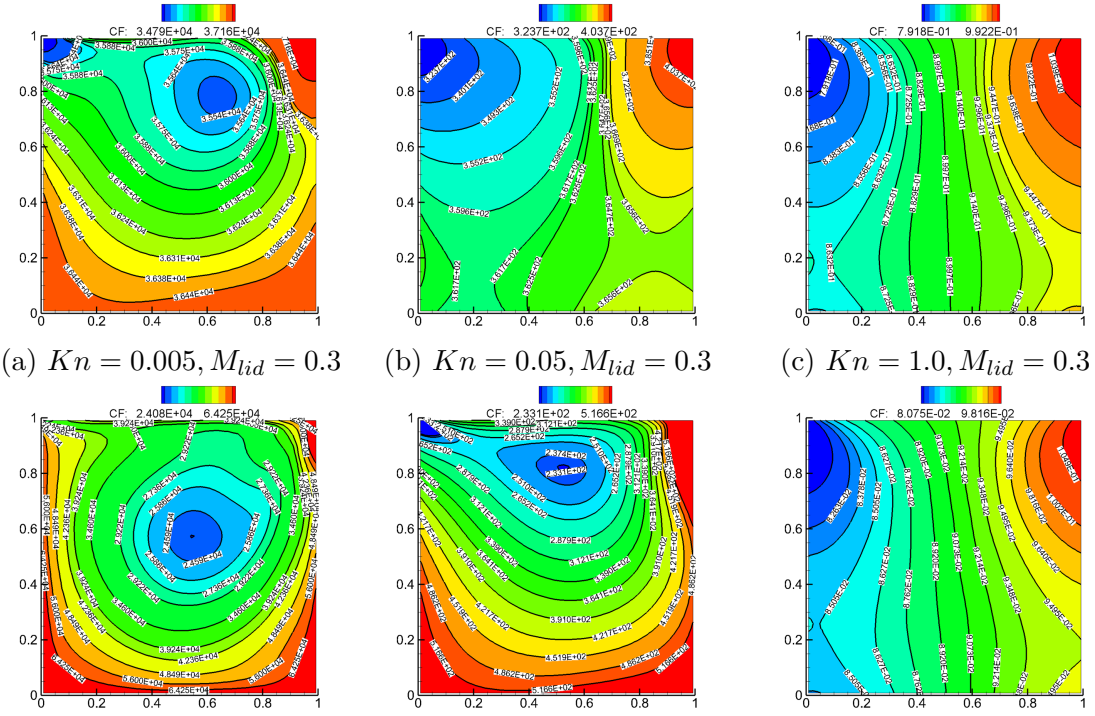

(a) $Kn = 0.005, M_{lid} = 0.3$ (b) $Kn = 0.05, M_{lid} = 0.3$ (c) $Kn = 1.0, M_{lid} = 0.3$

(d) $Kn = 0.005, M_{lid} = 3.0$ (e) $Kn = 0.05, M_{lid} = 3.0$ (f) $Kn = 1.0, M_{lid} = 3.0$

Figure 5.12: Collision frequency contours for $AR = 1.0$

The normalized collision frequency contours in deep cavity are illustrated in Fig-

ure 5.13. At low Knudsen numbers, the collision frequency increases as one traverses deeper into the cavity. The effect is much dominant in the high-speed case (figures 5.13 (d) and (e)). As discussed earlier, the effect of increasing lid Mach number is similar to the effect of decreasing Knudsen number i.e. transition from Figure 5.13 (b) to Figure 5.13 (a) is comparable to transition from Figure (b) to Figure (e). The similarity holds true for square and wide cavities as well. Except for high Knudsen numbers, the collision frequency, density and the velocity magnitude deep inside the cavity favors the formation of a near-stagnant region as in case of a square cavity. The formation of higher order vortices beneath the primary vortex in a deep cavity (given suitable conditions) can be well-understood if the depth of the cavity is thought to continually increase starting from a square cavity. Let us assume that the conditions are always favorable to form USE and DSE at the cavity corners. When we increase the depth of the cavity, the USE and DSE grow in size, as more molecules get entrapped in these regions. A further increase in the depth eventually allows the DSE and USE to meet up and merge to form a secondary vortex beneath the primary vortex. This has also been observed for very low-speed cavity flows in a previous study by Naris and Valougeorgis [31]. Subsequent increase in depth will then be followed by the formation of tertiary and higher order vortices with significant decrease in vorticity strength.

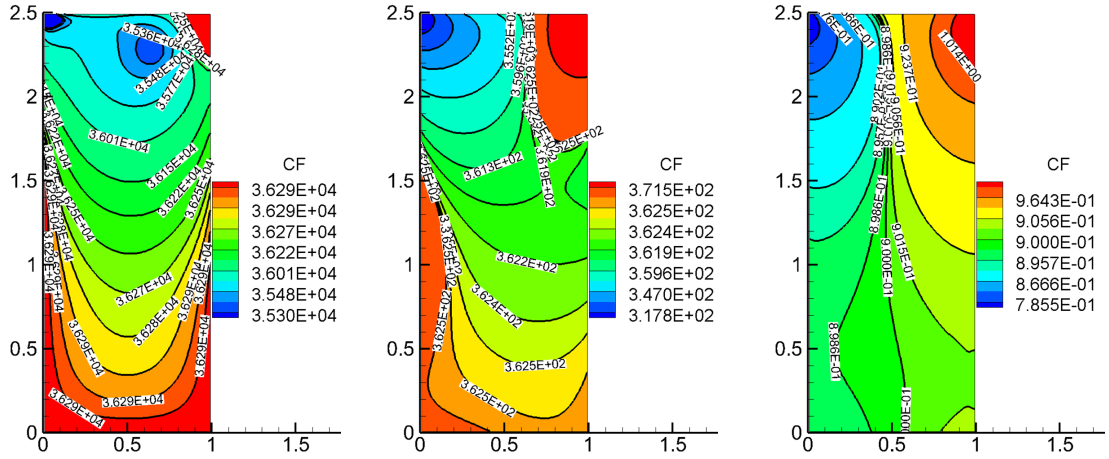


(a) $Kn = 0.005, M_{lid} = 0.3$ (b) $Kn = 0.05, M_{lid} = 0.3$ (c) $Kn = 1.0, M_{lid} = 0.3$

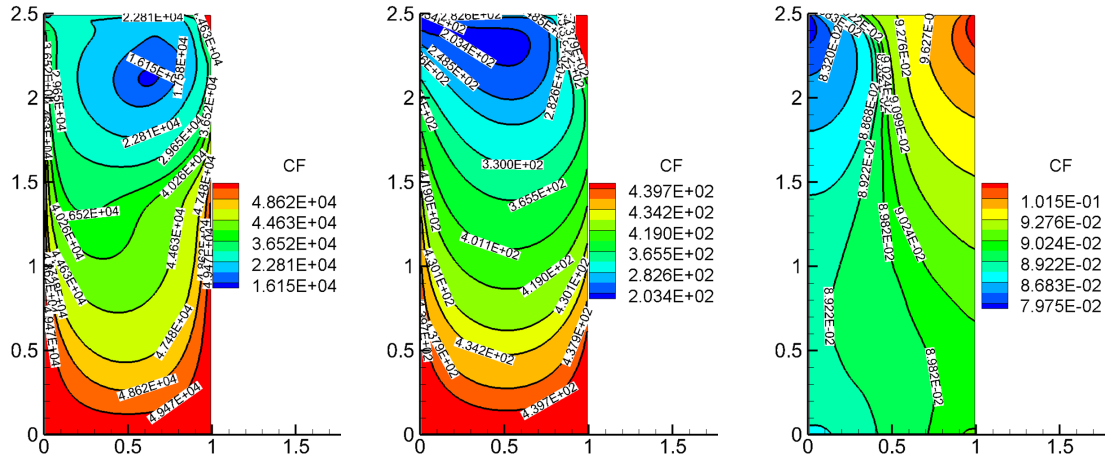


(d) $Kn = 0.005, M_{lid} = 3.0$ (e) $Kn = 0.05, M_{lid} = 3.0$ (f) $Kn = 1.0, M_{lid} = 3.0$

Figure 5.13: Collision frequency contours for $AR = 2.5$

Figure 5.14 shows the collision frequency contours in wide cavities at different Mach and Knudsen numbers. At high Knudsen numbers and low Mach numbers, the flow domain consists only of a primary vortex as we do not have a favorable collision frequency near the cavity corners (figures 5.14 (b), (c) and (f)). The streamlines are simply turned primarily due to the molecular collisions with the cavity walls. With a decrease in the Knudsen number or an increase in the lid Mach number, collision frequencies and densities suitable for the generation of secondary eddies

appear near the cavity corners (figure 5.14 (a) and (e)). As the lid Mach number is further increased, the USE grows in size as a consequence of more molecules being entrapped (figure 5.14 (d)), which eventually stabilizes to form a secondary vortex (SV). This pushes a part of the primary vortex (PV), but a distorted tail of PV still remains between the lid and SV, which as discussed earlier, is a consequence of the 'continuum no-slip' boundary condition of the moving lid. Tertiary and higher order vortices form with an increase in the cavity width, given that a favorable condition prevails.

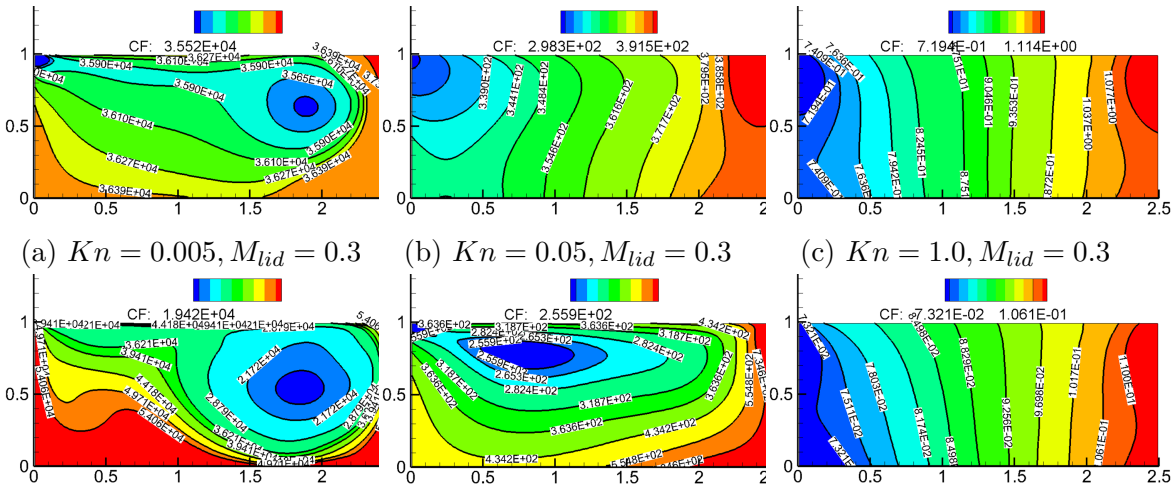


(a) $Kn = 0.005, M_{lid} = 0.3$ (b) $Kn = 0.05, M_{lid} = 0.3$ (c) $Kn = 1.0, M_{lid} = 0.3$

(d) $Kn = 0.005, M_{lid} = 3.0$ (e) $Kn = 0.05, M_{lid} = 3.0$ (f) $Kn = 1.0, M_{lid} = 3.0$

Figure 5.14: Collision frequency contours for $AR = 0.4$

To summarize, vortex-structure maps are prepared from a set of 360 simulations for square, deep and wide cavities. Figure 5.15 classifies the 'lid Mach number - global Knudsen number' space into different bands where each band represents a particular flow structure configuration. The delineation boundaries are computed based on the Gaussian Naive Bayes model [33, 9]. It should be noted from Figure 5.15 that

only the primary vortex exists in the flow domain at high degrees of rarefaction and low lid Mach numbers. The eddies and higher order vortices start appearing as one approaches continuum and this behavior could be further accelerated by increasing the lid Mach number. The chart remains almost similar for deep and wide cavities, with the difference being that the wide cavities are more sensitive to the changes in the degree of rarefaction. However, the vortex evolution mechanisms are different for deep and wide cavities.

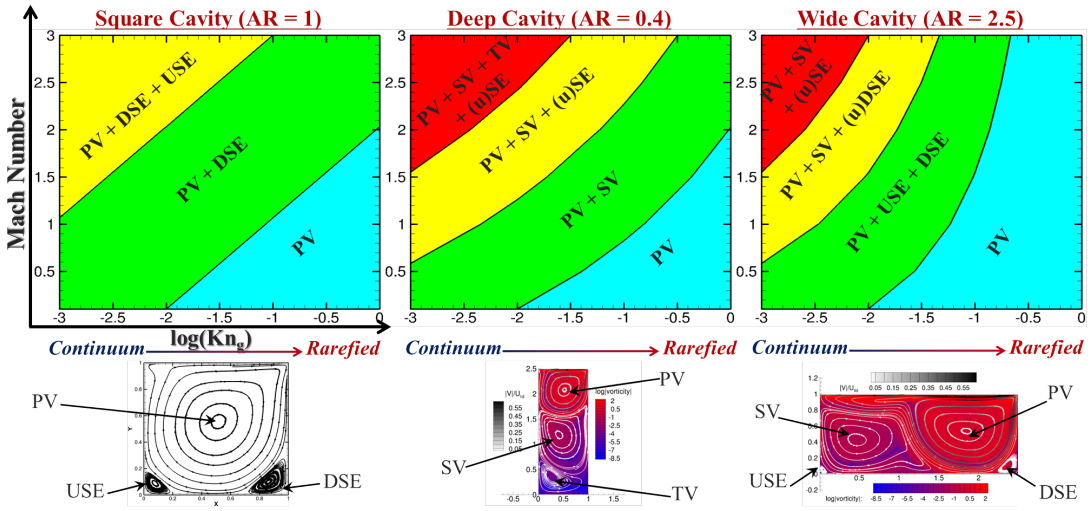


Figure 5.15: Classification of vortex configurations for square, deep and wide cavities

## 5.4 Conclusion

The vortex structures in rarefied cavity flows are examined in this study. A highly rarefied lid-driven cavity consists only of a primary vortex driven by the moving lid. The streamlines form a closed loop as a consequence of the molecules colliding solely against the cavity walls. There is not sufficient accumulation of molecules at the corners to initaite formation of corner eddies. Favorable conditions

for corner eddy formation are (a) high density of molecule accumulation, (b) high collision frequency and (c) low velocity magnitude. As the degree of rarefaction is decreased, more molecules are accumulated in the DSE/USE regions. Small velocity magnitude and high collision frequency at these regions indicate the formation of a near-stagnant cluster of molecules. These regions then act as independent collection of fluid particles creating a barrier that deflect an oncoming external molecules. The near-stagnant particles start to gain angular momentum from the nearby primary vortex to form secondary eddies. As the cavity depth is increased, more molecules get entrapped into the DSE/USE regions, allowing the eddies to grow in size. With further increase in the cavity depth, the DSE and USE merge to form a secondary vortex. The process keeps repeating with an increase in the cavity depth, given favorable flow conditions. If the width of the cavity is increased, the USE region grows in size, leading to the formation of a secondary vortex. The shape of the primary vortex distorts leaving behind a narrow extension between the secondary vortex and the 'no-slip' moving lid. Vortex structure classification maps are generated in Kn - Ma parameter space for square, deep and wide cavities. In general, it is observed that the evolution of flow structures in wide cavities are more sensitive to the degree of rarefaction than that for deep cavities.

# 6. PRANDTL NUMBER EFFECTS IN HIGH-SPEED RAREFIED CAVITY FLOWS*

A parameter that could potentially affect the thermal behavior in a rarefied cavity flow is the Prandtl number. The effects of Prandtl number were previously investigated in the continuum regime for turbulent flows [30, 36, 22]. Flow structures and thermal transport behavior are observed to be sensitive to changes in the Prandtl number in turbulent flows. However, the effect of Prandtl number in a rarefied or near-continuum regime is yet to be investigated. In this work, we perform a systematic parametric study to analyze the effects of Prandtl number variation on the thermal transport behavior in the vicinity of cavity walls.

## 6.1 Numerical Setup

UGKS simulations of 2D lid-driven square cavity flows are carried out for a lid Mach number ($M_{lid}$) of 3. The cavity dimensions are the same as discussed in Chapter 5. An extensive validation has already been performed for cavities of different aspect ratios by Venugopal and Girimaji [43]. In this study, results from two sets of numerical experiments are examined for effects due to variation of Prandtl number ($Pr$). In the first set (isothermal case), all the cavity walls including the lid are maintained at a constant temperature of $273K$, and the second one has all walls set to adiabatic boundaries. In both these sets, the freestream Knudsen numbers are 0.001, 0.01 and 0.1 representing the continuum, near-continuum and rarefied regimes respectively; and $Pr$ is varied as 0.01, 0.1, 0.5 and 1.0. $Pr$ is limited to a value of one, as the driving fluid is in the gaseous phase. All other molecular dimensions are

*Reprinted with permission from Begell House Inc. Full citation: Venugopal, Vishnu, and Sharath S. Girimaji. 'Prandtl Number Effects in High-Speed Rarefied Cavity Flows.' In Proceedings of the Eighth International Symposium On Turbulence, Heat and Mass Transfer, September 2015

based on the Variable Hard Sphere of Argon gas at a reference state of $101325Pa$ and $273K$. CFL number for the 2D simulation is set to 0.6 in all the cases.

## 6.2 Results and Discussion

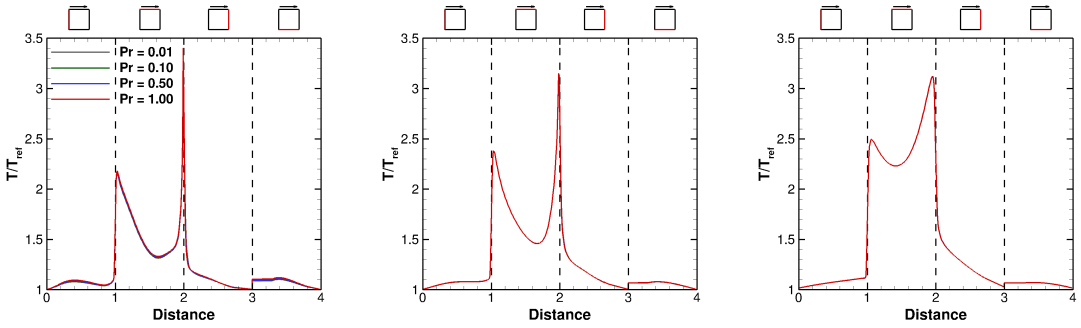


Figure 6.1: Temperature profiles along the cavity walls: steady state isothermal case, Column$[1-3] = Kn_g[0.001,\ 0.01,\ 0.1]$

Figure 6.1 shows the non-dimensional temperature profiles near the isothermal cavity walls. Variable 'Distance' is defined for the sake of clarity. 'Distance' $= 0-1$ is the left wall, 'Distance' $= 1-2$ is the top lid, 'Distance' $= 2-3$ is the right wall and 'Distance' $= 3-4$ is the bottom surface, all measured in the clockwise direction. Changes in $Pr$ do not affect the thermal profile along the cavity walls which is a consequence of the walls being maintained at a constant temperature (Figure 6.1). It is to be noted that the temperature slip is significant near the moving lid even when the global Knudsen number is set to a typical continuum value of 0.001. This is because the relaxation times (time to achieve local thermodynamic equilibrium) for the molecules near the wall are too high as they are kept excited by the lid driving at ($M_{lid} = 3$). Moreover, the temperature field approached a steady state with isothermal boundary conditions. Simulations are then performed with adiabatic

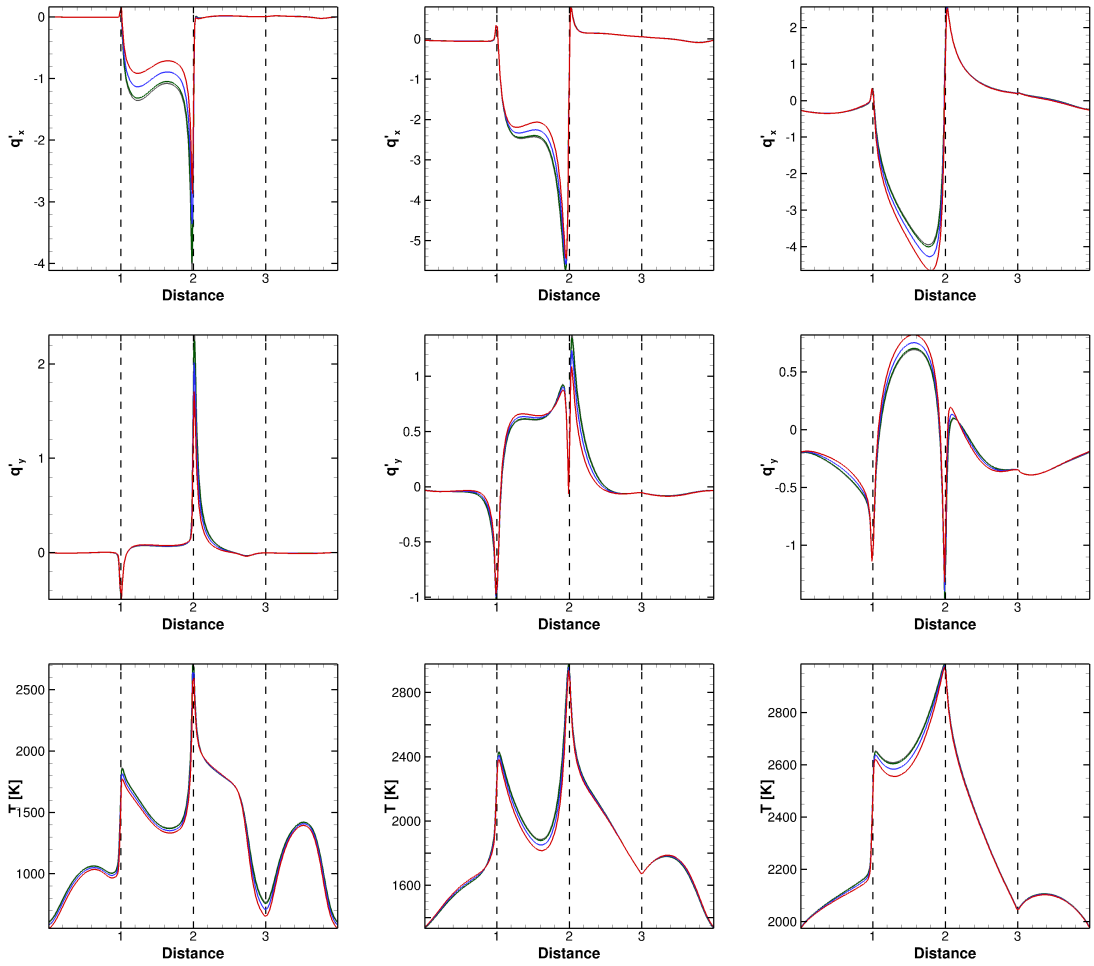


Figure 6.2: Profiles along adiabatic cavity walls at Time = 10 (see Figure 6.1 for legends):
Column$[1-3] = Kn_g[0.001, 0.01, 0.1]$, Row$[1-3] = [|q_x^{'}|, |q_y^{'}|, T]$

walls to investigate the thermal characteristics of the system with $Pr$ variation. This would allow us to determine the actual amount of heat that flows to the cavity walls and the rate at which the wall temperature increases.

Figure 6.2 illustrates the heat flux (non-dimensionalized by $\rho_\infty a_\infty^3$, where $a$ is the speed of sound) and temperature profiles along the insulated cavity walls. Heat flux components along the direction of lid velocity, $q_x^{'}$, is plotted in the first row

of Figure 6.2. The continuum and near-continuum profile near the adiabatic lid confirms that $q_x^{'}$ increases with an increase in $Pr$ and flows in the direction opposite to that of the lid velocity, while $q_x^{'}$ decreases with an increase in $Pr$ for the rarefied case. This should not affect the observed variations in lid temperature profile, as $q_x^{'}$ is directed tangential to the lid surface. However, in the rarefied case, we observe peak $q_x^{'}$ on the downstream wall which contributes to a rise in the wall temperature. $q_y^{'}$, is plotted in the second row of Figure 6.2 and it can be seen that heat flux peaks at the top right corner of the cavity. Overall, in continuum regimes, the heat flux peaks are higher at low $Pr$, and these peaks are less sensitive to changes in $Pr$ in rarefied regimes. But, it should be noted that the average heat flux and hence the temperature (third row of Figure 6.2) along the top lid and the downstream cavity wall show a significant increase with an increase in the degree of rarefaction. Figure 6.3 shows the average lid temperature and average lid heat-flux at different values of $Pr$ and $Kn_g$. The trend shows that the average temperature decreases with an increase in Prandtl number, particularly in the rarefied regime. Also, the average lid heat-flux in rarefied regimes is found to increase with an increase in $Pr$ whose trend is opposite to those at continuum and near-continuum cases.

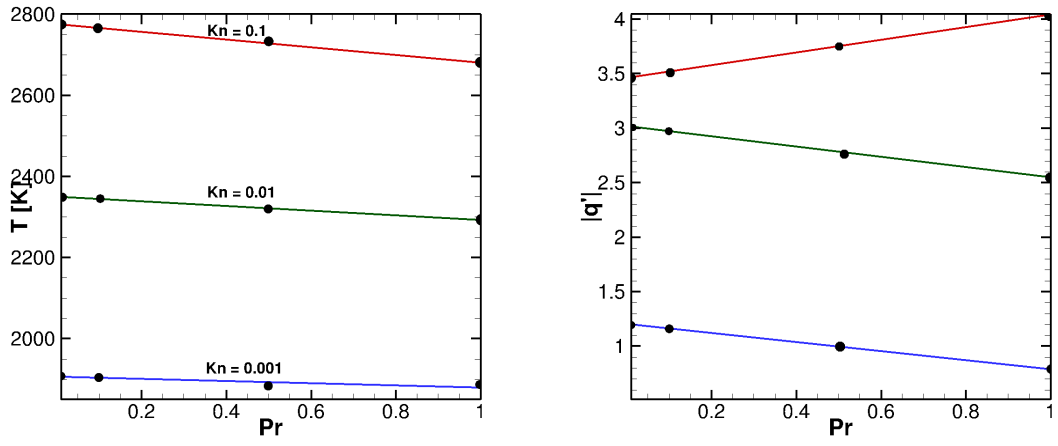


Figure 6.3: Effect of $Pr$ variation on (a) average lid temperature and (b) average lid heat-flux

## 6.3 Conclusion

A parametric study was conducted to analyze the effects of Prandtl number ($Pr$) variation on the thermal transport behavior in the vicinity of cavity walls. 2D UGKS simulations are performed for different global Knudsen numbers for high-speed flows with the lid moving at Mach 3. With isothermal walls, changes in $Pr$ do not affect the thermal profile along the cavity walls at any level of rarefaction. The temperature field approached a steady state with isothermal boundary conditions. The average temperature near the lid decreases with an increase in Prandtl number when the cavity walls are set to be adiabatic. This effect is significant in the rarefied regime. Also, for the adiabatic case, the average lid heat-flux in rarefied regimes is found to increase with an increase in $Pr$, while the average heat-flux near the lid decreases with increasing $Pr$ at lower Knudsen numbers. Further analysis is required to understand the physical mechanisms behind this observation.

# 7. CONCLUDING REMARKS

A novel finite volume gas kinetic numerical scheme is developed from the Unified Gas Kinetic Scheme of Xu and Huang [46] by enhancing the initial distribution flux reconstruction with a WENO (Weighted Essentially Non-Oscillatory) method [39, 49]. The entire phase space is discretized starting from the BGK-Shakhov model [37], which allows us to numerically simulate flows in the whole Knudsen number regime. A comprehensive step-by-step algorithm to this approach is presented in Appendix A.

In Chapter 3, the results from UGKS codes are validated against corresponding DSMC solutions for a wide range of Knudsen numbers spanning from near-continuum/slip regime to rarefied regime. Use of WENO schemes for initial reconstruction of the distribution fluxes gave oscillation-free solutions with higher spacial accuracy as well as faster convergence compared to Van-Leer limiting scheme at high Knudsen numbers.

Further simulations with varying aspect-ratio reveal that the formation of secondary vortices depend on the degree of rarefaction as well as the lid velocity. It is observed that multi-vortex configurations are favorable in high aspect ratio cavities. As the degree of rarefaction is increased, secondary vortices tend to disappear. At the same time, the number of active vortices increase with an increase in the lid velocity. However, with higher lid velocities at highly rarefied regimes, non-physical oscillations appear in the flow domain. Newton-Cotes quadrature with 100 velocity points in each direction along with a $5^{th}$ WENO scheme for flux interpolation is then necessary to obtain a physically meaningful steady-state with UGKS. Full 3-D simulations are needed to further confirm the physical features presented here.

In Chapter 4, the thermal transport behavior is analyzed for cavity flows of different aspect ratios and are characterized as a function of global Knudsen number and lid Mach number. An increase in the flow speed constraints the regions of non-equilibrium to the vicinity of the moving lid. Extended hydrodynamic models like Burnett models could accurately capture the thermal transport in the continuum and near-continuum regime irrespective of the cavity aspect ratio and lid Mach number. In transition and rarefied flows, the extended thermodynamic models efficiently represent the heat transport behavior away from the cavity walls. Augmented Burnett model captures the heat flux vectors better than the BGK-Burnett model in supersonic flow regime. The thermal transport phenomena in cavity flow simulations using Unified Gas Kinetic Scheme do not violate Boltzmann's $H$ theorem and further validates the physical existence of counter-counter-gradient heat transfer. Bolzmann's $H$ theorem is universal and should be invoked to analyze the validity of flow fields accompanied with high non-equilibrium effects.

The vortex structures in rarefied cavity flows are examined in Chapter 5. A highly rarefied lid-driven cavity consists only of a primary vortex driven by the moving lid. The streamlines form a closed loop as a consequence of the molecules colliding solely against the cavity walls. There is not sufficient accumulation of molecules at the corners to initaite formation of corner eddies. Favorable conditions for corner eddy formation are (a) high density of molecule accumulation, (b) high collision frequency and (c) low velocity magnitude. As the degree of rarefaction is decreased, more molecules are accumulated in the DSE/USE regions. Small velocity magnitude and high collision frequency at these regions indicate the formation of a near-stagnant cluster of molecules. These regions then act as independent collection of fluid particles creating a barrier that deflect an oncoming external molecules. The near-stagnant particles start to gain angular momentum from the nearby primary

vortex to form secondary eddies. As the cavity depth is increased, more molecules get entrapped into the DSE/USE regions, allowing the eddies to grow in size. With further increase in the cavity depth, the DSE and USE merge to form a secondary vortex. The process keeps repeating with an increase in the cavity depth, given favorable flow conditions. If the width of the cavity is increased, the USE region grows in size, leading to the formation of a secondary vortex. The shape of the primary vortex distorts leaving behind a narrow extension between the secondary vortex and the 'no-slip' moving lid. Vortex structure classification maps are generated in Kn - Ma parameter space for square, deep and wide cavities. In general, it is observed that the evolution of flow structures in wide cavities are more sensitive to the degree of rarefaction than that for deep cavities.

Chapter 6 includes a parametric study to analyze the effects of Prandtl number ($Pr$) variation on the thermal transport behavior in the vicinity of cavity walls. 2D UGKS simulations are performed for different global Knudsen numbers for high-speed flows with the lid moving at Mach 3. With isothermal walls, changes in $Pr$ do not affect the thermal profile along the cavity walls at any level of rarefaction. The temperature field approached a steady state with isothermal boundary conditions. The average temperature near the lid decreases with an increase in Prandtl number when the cavity walls are set to be adiabatic. This effect is significant in the rarefied regime. Also, for the adiabatic case, the average lid heat-flux in rarefied regimes is found to increase with an increase in $Pr$, while the average heat-flux near the lid decreases with increasing $Pr$ at lower Knudsen numbers. Further analysis is required to understand the physical mechanisms behind this observation.

To summarize, gas kinetic numerical simulations based on a WENO enhanced Unified Gas Kinetic Scheme reproduces well established results in the literature over the entire Knudsen number regime. These high-fidelity simulations prove to capture

relevant physical mechanisms involved in extreme non-equilibrium flows. Parametric studies followed by careful observations and rigorous analyses reveal important insights to the rarefaction effects on the heat and mass transport behavior of canonical 2D cavity flows. The proposed scheme can extensively be used for fluid flows comprising of large density variations whose length scales extend from a macro-scale to a molecular scale. However, 3D UGKS simulations are necessary to investigate real-world problems or even to examine the non-equilibrium due to rarefaction in turbulence dominated flows. It should be noted that such 3D UGKS simulations would require a generous amount of computational memory as the whole six dimensional phase space needs to be discretized. Hence, an adaptive mesh refinement technique in both the physical as well as the velocity space plays a critical role in optimizing the memory consumption of a 3D UGKS solver.

# REFERENCES


[1] Ramesh K Agarwal and Ramesh Balakrishnan. Numerical simulation of bgk-burnett equations. Technical report, DTIC Document, 1996.

[2] Ramesh K Agarwal, Keon-Young Yun, and Ramesh Balakrishnan. Beyond navier–stokes: Burnett equations for flows in the continuum–transition regime. *Physics of Fluids*, 13(10):3061–3085, 2001.

[3] Ramesh Balakrishnan and Ramesh K Agarwal. Entropy consistent formulation and numerical simulation of the bgk-burnett equations using a kinetic wave/particle flux splitting algorithm. In *Fifteenth International Conference on Numerical Methods in Fluid Dynamics*, pages 480–485. Springer, 1997.

[4] Timothy J Bartel, Todd M Sterk, Jeff Payne, and Bryan Preppernau. Dsmc simulation of nozzle expansion flow fields. In *AIAA and ASME, Joint Thermophysics and Heat Transfer Conference, Sixth, Colorado Springs, CO*, 1994.

[5] John J Bertin and Russell M Cummings. Critical hypersonic aerothermodynamic phenomena*. *Annu. Rev. Fluid Mech.*, 38:129–157, 2006.

[6] Prabhu Lal Bhatnagar, Eugene P Gross, and Max Krook. A model for collision processes in gases. i. small amplitude processes in charged and neutral one-component systems. *Physical Review*, 94(3):511, 1954.

[7] Graeme Austin Bird. *Molecular gas dynamics and the direct simulation of gas flows*. Clarendon, 1994.

[8] AV Bobylev. The chapman-enskog and grad methods for solving the boltzmann equation. In *Akademiia Nauk SSSR Doklady*, volume 262, pages 71–75, 1982.

[9] Lars Buitinck, Gilles Louppe, Mathieu Blondel, Fabian Pedregosa, Andreas Mueller, Olivier Grisel, Vlad Niculae, Peter Prettenhofer, Alexandre Gramfort,

Jaques Grobler, Robert Layton, Jake VanderPlas, Arnaud Joly, Brian Holt, and Gaël Varoquaux. API design for machine learning software: experiences from the scikit-learn project. In *ECML PKDD Workshop: Languages for Data Mining and Machine Learning*, pages 108–122, 2013.

[10] D Burnett. The distribution of molecular velocities and the mean motion in a non-uniform gas. *Proceedings of the London Mathematical Society*, 2(1):382–435, 1936.

[11] Henry A Carlson, Roberto Roveda, Iain D Boyd, and Graham V Candler. A hybrid cfd-dsmc method of modeling continuum-rarefied flows. *AIAA paper*, 1180:2004, 2004.

[12] Wang Chang and George Eugène Uhlenbeck. On the transport phenomena in rarified gases. Technical report, DTIC Document, 1948.

[13] Sydney Chapman and Thomas George Cowling. *The mathematical theory of non-uniform gases: an account of the kinetic theory of viscosity, thermal conduction and diffusion in gases*. Cambridge University Press, 1970.

[14] Gang Chen. Ballistic-diffusive heat-conduction equations. *Physical Review Letters*, 86(11):2297, 2001.

[15] Shyan-Yih Chou and Donald Baganoff. Kinetic flux–vector splitting for the navier–stokes equations. *Journal of Computational Physics*, 130(2):217–230, 1997.

[16] C. K. Chu. Kinetic-Theoretic Description of the Formation of a Shock Wave. *Physics of Fluids*, 8(1):12, 1965.

[17] Keith A Comeaux, Dean R Chapman, and Robert W MacCormack. An analysis of the burnett equations based on the second law of thermodynamics. In $33^{rd}$ *AIAA Aerospace Sciences Meeting and Exhibit, Reno, NV*, 1995.

[18] Zhaoli Guo, Kun Xu, and Ruijie Wang. Discrete unified gas kinetic scheme for

all knudsen number flows: Low-speed isothermal case. *Physical Review E*, 88 (3):033305, 2013.

[19] Juan-Chen Huang, Kun Xu, and Pubing Yu. A unified gas-kinetic scheme for continuum and rarefied flows ii: multi-dimensional cases. *Commun. Comput. Phys*, 3(3):662–690, 2012.

[20] Juan-Chen Huang, Kun Xu, and Pubing Yu. A unified gas-kinetic scheme for continuum and rarefied flows iii: Microflow simulations. *Commun. Comput. Phys*, 14(5):1147–1173, 2013.

[21] Shi Jin and Marshall Slemrod. Regularization of the burnett equations via relaxation. *Journal of Statistical Physics*, 103(5-6):1009–1033, 2001.

[22] Hiroshi Kawamura, Hiroyuki Abe, and Yuichi Matsuo. Dns of turbulent heat transfer in channel flow with respect to reynolds and prandtl number effects. *International Journal of Heat and Fluid Flow*, 20(3):196–207, 1999.

[23] Johannes Kerimo and Sharath S Girimaji. Boltzmann–bgk approach to simulating weakly compressible 3d turbulence: comparison between lattice boltzmann and gas kinetic methods. *Journal of Turbulence*, (8):N46, 2007.

[24] G Kumar, Sharath S Girimaji, and J Kerimo. Weno-enhanced gas-kinetic scheme for direct simulations of compressible transition and turbulence. *Journal of Computational Physics*, 234:499–523, 2013.

[25] Georgy Lebon, Hatim Machrafi, M Grmela, and Ch Dubois. An extended thermodynamic model of transient heat conduction at sub-continuum scales. In *Proceedings of the Royal Society of London A: Mathematical, Physical and Engineering Sciences*, volume 467, pages 3241–3256. The Royal Society, 2011.

[26] Wing Yin Lee, Man Wong, and Yitshak Zohar. Pressure loss in constriction microchannels. *Journal of Microelectromechanical Systems*, 11(3):236–244, 2002.

[27] Elmer Eugene Lewis and Warren F Miller. *Computational methods of neutron*

*transport*. John Wiley and Sons, Inc., New York, NY, 1984.

[28] JC Mandal and SM Deshpande. Kinetic flux vector splitting for euler equations. *Computers & Fluids*, 23(2):447–478, 1994.

[29] Alireza Mohammadzadeh, Ehsan Roohi, Hamid Niazmand, Stefan Stefanov, and Rho Shin Myong. Thermal and second-law analysis of a micro-or nanocavity using direct-simulation monte carlo. *Physical Review E*, 85(5):056310, 2012.

[30] Yang Na, Dimitrios V Papavassiliou, and Thomas J Hanratty. Use of direct numerical simulation to study the effect of prandtl number on temperature fields. *International Journal of Heat and Fluid Flow*, 20(3):187–195, 1999.

[31] Stergios Naris and Dimitris Valougeorgis. The driven cavity flow over the whole range of the knudsen number. *Physics of Fluids*, 17(9):097106, 2005.

[32] S Pantazis and H Rusche. A hybrid continuum-particle solver for unsteady rarefied gas flows. *Vacuum*, 109:275–283, 2014.

[33] F. Pedregosa, G. Varoquaux, A. Gramfort, V. Michel, B. Thirion, O. Grisel, M. Blondel, P. Prettenhofer, R. Weiss, V. Dubourg, J. Vanderplas, A. Passos, D. Cournapeau, M. Brucher, M. Perrot, and E. Duchesnay. Scikit-learn: Machine learning in Python. *Journal of Machine Learning Research*, 12:2825–2830, 2011.

[34] Kin-Choek Pong, Chih-Ming Ho, Jianqiang Liu, and Yu-Chong Tai. Non-linear pressure distribution in uniform microchannels. *ASME-Publications-Fed*, 197: 51–51, 1994.

[35] Kevin H Prendergast and Kun Xu. Numerical hydrodynamics from gas-kinetic theory. *Journal of Computational Physics*, 109(1):53–66, 1993.

[36] L Redjem-Saad, M Ould-Rouiss, and G Lauriat. Direct numerical simulation of turbulent heat transfer in pipe flows: Effect of prandtl number. *International Journal of Heat and Fluid Flow*, 28(5):847–861, 2007.

[37] EM Shakhov. Generalization of the krook kinetic relaxation equation. *Fluid Dynamics*, 3(5):95–96, 1968.

[38] B Shizgal. A gaussian quadrature procedure for use in the solution of the boltzmann equation and related problems. *Journal of Computational Physics*, 41(2): 309–328, 1981.

[39] Chi-Wang Shu. *Essentially non-oscillatory and weighted essentially non-oscillatory schemes for hyperbolic conservation laws*. Springer, 1998.

[40] M Torrilhon and Henning Struchtrup. Regularized 13-moment equations: shock structure calculations and comparison to burnett models. *Journal of Fluid Mechanics*, 513:171–198, 2004.

[41] Bram Van Leer. Towards the ultimate conservative difference scheme. v. a second-order sequel to godunov's method. *Journal of Computational Physics*, 32(1):101–136, 1979.

[42] Stelios Varoutis, Dimitris Valougeorgis, and Felix Sharipov. Application of the integro-moment method to steady-state two-dimensional rarefied gas flows subject to boundary induced discontinuities. *Journal of Computational Physics*, 227(12):6272–6287, 2008.

[43] Vishnu Venugopal and Sharath S Girimaji. Unified gas kinetic scheme and direct simulation monte carlo computations of high-speed lid-driven microcavity flows. *Communications in Computational Physics*, 17(05):1127–1150, 2015.

[44] Zhihui Wang, Lin Bao, and Binggang Tong. Rarefaction criterion and non-fourier heat transfer in hypersonic rarefied flows. *Physics of Fluids*, 22(12): 126103, 2010.

[45] Kun Xu. A gas-kinetic bgk scheme for the navier–stokes equations and its connection with artificial dissipation and godunov method. *Journal of Computational Physics*, 171(1):289–335, 2001.

[46] Kun Xu and Juan-Chen Huang. A unified gas-kinetic scheme for continuum and rarefied flows. *Journal of Computational Physics*, 229(20):7747–7764, 2010.

[47] Kun Xu and Juan-Chen Huang. An improved unified gas-kinetic scheme and the study of shock structures. *IMA Journal of Applied Mathematics*, 76(5):698–711, 2011.

[48] Kun Xu, Meiliang Mao, and Lei Tang. A multidimensional gas-kinetic BGK scheme for hypersonic viscous flow. *Journal of Computational Physics*, 203(2): 405–421, 2005.

[49] Nail K Yamaleev and Mark H Carpenter. High-order energy stable weno schemes. In $47^{th}$ *AIAA Aerospace Sciences Meeting including the New Horizons Forum and Aerospace Exposition*, 2009.

[50] J.Y. Yang and J.C. Huang. Rarefied flow computations using nonlinear model boltzmann equations. *Journal of Computational Physics*, 120(2):323 – 339, 1995.

[51] Keon-Young Yun, Ramesh K Agarwal, Ramesh Balakrishnan, Keon-Young Yun, Ramesh Agarwal, and Ramesh Balakrishnan. A comparative study of augmented burnett and bgk-burnett equations for computing hypersonic blunt body flows. In $35^{th}$ *AIAA Aerospace Sciences Meeting & Exhibit, Reno, NV*, 1997.

[52] Xiaolin Zhong. *Development and computation of continuum higher order constitutive relations for high-altitude hypersonic flow.* Stanford University, 1991.

# APPENDIX A

# ALGORITHM - UNIFIED GAS KINETIC SCHEME

This chapter describes the algorithm for a finite volume Unified Gas-Kinetic Scheme presented in Xu and Huang [46, 47] enhanced with a WENO (Weighted Essentially Non-Oscillatory) techniques of Shu [39], Yamaleev and Carpenter [49] for initial distribution flux reconstruction. A one-dimensional formulation and its algorithm is discussed. The algorithm can easily be extended to two/three-dimensional program using a directional splitting approach [19, 48]. The important alterations required in the algorithm when implementing a two dimensional problem are discussed in section A.8.

## A.1 Model Equation

The model equation is the BGK-Shakhov model [37]. In one dimensional case the model equation can be written as,

$$\frac{\partial f}{\partial t} + u\frac{\partial f}{\partial x} = \frac{f^+ - f}{\tau}, \tag{A.1}$$

where $f$ is the single particle distribution function, $u$ is particle velocity, $\tau = \mu/p$ is particle collision time, $\mu$ is the dynamic viscosity coefficient, $p$ is the pressure and $f^+$ is the modified equilibrium distribution function.

The modified equilibrium distribution is given by,

$$f^+ = g\left[1 + (1 - \mathrm{Pr})\mathbf{c}\cdot\mathbf{q}\left(\frac{c^2}{RT} - 5\right)/(5pRT)\right] = g + g^+, \tag{A.2}$$

where $g$ is the equilibrium Maxwellian distribution, Pr is the Prandtl number, $\mathbf{c}$ is

the random (or thermal or peculiar) velocity, $\mathbf{q}$ is heat flux, $R$ is gas constant and $T$ is the temperature.

The Maxwellian distribution for 1D problem is,

$$g = \rho \left(\frac{\lambda}{\pi}\right)^{\frac{K+1}{2}} e^{-\lambda((u-U)^2+\xi^2)}, \tag{A.3}$$

where $\rho$ is density, $\lambda = m/2kT$, $m$ is molecule mass, $k$ is Boltzmann constant, $U$ is the macroscopic velocity, $K$ is the number of internal degree of freedom and $\xi^2 = \xi_1^2 + \xi_2^2 ... + \xi_K^2$, a measure of the total energy contained in other excited internal modes. For example, a monatomic gas at 1D problem has $K = 2$ to account for the motion in $y, z$ direction, and $\xi^2 = v^2 + w^2$, where $v, w$ are particle velocity in $y, z$ direction.

The relation between $K$ and the ratio of specific heat is,

$$\gamma = \frac{K+3}{K+1}. \tag{A.4}$$

The dynamic viscosity coefficient can be calculated from Sutherland's law with the viscosity-temperature index calculated from a hard-sphere(HS)/variable hard-sphere collision model(VHS):

$$\mu = \mu_{ref} \left(\frac{T}{T_{ref}}\right)^{\omega}, \tag{A.5}$$

where $\mu_{ref}$ is the reference viscosity coefficient at the reference temperature, $T_{ref}$ and $\omega$ is the viscosity-temperature index whose value depends on the collision model we choose.

The collision term meets the requirement of 'conservative constraint' or 'compat-

ibility condition':

$$\int (f^+ - f)\psi d\Xi = 0, \tag{A.6}$$

where $\psi = (1, u, 1/2(u^2+\xi^2))^T$ is called the collision invariant matrix and $d\Xi = dud\xi$.

The macroscopic variables ($W$) can be computed via,

$$W = \begin{pmatrix} \rho \\ \rho U \\ \rho E \end{pmatrix} = \int \psi f d\Xi, \tag{A.7}$$

$$p = \frac{1}{3}\int [(u-U)^2 + \xi^2] f d\Xi, \tag{A.8}$$

$$q = \frac{1}{2}\int (u-U)[(u-U)^2 + \xi^2] f d\Xi, \tag{A.9}$$

where $\rho E$ is total energy.

An integral solution of the BGK-Shakhov model can be constructed by the method of characteristics [35],

$$f(x,t,u,\xi) = \frac{1}{\tau}\int_{t^n}^{t} f^+(x',t',u,\xi) e^{-(t-t')/\tau} dt' + e^{-(t-t^n)/\tau} f_0^n(x - u(t-t^n), t^n, u, \xi), \tag{A.10}$$

where $x' = x - u(t-t')$ is the particle trajectory and $f_0^n$ is the initial gas distribution function at $t^n$.

## A.2 Solution Algorithm

For the numerical computation, in addition to the discretization of physical space and time, the velocity space is also discretized. That is, the distribution function is for some discrete particle velocities instead of continuous velocity space from $-\infty$ to $\infty$ as in Xu [45]. Then the moments of the non-equilibrium distribution function are

calculated through numerical integration (the moments of equilibrium distribution are still calculated using analytical integration). The discretization of the velocity space is determined by the choice of numerical integration method.

In the finite volume approach, if trapezoidal rule is invoked for the approximation of collision term, Eq. A.1 becomes,

$$f_{i,k}^{n+1} = f_{i,k}^{n} + \frac{1}{\Delta x}\int_{t^n}^{t^{n+1}} (\mathbf{f}_{i-1/2} - \mathbf{f}_{i+1/2})dt + \frac{\Delta t}{2}\left(\frac{f_{i,k}^{+(n+1)} - f_{i,k}^{n+1}}{\tau^{n+1}} + \frac{f_{i,k}^{+(n)} - f_{i,k}^{n}}{\tau^{n}}\right), \tag{A.11}$$

where $f_{i,k}^{n}$ and $f_{i,k}^{n+1}$ are cell averaged distribution function of the i-th cell and k-th discrete particle velocity $u_k$ at time $t^n$ and $t^{n+1}$ respectively, $\Delta x$ is the cell length and $\Delta t$ is the time step, $\mathbf{f}_{i-1/2}$ and $\mathbf{f}_{i+1/2}$ are the fluxes of the distribution function across the cell interface, $f_{i,k}^{+(n)}$ and $f_{i,k}^{+(n+1)}$ are modified equilibrium distributions, $\tau^n$ and $\tau^{n+1}$ are particle collision times at $n^{th}$ and $(n+1)^t h$ time interval respectively.

Multiplying the collision invariants to Eq. A.11 and then integrating over the velocity space, the evolution equation of the conservative variables transforms to,

$$W_i^{n+1} = W_i^n + \frac{1}{\Delta x}(\mathbf{F}_{i-1/2} - \mathbf{F}_{i+1/2}), \tag{A.12}$$

where $\mathbf{F} = \int_{t^n}^{t^{n+1}} \int \psi \mathbf{f} d\Xi dt$.

In order to update the distribution function in Eq. A.11, there are three unknowns to be obtained: the interface gas distribution function $f$, the modified equilibrium distribution $f^{+(n+1)}$ and collision time $\tau^{n+1}$ at the next time level.

The flux $\mathbf{f}$ is calculated using the integral solution Eq. A.10 at the cell interface. Since $f^{+(n+1)}$ and $\tau^{n+1}$ have one-to-one correspondence to the macroscopic variables, they are obtained by using the updated conservative variables in Eq. A.12.

In order to remove the dependency of the distribution functions on the other

excited internal degrees of freedom $\xi$, the reduced distribution function [50, 16] is used in real computation, which can be defined as,

$$h = \int_{-\infty}^{\infty} f d\xi, \quad b = \int_{-\infty}^{\infty} \xi^2 f d\xi, \tag{A.13}$$

and the corresponding reduced modified equilibrium distributions are,

$$h^+ = H + H^+, \quad b^+ = B + B^+.$$

The corresponding reduced Maxwellian distribution $g$ then becomes,

$$H = \int_{-\infty}^{\infty} g d\xi = \rho \left(\frac{\lambda}{\pi}\right)^{1/2} e^{-\lambda(u-U)^2}, \quad B = \int_{-\infty}^{\infty} \xi^2 g d\xi = \frac{K}{2\lambda} H, \tag{A.14}$$

and where the respective terms related to $g^+$ can be computed as,

$$\begin{aligned} H^+ &= \int_{-\infty}^{\infty} g^+ d\xi = \frac{4(1-\mathrm{Pr})\lambda^2}{5\rho}(u-U)q(2\lambda(u-U)^2 + K - 5)H, \\ B^+ &= \int_{-\infty}^{\infty} \xi^2 g^+ d\xi = \frac{4(1-\mathrm{Pr})\lambda^2}{5\rho}(u-U)q(2\lambda(u-U)^2 + K - 3)B. \end{aligned} \tag{A.15}$$

Thus, the update of $f$ using Eq. A.11 transforms to the update of two similar equations for $h$ and $b$, respectively.

The overview flow chart of the solution algorithm in one iteration is shown in Figure A.1.

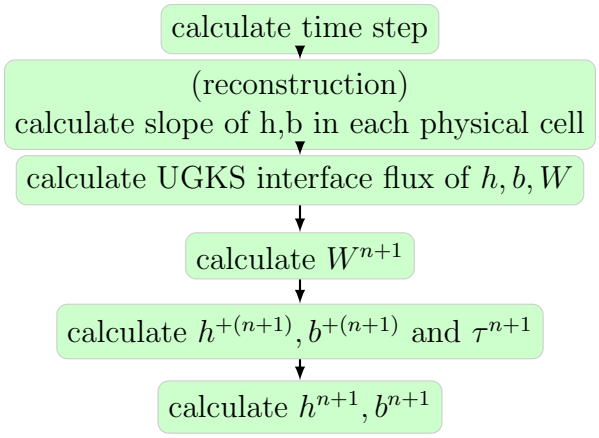


Figure A.1: Solution algorithm in one iteration

## A.3 Non-Dimensionalization

In the UGKS program, the following non-dimensionalizations are used,

$$\hat{t} = \frac{t}{t_\infty},\ \hat{u}_x = \frac{u_x}{C_\infty},\ \hat{x} = \frac{x}{L_\infty},\ \hat{\rho} = \frac{\rho}{\rho_\infty},\ \hat{T} = \frac{T}{T_\infty}, \hat{p} = \frac{p}{\rho_\infty C_\infty^2},$$
$$\hat{q} = \frac{q}{\rho_\infty C_\infty^3},\ \hat{h} = \frac{h}{\rho_\infty / C_\infty},\ \hat{b} = \frac{b}{\rho_\infty C_\infty},\ \hat{E} = \frac{E}{C_\infty^2}, \hat{\mu} = \frac{\mu}{\rho_\infty C_\infty L_\infty},$$

The freestream variables are related through,

$$C_\infty = \sqrt{2RT_\infty},\ t_\infty = \frac{L_\infty}{C_\infty},\ \lambda_\infty = 1/C_\infty^2.$$

In the following equation sets, all variables are non-dimensionalized, but we will drop the '$\hat{}$' for simplicity. Substituting reduced distribution functions, the expres-

sions for macroscopic variables can be written as,

$$\begin{aligned}
\rho &= \int h\mathrm{du} = \sum \alpha_k h_k, \\
\rho U &= \int hu\mathrm{du} = \sum \alpha_k h_k u_k, \\
\rho E &= \frac{1}{2}\left(\int hu^2\mathrm{du} + \int b\mathrm{du}\right) = \frac{1}{2}\left(\sum \alpha_k h_k u_k^2 + \sum \alpha_k b_k\right),
\end{aligned} \tag{A.16}$$

$$(K+1)p = \int (u-U)^2 h\mathrm{du} + \int b\mathrm{du} = \sum \alpha_k (u_k - U)^2 h_k + \sum \alpha_k b_k, \tag{A.17}$$

$$\begin{aligned}
q &= \frac{1}{2}\left[\int (u-U)(u-U)^2 h\mathrm{du} + \int (u-U) b\mathrm{du}\right] \\
&= \frac{1}{2}\left[\sum \alpha_k (u_k - U)(u_k - U)^2 h_k + \sum \alpha_k (u_k - U) b_k\right],
\end{aligned} \tag{A.18}$$

where $\alpha_k$ is the weight of the numerical integration at the k-th particle velocity. The summation is over all the discrete particle velocities.

The equation of state after non-dimensionalization is,

$$p = \frac{1}{2}\rho T, \quad \lambda = \frac{1}{T}. \tag{A.19}$$

## A.4 Time Step and Reconstruction

The time step is determined by the Courant-Friedrichs-Lewy condition

$$\Delta t = \mathrm{CFL}\frac{\Delta x}{|U| + c}, \tag{A.20}$$

where CFL is the Courant-Friedrichs-Lewy number, $c$ is the speed of sound. The macroscopic velocity $|U| + c$ can also be replaced by $\max(|u|)$.

In the program, the Van-Leer limiter and variants of WENO are used for the reconstruction. In the case with Van-Leer non-linear limiter, the slope of $h$ at the

i-th cell and k-th particle velocity is,

$$\sigma_{i,k}^{h} = (\text{sign}(s_1) + \text{sign}(s_2)) \frac{|s_1||s_2|}{|s_1| + |s_2|}, \tag{A.21}$$

where $s_1 = (h_{i,k} - h_{i-1,k})/(x_i - x_{i-1})$, $s_2 = (h_{i+1,k} - h_{i,k})/(x_{i+1} - x_i)$.

The slope of $b$ is calculated in the same way. WENO schemes directly computes the flux at the cell interfaces. The WENO-C scheme is presented first and WENO-S can be derived from WENO-C with minor simplifications. WENO-C calculates the numerical flux (flux of $h$ and $b$ in our case) at the interface ($x_{i+\frac{1}{2}}$) as a convex combination of four $3^{rd}$ order fluxes that are calculated based on the following three point stencils: $S^{(1)} = \{x_{i-2}, x_{i-1}, x_i\}$, $S^{(2)} = \{x_{i-1}, x_i, x_{i+1}\}$, $S^{(3)} = \{x_i, x_{i+1}, x_{i+2}\}$ and $S^{(4)} = \{x_{i+1}, x_{i+2}, x_{i+3}\}$. Note that the collection of all four stencils is symmetric with respect to $x_{i+\frac{1}{2}}$. The WENO-C flux of any quantity $q$ is then given by

$$q_{i+\frac{1}{2}} = w^{(1)} q_{i+\frac{1}{2}}^{(1)} + w^{(2)} q_{i+\frac{1}{2}}^{(2)} + w^{(3)} q_{i+\frac{1}{2}}^{(3)} + w^{(4)} q_{i+\frac{1}{2}}^{(4)} \tag{A.22}$$

where $q_{i+\frac{1}{2}}^{(r)}$ is the $3^{rd}$ order flux defined by the stencil $S^{(r)}$ $(r = 1, 2, 3, 4)$

$$\begin{pmatrix} q_{i+\frac{1}{2}}^{(1)} \\ q_{i+\frac{1}{2}}^{(2)} \\ q_{i+\frac{1}{2}}^{(3)} \\ q_{i+\frac{1}{2}}^{(4)} \end{pmatrix} = \frac{1}{6} \begin{pmatrix} 2 & -7 & 11 & 0 & 0 & 0 \\ 0 & -1 & 5 & 2 & 0 & 0 \\ 0 & 0 & 2 & 5 & -1 & 0 \\ 0 & 0 & 0 & 11 & -7 & 2 \end{pmatrix} \begin{pmatrix} q_{i-2} \\ q_{i-1} \\ q_i \\ q_{i+1} \\ q_{i+2} \\ q_{i+3} \end{pmatrix} \tag{A.23}$$

and the weight function is given by

$$w^{(r)} = \frac{b^{(r)}}{\sum_{m=1}^{4} b^{(r)}}, \tag{A.24}$$

$$b^{(r)} = d^{(r)} \left(1 + \frac{p}{\epsilon + \beta^{(r)}}\right), \quad \epsilon = 10^{-6}, \tag{A.25}$$

$$d^{(1)} = \frac{1}{10} - \Delta, \quad d^{(2)} = \frac{6}{10} - 3\Delta, \quad d^{(3)} = \frac{3}{10} + 3\Delta, \quad d^{(4)} = \Delta. \tag{A.26}$$

The functions $\beta^{(r)}$ are the smoothness indicators and are given by

$$\beta^{(1)} = \frac{13}{12}\left(q_{i-2} - 2q_{i-1} + q_i\right)^2 \quad + \quad \frac{1}{4}\left(q_{i-2} - 4q_{i-1} + 3q_i\right)^2 \tag{A.27a}$$

$$\beta^{(2)} = \frac{13}{12}\left(q_{i-1} - 2q_i + q_{i+1}\right)^2 \quad + \quad \frac{1}{4}\left(q_{i-1} - q_{i+1}\right)^2 \tag{A.27b}$$

$$\beta^{(3)} = \frac{13}{12}\left(q_i - 2q_{i+1} + q_{i+2}\right)^2 \quad + \quad \frac{1}{4}\left(3q_i - 4q_{i+1} + 3q_{i+2}\right)^2 \tag{A.27c}$$

$$\beta^{(4)} = \frac{13}{12}\left(q_{i+1} - 2q_{i+2} + q_{i+3}\right)^2 + \quad \frac{1}{4}\left(-5q_{i+1} + 8q_{i+2} - 3q_{i+3}\right)^2 \tag{A.27d}$$

and the expression for $p$ is given by

$$p = \begin{cases} \left(-q_{i-2} + 5q_{i-1} - 10q_i + 10q_{i+1} - 5q_{i+2} + q_{i+3}\right)^2 & for \quad \Delta \neq 0 \\ \left(q_{i-2} - 4q_{i-1} + 6q_i - 4q_{i+1} + q_{i+2}\right)^2 & for \quad \Delta = 0 \end{cases} \tag{A.28}$$

The value of $\Delta$ affects the convergence rate and for the specific value of $\Delta_c = \frac{1}{20}$, the convergence rate is 6 [49]. Hence, all WENO-C simulations will be performed with $\Delta = \frac{1}{20}$. It can be proved that the classical fifth-order upwind-biased WENO-S scheme of Shu [39] is obtained by setting $\Delta = 0$. It should be noted that the WENO reconstruction to the left interface to obtain $q_{i-\frac{1}{2}}$ is mirror symmetric with respect to $x_i$ of the above procedure [39].

The flux of the initial distribution function at the cell interface at $x_{i+1/2}$ is selected

based on the direction of the particle velocity in the corresponding velocity space $u_k$:

$$q_{i+1/2,k} = \begin{cases} q_{i+1/2,k}^{(left)} & if \quad u_k \geq 0 \\ \\ q_{i+1/2,k}^{(right)} & if \quad u_k < 0 \end{cases} \tag{A.29}$$

The WENO based slope ($\sigma_{i,k} = (q_{i+1/2,k}^{(left)} - q_{i-1/2,k}^{(right)})/(x_{i+1/2} - x_{i-1/2})$) is also computed and stored in order to substitute into further computations.

## A.5 UGKS Flux Computation

Consider the cell interface $x_{i+1/2} = 0$ at $t^n = 0$.

### *A.5.1 Calculation of Interface Fluxes*

Here the original distribution function is used for illustration. From Eq. A.10, the integral solution at the cell interface is,

$$f(0, t, u_k, \xi) = \frac{1}{\tau} \int_0^t f^+(x', t', u_k, \xi) e^{-(t-t')/\tau} dt' + e^{-t/\tau} f_0(-u_k t, 0, u_k, \xi). \tag{A.30}$$

The initial distribution function around the interface $f_0$ is,

$$f_0(x, 0, u_k, \xi) = \begin{cases} f_{i+1/2,k}^L + \sigma_{i,k} x, & x \leqslant 0, \\ f_{i+1/2,k}^R + \sigma_{i+1,k} x, & x > 0, \end{cases} \tag{A.31}$$

where $f_{i+1/2,k}^L, f_{i+1/2,k}^R$ are the reconstructed initial distribution functions at the left and right side of the interface.

The Maxwellian distribution around the interface in $f^+$ is approximated by Taylor expansion,

$$g(x, t, u, \xi) = g_0[1 + (1 - H[x])a^L x + H[x]a^R x + At], \tag{A.32}$$

where $g_0$ is the Maxwellian distribution at $x = 0, t = 0$ and $H[x]$ is the Heaviside function

$$H[x] = \begin{cases} 0, & x < 0, \\ 1, & x \geqslant 0. \end{cases}$$

$a^L, a^R$ and $A$ have the same form [45],

$$a = a_1 + a_2 u + a_3 \frac{1}{2}(u^2 + \xi^2),$$

where $a_1, a_2, a_3$ are local constants.

Inserting Eq. A.31 and Eq. A.32 into Eq. A.30, one obtains,

$$\begin{aligned} f(0,t,u_k,\xi) =& (1 - e^{-t/\tau})(g_0 + g^+) \\ &+ (\tau(-1 + e^{-t/\tau}) + te^{-t/\tau})(a^L H[u_k] + a^R(1 - H[u_k]))u_k g_0 \\ &+ \tau(t/\tau - 1 + e^{-t/\tau})Ag_0 \\ &+ e^{-t/\tau}((f^L_{i+1/2,k} - u_k t\sigma_{i,k})H[u_k] + (f^R_{i+1/2,k} - u_k t\sigma_{i+1,k})(1 - H[u_k])) \\ =& \tilde{g}_{i+1/2,k} + \tilde{f}_{i+1/2,k}, \end{aligned} \tag{A.33}$$

where $\tilde{g}_{i+1/2,k}$ is the first three terms related to equilibrium distribution, $\tilde{f}_{i+1/2,k}$ is the last term related to the initial non-equilibrium distribution.

Here $g_0$ or $W_0$ in Eq. A.32 can be obtained by applying the compatibility condition at $x = 0, t = 0$,

$$\int (f^+ - f)|_{x=0,t=0} \psi d\Xi = 0,$$

which gives,

$$W_0 = \int g_0 \psi d\Xi = \int f_0(0,0,u_k,\xi)\psi d\Xi. \tag{A.34}$$

We then, compute the variables $a^L, a^R, A$ which are obtained from the mathe-

matical definitions for the slope of conservative variables,

$$\left(\frac{\partial W}{\partial x}\right)^L = \int a^L g_0 \psi d\Xi, \quad \left(\frac{\partial W}{\partial x}\right)^R = \int a^R g_0 \psi d\Xi, \tag{A.35}$$

$$\frac{\partial W}{\partial t} = \int A g_0 \psi d\Xi. \tag{A.36}$$

The time derivative of $W$ can be calculated via the compatibility condition,

$$\frac{\mathrm{d}}{\mathrm{d}t} \int (f^+ - f)\psi d\Xi \Big|_{x=0,t=0} = 0,$$

which gives,

$$\frac{\partial W}{\partial t} = -\int \left(a^L H[u] + a^R (1 - H[u])\right) u g_0 \psi d\Xi. \tag{A.37}$$

### *A.5.2 Numerical Procedure*

The flow chart of the numerical procedure is shown in Figure A.2.

*Reconstruct initial distribution*

Take $h$ as example. Since we take value from $h^L_{i+1/2,k}$ only if $u_k \geqslant 0$ and take value from $h^R_{i+1/2,k}$ only if $u_k < 0$ (see Eq. A.33), there is no need to store the left and right values separately.

We define the variable,

$$h_{i+1/2,k} = \begin{cases} h_{i,k} + (x_{i+1/2} - x_i)\sigma^h_{i,k}, & u_k \geqslant 0, \\ h_{i+1,k} - (x_{i+1} - x_{i+1/2})\sigma^h_{i+1,k}, & u_k < 0, \end{cases}$$

and similarly,

$$\sigma^h_{i+1/2,k} = \begin{cases} \sigma^h_{i,k}, & u_k \geqslant 0, \\ \sigma^h_{i+1,k}, & u_k < 0. \end{cases}$$

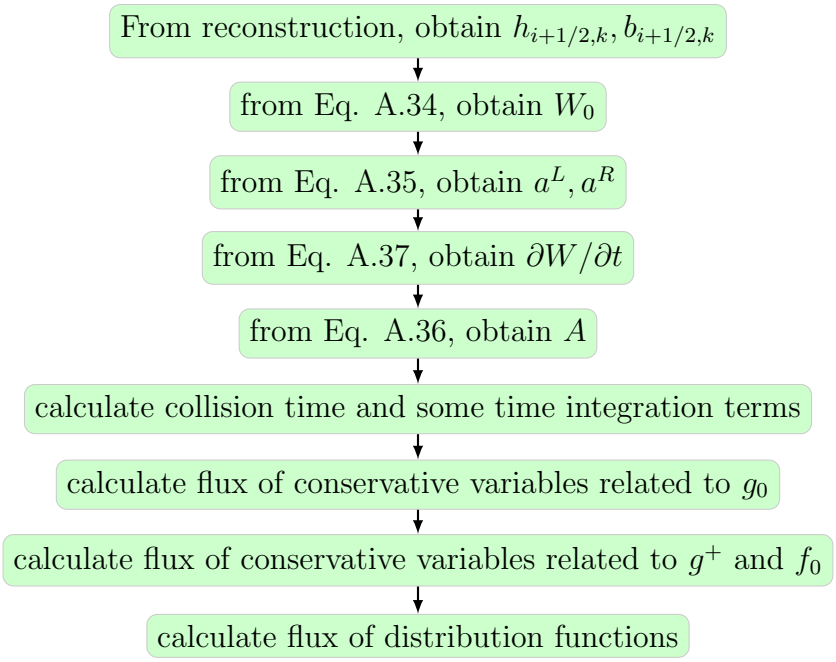


Figure A.2: UGKS interface flux calculation

In the program, they are written as,

$$\sigma^h_{i+1/2,k} = \sigma^h_{i,k} H[u_k] + \sigma^h_{i+1,k}(1 - H[u_k]),$$

and,

$$h_{i+1/2,k} = (h_{i,k} + (x_{i+1/2} - x_i)\sigma^h_{i,k})H[u_k] + (h_{i+1,k} - (x_{i+1} - x_{i+1/2})\sigma^h_{i+1,k})(1 - H[u_k]).$$

*Calculate* $W_0$

$W_0$ is calculated from Eq. A.16, with $h_k = h_{i+1/2,k}, b_k = b_{i+1/2,k}$.

Then the primary variables are obtained from the relation (the expression for $\lambda$

below only holds for equilibrium state),

$$\rho_0 = \rho_0, \quad U_0 = \frac{\rho_0 U_0}{\rho_0}, \quad \lambda_0 = \frac{(K+1)\rho_0}{4\left(\rho_0 E_0 - \frac{1}{2}\rho U_0^2\right)}.$$

The heat flux is calculated by Eq. A.18, with $h_k = h_{i+1/2,k}, b_k = b_{i+1/2,k}, U = U_0$.

*Calculate* $a^L, a^R$

The macroscopic slope is approximated by,

$$\left(\frac{\partial W}{\partial x}\right)^L \approx \frac{W_0 - W_i}{x_{i+1/2} - x_i}, \quad \left(\frac{\partial W}{\partial x}\right)^R \approx \frac{W_{i+1} - W_0}{x_{i+1} - x_{i+1/2}},$$

and the three components of $a^L, a^R$ are calculated from,

$$\begin{aligned} a_3 &= \frac{4\lambda_0^2}{(K+1)\rho_0}\left[2\frac{\partial \rho E}{\partial x} + \left(U_0^2 - \frac{K+1}{2\lambda_0}\right)\frac{\partial \rho}{\partial x} - 2U_0\frac{\partial \rho U}{\partial x}\right], \\ a_2 &= \frac{2\lambda_0}{\rho_0}\left(\frac{\partial \rho U}{\partial x} - U_0\frac{\partial \rho}{\partial x}\right) - U_0 a_3, \\ a_1 &= \frac{1}{\rho_0}\frac{\partial \rho}{\partial x} - U_0 a_2 - \frac{1}{2}\left(U_0^2 + \frac{K+1}{2\lambda_0}\right)a_3. \end{aligned} \tag{A.38}$$

*Calculate* $\partial W/\partial t$ *and* $A$

From Eq. A.37, the time derivative of $W$ is calculated from,

$$\frac{\partial W}{\partial t} = -\rho_0\left(< a^L u\psi >_{>0} + < a^R u\psi >_{<0}\right),$$

where $< ... >$ is the moments of Maxwellian distribution function. The detail definition and calculation can be found in [45] and also in section A.9.

$A$ is calculated in the same way as $a^L, a^R$ using Eq. A.38.

*Calculate collision time and some time integration terms*

From Eq. A.5 and Eq. A.19, the collision time is,

$$\tau = \frac{2\lambda_0^{1-\omega}}{\rho_0}\mu_\infty.$$

Some time integrals used in the evaluation of flux are listed below,

$$\begin{aligned}
Mt_4 &= \int_{t^n}^{t^{n+1}} e^{-t/\tau}dt = \tau(1-e^{-\Delta t/\tau}),\\
Mt_5 &= \int_{t^n}^{t^{n+1}} te^{-t/\tau}dt = -\tau\Delta te^{-\Delta t/\tau} + \tau Mt_4,\\
Mt_1 &= \int_{t^n}^{t^{n+1}} (1-e^{-t/\tau})dt = \Delta t - Mt_4,\\
Mt_2 &= \int_{t^n}^{t^{n+1}} (\tau(-1+e^{-t/\tau}) + te^{-t/\tau})dt = -\tau Mt_1 + Mt_5,\\
Mt_3 &= \int_{t^n}^{t^{n+1}} \tau(t/\tau - 1 + e^{-t/\tau})dt = \frac{1}{2}\Delta t^2 - \tau Mt_1.
\end{aligned}$$

*Calculate the flux of conservative variables related to $g_0$*

Theoretically, $\int_{t^n}^{t^{n+1}}\int \tilde{g}_{i+1/2}u\psi d\Xi dt$ can be calculated analytically. But the integration related to $g^+$ is too complex, and will be calculated with numerical integration. Only the terms related to $g_0$ will be integrated analytically here.

$$\mathbf{F}_{g_0} = Mt_1\rho_0 < u\psi > + Mt_2\rho_0\left(< a^L u^2\psi >_{>0} + < a^R u^2\psi >_{<0}\right) + Mt_3\rho_0 < Au\psi >$$

*Calculate the flux of conservative variables related to $g^+$ and $f_0$*

First evaluate $H_k, B_k$ corresponding to $g_0$ by Eq. A.14,

$$H_k = \rho_0\left(\frac{\lambda_0}{\pi}\right)^{1/2} e^{-\lambda_0(u_k-U_0)^2}, \quad B_k = \frac{K}{2\lambda_0}H_k,$$

and then evaluate $H_k^+, B_k^+$ corresponding to $g^+$ by Eq. A.15,

$$H_k^+ = \frac{4(1-\Pr)\lambda_0^2}{5\rho_0}(u_k - U_0)q(2\lambda_0(u_k-U_0)^2 + K - 5)H_k,$$
$$B_k^+ = \frac{4(1-\Pr)\lambda_0^2}{5\rho_0}(u_k - U_0)q(2\lambda_0(u_k-U_0)^2 + K - 3)B_k.$$

The flux of conservative variables related to $g^+$ is,

$$\mathbf{F}_{g^+} = Mt_1 \begin{pmatrix} \sum \alpha_k u_k H_k^+ \\ \sum \alpha_k u_k^2 H_k^+ \\ \frac{1}{2}\left(\sum \alpha_k u_k^3 H_k^+ + \sum \alpha_k u_k B_k^+\right) \end{pmatrix}.$$

The flux of conservative variables related to $f_0$ is,

$$\mathbf{F}_{f_0} = Mt_4 \begin{pmatrix} \sum \alpha_k u_k h_{i+1/2,k} \\ \sum \alpha_k u_k^2 h_{i+1/2,k} \\ \frac{1}{2}\left(\sum \alpha_k u_k^3 h_{i+1/2,k} + \sum \alpha_k u_k b_{i+1/2,k}\right) \end{pmatrix}$$
$$-Mt_5 \begin{pmatrix} \sum \alpha_k u_k^2 \sigma^h_{i+1/2,k} \\ \sum \alpha_k u_k^3 \sigma^h_{i+1/2,k} \\ \frac{1}{2}\left(\sum \alpha_k u_k^4 \sigma^h_{i+1/2,k} + \sum \alpha_k u_k^2 \sigma^b_{i+1/2,k}\right) \end{pmatrix}.$$

The flux of conservative variables is,

$$\mathbf{F}_{i+1/2} = \int_{t^n}^{t^{n+1}} \int f_{i+1/2} u \psi d\Xi dt = \mathbf{F}_{g_0} + \mathbf{F}_{g^+} + \mathbf{F}_{f_0}.$$

*Calculate the flux of distribution functions*

The flux of reduced distribution function $h$ is calculated by,

$$\begin{aligned}
\int_{t^n}^{t^{n+1}} \mathbf{f}^h_{i+1/2,k} dt &= \int_{t^n}^{t^{n+1}} \int f_{i+1/2,k} u_k d\xi dt \\
&= Mt_1 u_k (H_k + H_k^+) \\
&+ Mt_2 u_k^2 \left( a_1^L H_k + a_2^L u_k H_k + \frac{1}{2} a_3^L (u_k^2 H_k + B_k) \right) H[u_k] \\
&+ Mt_2 u_k^2 \left( a_1^R H_k + a_2^R u_k H_k + \frac{1}{2} a_3^R (u_k^2 H_k + B_k) \right) (1 - H[u_k]) \\
&+ Mt_3 u_k \left( A_1 H_k + A_2 u_k H_k + \frac{1}{2} A_3 (u_k^2 H_k + B_k) \right) \\
&+ Mt_4 u_k h_{i+1/2,k} - Mt_5 u_k^2 \sigma^h_{i+1/2,k}.
\end{aligned}$$

The flux of reduced distribution function $b$ is calculated by,

$$\begin{aligned}
\int_{t^n}^{t^{n+1}} \mathbf{f}^h_{i+1/2,k} dt &= \int_{t^n}^{t^{n+1}} \int f_{i+1/2,k} u_k d\xi dt \\
&= Mt_1 u_k (B_k + B_k^+) \\
&+ Mt_2 u_k^2 \left( a_1^L B_k + a_2^L u_k B_k + \frac{1}{2} a_3^L (u_k^2 B_k + < \xi^4 > H_k) \right) H[u_k] \\
&+ Mt_2 u_k^2 \left( a_1^R B_k + a_2^R u_k B_k + \frac{1}{2} a_3^R (u_k^2 B_k + < \xi^4 > H_k) \right) (1 - H[u_k]) \\
&+ Mt_3 u_k \left( A_1 B_k + A_2 u_k B_k + \frac{1}{2} A_3 (u_k^2 B_k + < \xi^4 > H_k) \right) \\
&+ Mt_4 u_k b_{i+1/2,k} - Mt_5 u_k^2 \sigma^b_{i+1/2,k}.
\end{aligned}$$

## A.6 Update Cell Averaged Value

The procedure is shown in Figure A.3.

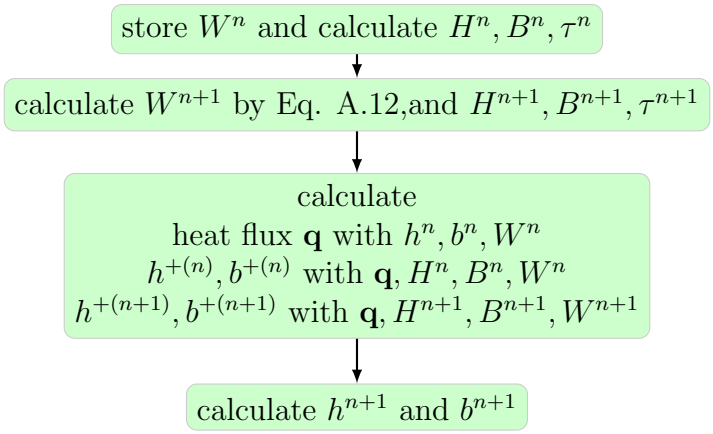


Figure A.3: Update cell averaged value

The equation for updating $h^{n+1}$ and $b^{n+1}$ can be obtained from Eq. A.11,

$$h_{i,k}^{n+1} = \left(1 + \frac{\Delta t}{2\tau^{n+1}}\right)^{-1} \left[h_{i,k}^n + \frac{1}{\Delta x}\int_{t^n}^{t^{n+1}} (\mathbf{f}_{i-1/2}^h - \mathbf{f}_{i+1/2}^h)dt + \frac{\Delta t}{2}\left(\frac{h_{i,k}^{+(n+1)}}{\tau^{n+1}} + \frac{h_{i,k}^{+(n)} - h_{i,k}^n}{\tau^n}\right)\right],$$

$$b_{i,k}^{n+1} = \left(1 + \frac{\Delta t}{2\tau^{n+1}}\right)^{-1} \left[b_{i,k}^n + \frac{1}{\Delta x}\int_{t^n}^{t^{n+1}} (\mathbf{f}_{i-1/2}^b - \mathbf{f}_{i+1/2}^b)dt + \frac{\Delta t}{2}\left(\frac{b_{i,k}^{+(n+1)}}{\tau^{n+1}} + \frac{b_{i,k}^{+(n)} - b_{i,k}^n}{\tau^n}\right)\right].$$

## A.7 Boundary Condition

Only isothermal wall boundary condition with complete accommodation is discussed. The boundary condition described here is quite simple. The incoming distribution function is directly obtained through interpolation.

Firstly, obtain $h_k^{in}, b_k^{in}$ by one-sided interpolation from the interior region. For example,

$$h_k^{in} = h_{1,k} - \sigma_{1,k}^h \frac{\Delta x}{2}.$$

Secondly, calculate the density at the wall with the condition that no particle penetrates the wall,

$$\int_{t^n}^{t^{n+1}} \int_{u>0} u g_w d\Xi dt + \int_{t^n}^{t^{n+1}} \int_{u<0} u f^{in} d\Xi dt = 0,$$

which gives,

$$\rho_w = -\frac{\sum \alpha_k u_k h_k^{in}}{\left(\frac{\lambda_w}{\pi}\right)^{1/2} \sum \alpha_k u_k e^{-\lambda_w (u_k - U_w)^2}},$$

where $g_w, \rho_w, \lambda_w, U_w$ are the variables at the wall.

The corresponding reduced Maxwellian distribution at the wall $H_k^w, B_k^w$ is also obtained.

Thirdly, the distribution function at the boundary interface is expressed by (same holds for $b_k$),

$$h_k = H_k^w H[u_k] + h_k^{in}(1 - H[u_k]).$$

Finally, the flux across the wall is calculated by,

$$\mathbf{F}_{1/2} = \Delta t \begin{pmatrix} \sum \alpha_k u_k h_k \\ \sum \alpha_k u_k^2 h_k \\ \sum \alpha_k \frac{1}{2} \left(u_k^3 h_k + u_k b_k\right) \end{pmatrix},$$

and,

$$\int_{t^n}^{t^{n+1}} \mathbf{f}_{1/2,k}^h dt = \Delta t u_k h_k,$$
$$\int_{t^n}^{t^{n+1}} \mathbf{F}_{1/2,k}^b dt = \Delta t u_k b_k.$$

## A.8 UGKS2D Code

### *A.8.1 Differences with 1D*

For 2D problem, many expressions need to be slightly changed. For example,

$$g = \rho \left(\frac{\lambda}{\pi}\right)^{\frac{K+2}{2}} e^{-\lambda((u-U)^2+(v-V)^2+\xi^2)},$$

where $v$ is particle velocity in y direction, $V$ is macroscopic velocity in y direction.

The relation between $K$ and $\gamma$ becomes,

$$\gamma = \frac{K+4}{K+2}.$$

The reduced Maxwellian distribution becomes ($B$ is not changed),

$$H = \int_{-\infty}^{\infty} g d\xi = \rho \left(\frac{\lambda}{\pi}\right) e^{-\lambda((u-U)^2+(v-V)^2)}.$$

The collision invariants are $\psi = (1, u, v, 1/2(u^2 + v^2 + \xi^2))^T$. And the expressions for macroscopic variables are correspondingly changed. For example, the non-dimensionalized pressure is calculated via,

$$\frac{K+2}{2} p = \int ((u-U)^2 + (v-V)^2) h du + \int b du.$$

When calculating the flux, the slopes related to Maxwellian become,

$$a = a_1 + a_2 u + a_3 v + a_4 \frac{1}{2}(u^2 + v^2 + \xi^2),$$

and the components are calculated via,

$$
\begin{aligned}
a_4 &= \frac{4\lambda_0^2}{(K+2)\rho_0}\left[2\frac{\partial \rho E}{\partial x} + \left(U_0^2 + V_0^2 - \frac{K+2}{2\lambda_0}\right)\frac{\partial \rho}{\partial x} - 2U_0\frac{\partial \rho U}{\partial x} - 2V_0\frac{\partial \rho V}{\partial x}\right], \\
a_3 &= \frac{2\lambda_0}{\rho_0}\left(\frac{\partial \rho V}{\partial x} - V_0\frac{\partial \rho}{\partial x}\right) - V_0 a_4, \\
a_2 &= \frac{2\lambda_0}{\rho_0}\left(\frac{\partial \rho U}{\partial x} - U_0\frac{\partial \rho}{\partial x}\right) - U_0 a_4, \\
a_1 &= \frac{1}{\rho_0}\frac{\partial \rho}{\partial x} - U_0 a_2 - V_0 a_3 - \frac{1}{2}\left(U_0^2 + V_0^2 + \frac{k+2}{2\lambda_0}\right)a_4.
\end{aligned}
$$

### *A.8.2 Other Information*

The Gaussian quadrature used in the code is from Table IIa of Shizgal [38], which is better than Gaussian-Hermite quadrature in high Knudsen number case. But for the cavity problem with Kn $> 1$, Newton-Cotes formula of $100 \times 100$ velocity grids can avoid oscillating in the solution even with a Van-Leer limiter, which happens using Gaussian quadrature and second order interpolation.

## A.9 Moments of Maxwellian Distribution Function

In the program, the moments of Maxwellian distribution function is frequently used.

The moments of Maxwellian distribution function is defined as,

$$
\rho < ... >= \int (...) g d\Xi,
$$

and have the property that,

$$
< u^n \xi^m >=< u^n >< \xi^m >,
$$

where $m, n$ are integers.

*Moments of* $\xi^m$

$$< \xi^2 >= \left(\frac{K}{2\lambda}\right), \quad < \xi^4 >= \left(\frac{3K}{4\lambda^2} + \frac{K(K-1)}{4\lambda^2}\right).$$

*Moments of* $u^n$

The integration limits of $< u^n >$ are from $-\infty$ to $\infty$,

$$\begin{aligned} < u^0 > &= 1, \\ < u^1 > &= U, \\ < u^{n+2} > &= U < u^{n+1} > + \frac{n+1}{2\lambda} < u^n > . \end{aligned}$$

The integration limits of $< u^n >_{>0}$ are from 0 to $\infty$,

$$\begin{aligned} < u^0 >_{>0} &= \frac{1}{2}\mathrm{erfc}(-\sqrt{\lambda}U), \\ < u^1 >_{>0} &= U < u^0 >_{>0} + \frac{1}{2}\frac{e^{-\lambda U^2}}{\sqrt{\pi\lambda}}, \\ < u^{n+2} >_{>0} &= U < u^{n+1} >_{>0} + \frac{n+1}{2\lambda} < u^n >_{>0} . \end{aligned}$$

The integration limits of $< u^n >_{<0}$ are from $-\infty$ to 0,

$$\begin{aligned} < u^0 >_{<0} &= \frac{1}{2}\mathrm{erfc}(\sqrt{\lambda}U), \\ < u^1 >_{<0} &= U < u^0 >_{<0} - \frac{1}{2}\frac{e^{-\lambda U^2}}{\sqrt{\pi\lambda}}, \\ < u^{n+2} >_{<0} &= U < u^{n+1} >_{<0} + \frac{n+1}{2\lambda} < u^n >_{<0} . \end{aligned}$$

*Moments of* $< u^n \xi^m \psi >$

There are three components for 1D problem,

$$< u^n \xi^m \psi >= \begin{pmatrix} < u^n >< \xi^m > \\ < u^{n+1} >< \xi^m > \\ \frac{1}{2}\left(< u^{n+2} >< \xi^m > + < u^n >< \xi^{m+2} >\right) \end{pmatrix}.$$

*Moments of* $< a u^n \psi >$

There are three components for 1D problem,

$$< a u^n \psi >= a_1 < u^n \psi > + a_2 < u^{n+1} \psi > + \frac{1}{2} a_3 \left(< u^{n+2} \psi > + < u^n \xi^2 \psi >\right).$$